METAL-ASSISTED CHEMICALLY ETCHED SILICON NANOWIRE SYSTEMS FOR BIOCHEMICAL AND ENERGY STORAGE APPLICATIONS

ZHENG HAN

(B. Eng. (Hons.), NUS)

A THESIS SUBMITTED

FOR THE DEGREE OF DOCTOR OF PHILOSOPHY

DEPARTMENT OF ELECTRICAL AND COMPUTER ENGINEERING

NATIONAL UNIVERSITY OF SINGAPORE

2014

DECLARATION

I hereby declare that this thesis is my original work
and it has been written by me in its entirety.
I have duly acknowledged all the sources of information
which have been used in the thesis.

This thesis has also not been submitted for any degree
in any university previously.

Zheng Han

11 August 2014

Acknowledgements

This thesis presents the interdisciplinary studies I have spent effort on over the past four years. Coming to the end of my Ph.D study, I would like to sincerely thank all those people who made this work possible.

First and foremost I would like to express my deepest gratitude to my thesis supervisor, Professor Choi Wee Kiong, for his invaluable guidance, support and encouragement even during his medical treatments in the past two years. Professor Choi is a knowledgeable, patient and responsible teacher, at the mean time; he is also an imaginative, adventurous and persistent researcher. His enthusiasm in research and excellent management skills made him a great team leader. All the cross-disciplinary research projects would not be possible without his support. It has been an honor for me to be his student. I appreciate all his time and effort to make me a productive and responsible researcher. His motivation and encouragement have helped me in all the time of my research and thesis writing.

I am greatly in dept to Professor Raj Rajagopalan and Professor Too Heng-Phon for the knowledge and advice on the protein microarray project. I would like to thank Professor Saif A. Khan for his insights in the biomimicking applications of the silicon nanowires. My sincere thanks also go to Professor Carl V. Thompson for the critical and informative discussions with him on the topics of Si and Ge metal-assisted etching.

Microelectronics Laboratory is a big family, where everyone is always willing to help each other. I am so thankful to Mr Walter Lim and Mdm Ah Liang Kiat for their continuous effort on maintaining the equipment and managing the lab resources. I would like to thank my seniors Liew Tze Haw and Khalid for their guidance and support during my final year project and the beginning stage of the Ph.D study. Special thanks to my teammates Cheng He, Wu Jia Xin, Lai Changquan, Mai Trong Thi, Raja and Lin Thu for all the help when we worked together. I also want to acknowledge the rest of my friendly colleagues, Wang Zongbin, Zhu Mei, Li Bihan, Xu Wei, Yudi, Ria and Wang Kai who have helped me one way or the other. I am especially grateful to Yu Sihang for his immense contribution to our etching projects in the past two years.

Next, I want to thank GLOBALFOUNDRIES Singapore Pte Ltd and Economic Development Board (EDB) for providing the research scholarship. I very much appreciate the comprehensive training given by Dr. Lap Chan, Mr. Leong Kam Chew and Dr. Ng Chee Mang. Especially, I want to thank Dr. Lap Chan and Mr. Leong Kam Chew for all the help and support during my candidature. My thanks also go to the colleagues in GF SP program. It has been a pleasure to work with you all.

Last but not least, I want to thank my supportive wife and parents for all the love and encouragement. I owe everything to them and I will cherish every moment with them in my life.

Table of Contents

Summary

Silicon (Si) nanowires are important building blocks for wide range of applications, such as nanoelectronics, optoelectronics, energy storage systems and biochemical applications. In this study, ordered and random Si nanowires were fabricated using interference lithography and metal-assisted chemical etching (IL-MACE) and glancing angle deposition and metal-assisted chemical etching (GLAD-MACE), respectively. The surface morphology and porosity of these metal-assisted chemically etched nanowires were investigated with various characterization techniques, including scanning electron microscopy (SEM), transmission electron microscopy (TEM), Brunauer-Emett-Teller (BET) and thermoporometry. It was found that the GLAD-MACE nanowires were relatively thinner and more porous than IL-MACE nanowires.

Metal-assisted chemically etched silicon nanowire substrates were used for DNA and protein microarrays with an analyte-specific homogeneous mixing strategy. The surface loading capacities of the substrates were examined by direct coupling of dye molecules on the functionalized Si nanowires. Detailed investigation showed that surface porosity and the clumping of nanowires were the primary and secondary factors for determining the loading capacities of the nanowires, respectively. GLAD-MACE (Au) samples showed the highest loading capacity and therefore were further functionalized by carboxyl groups for stationary incubation of sense DNA. The subsequent DNA and protein detections were performed by hybridization of dye-modified anti-sense ssDNA and analyte-antibody-anti-sense-DNA complex conjugated in homogeneous phase solution.

The DNA and protein microarrays showed capturing efficiencies of up to 250 fold increase as compared to those on flat Si samples. After signal amplification, sepsis biomarker, IL-8 protein, was captured on the Si nanowire platform, which showed a lower detection limit of ~1nM.

The surface morphology of GLAD-MACE silicon nanowires was tuned by different GLAD durations and surface drying methods to mimick the famous lotus and petal effects. Different GLAD durations resulted in different morphologies of Au nanoparticles, which determined the porosity and morphologies of GLAD-MACE Si nanowires. Lotus-like and petal-like surfaces were obtained on the silanized GLAD-MACE samples using longer and shorter GLAD durations, respectively. Different liquid drying medium also changed the surface morphology and wettability of Si nanowires. The DI water dried and 2-propanol dried samples coated with organosilane showed lotus-like and petal-like wetting behaviors, respectively. Both of these two methods were successfully used to demonstrate the integration of lotus-like and petal-like surfaces on a single substrate.

Amorphous Si nanowires were fabricated by IL-MACE and GLAD-MACE methods to systematically study their performance as anode material for lithium-ion micro-battery application. As the battery performance of monolithic Si thin film anode suffered from pulverization, cracking and large volume change when the film thickness increased, GLAD-MACE and IL-MACE Si nanowires were integrated into the anode to reduce these issues. However, GLAD-MACE samples had severe degradation of cycling performance within 50 cycles due to

large volume change of the nanowires. To improve the performance, IL-MACE Si nanowires with larger diameter and inter-wire space were used to replace GLAD-MACE nanowires. IL-MACE nanowires remained intact after 50 cycles, which led to good cycling performance and areal specific capacity performance. The rate performance results showed that Si nanowires were superior to Si thin films for battery anode due to reduced lithium-ion diffusion length on Si nanowires.

List of Tables

List of Figures

List of Symbols and Acronyms

Si	Silicon
IL	Interference lithography
GLAD	Glancing angle deposition
MACE	Metal-assisted chemical etching
SEM	Scanning electron microscopy
TEM	Transmission electron microscopy
BET	Brunauer-Emett-Teller
DNA	Deoxyribonucleic acid
Au	Gold
Ag	Silver
ssDNA	Single strand deoxyribonucleic acid
ASR	Analyte specific reagent
IL-8	Interleukin-8
DI water	De-ionized water
VLS	Vapor-liquid-solid
SiH_4	silane
$SiCl_4$	Silicon tetrachloride
CVD	Chemical vapor deposition
MBE	Molecular beam epitaxy
KOH	Potassium hydroxide
TMAH	Tetramethylammonium hydroxide
H_2O_2	Hydrogen peroxide
HF	Hydrofluoric acid
Pt	Platinum

Pd	Palladium
Cu	Copper
h^+	Hole
$AgNO_3$	Silver nitride
P	Etchant composition of [HF] / ([H_2O_2] +[HF])
FET	Field effect transistor
APTES	(3-Aminopropyl)triethoxysilane
BSA	Bovine serum albumin
IgG	Immunoglobulin G
IgM	Immunoglobulin M
Cy3	Cyanine-3
Cy5	Cyanine-5
FITC	Fluorescein isothiocyanate
SC	Standard cleaning
RCA	Radio Corporation of America
NH_4OH	Ammonium hydroxide
N_2	Nitrogen
HCl	Hydrochloric acid
Ar	Argon
He	Helium
Cd	Cadmium
UV	Ultraviolet
p	Period of structures
λ	Wavelength of the light source
θ	Half angle between two interfering beams

Ta	Tantalum
Mo	Molybdenum
W	Tungsten
Al	Aluminum
H_2O	Water
O_2	Oxygen
CCD	Charge coupled device
HRTEM	High resolution transmission electron microscopy
P/P_0	Relative pressure of inert gas
V	Amount of gas adsorbed
V_m	Amount of gas adsorbed for a monolayer
C	BET constant
BJH	Barrett−Joyner−Halenda
γ_{ls}	Liquid-solid interfacial tension,
ΔH_0	Molar heat of fusion
v_l	Liquid phase molar volume
R_p	Pore radius
ΔT	Phase transition shift of temperature
DSC	Differential scanning calorimetry
ΔH_f	Enthalpy of fusion
3-D	Three dimensional
NHS	1-hydroxy-2-nitrobenzene-4-sulfonic acid
SDC	Synthetic complete
RFU	Relative fluorescent unit
EDC	1-Ethyl-3-(3-dimethylaminopropyl)carbodiimide

MES	2-(N-morpholino)ethanesulfonic acid
HNSA	1-hydroxy-2-nitrobenzene-4-sulfonic acid
PBS	Phosphate buffered saline
f	Solid fraction
θ_0	Young's angle
θ^*	Surface contact angle
F_V	van der Waals force
BOE	Buffered oxide etch
PCT	Procalcitonin
CRP	C-reactive protein
Ω	Ohm
V	Volt
sccm	Standard cubic centimeters per minute
W	Watt
wt%	Weight percentage
rpm	Round per minute
°C	Degree Celsius
M	Molar
keV	Kilo-electron volts
K	Kelvin

Chapter 1 Introduction

1.1 Background

Nanotechnology is the engineering of functional structures in atomic or molecular scale.[1] In the past decades, fast progress has been made on the research and development of artificial construction and application of the surfaces with functional nanostructures.[2],[3] The most widely used material for the fabrication of nanostructures is silicon (Si), because of its advantages in abundant supply in natural form and the interesting electrical properties for integrated circuits.[2],[3] As the size of electronic transistors continued to shrink, numerous processing techniques have been developed for the fabrication of smaller Si nanostructures.[4]-[28] In addition to the low cost and availability of fabrication techniques, Si has many other superior properties, such as good biocompatibility and high gravimetric capacity.[2],[29]-[31] Among different nanostructures, Si nanowires with high surface-to-volume ratio are of particular interest for the potential applications in nanoelectronic, optoelectronic, biochemical and energy storage systems.[2],[3],[29]-[31]

Recently, the novel metal-assisted chemical etching of Si has been extensively studied for its simple experimental setup, anisotropic etching direction, capability of creating high aspect ratio nanostructures and good control of etching profile and Si crystal quality.[3] With interconnected patterns of noble metals (e.g. Au) on the Si surface, Si nanowires with small diameter, large height and high porosity can be obtained using this method. In this study, metal-assisted chemical etching of Si will be combined with different patterning methods to create Si

nanowires of different morphology and porosity in large area. The enhanced surface area and tunable surface morphology of metal-assisted chemically etched Si nanowires will be investigated for the applications in bioanalytic, biomimetic and energy storage applications.

1.2 Research Objective

This study aims to develop new methods to fabricate metal-assisted chemically etched Si nanowires with high aspect ratio and porosity. The high aspect ratio and porosity of the nanowires coupled with the gravimetric capacity to develop biomedical and energy storage applications. The Si nanowires will be characterized in terms of porosity, dimensions and surface morphology to understand the performance of different metal-assisted chemically etched nanowire systems in different applications.

1.3 Organization of Thesis

This thesis is organized into eight chapters.

Chapter 1 is the introduction consisting of background information and research objective of this thesis.

Chapter 2 provides a brief literature review of the publications related to this work. Various Si nanowire fabrication methods will be briefly discussed including bottom-up and top-down methods. Next, metal-assisted chemical etching of Si will be reviewed, which will be followed by the bioanalytic, biomimetic and energy storage applications of Si nanowires.

Chapter 3 is the experimental detail of the Si nanowire fabrication procedures and characterization techniques.

Chapter 4 describes the IL-MACE and GLAD-MACE Si nanowire fabrication methods. The process flow of these two methods will be introduced. Regular and random Si nanowires fabricated on both single crystalline Si wafer and sputtered amorphous Si on stainless steel substrates will be discussed. The surface morphology and porosity results obtained by different characterization techniques will be analyzed.

Chapter 5 presents the bioanalytic applications of metal-assisted chemically etched Si nanowires. The DNA and protein capturing strategy on Si nanowire substrates will be introduced. The experimental procedures and process flows for the substrate fabrication and biomedical detections will be discussed. In order to select the best substrate for DNA and protein detections, the surface loading capacities of various metal-assisted chemically etched Si nanowire samples will be compared by direct coupling of dye molecules. The surface loading capacity will be investigated with respect to different morphologies and porosity of the samples. The performance of the bio-detection platform will be examined by capturing DNA and protein on the nanowire substrate. This chapter will end with the detection of sepsis protein biomarker.

Chapter 6 demonstrates the biomimetic application of lotus and petal effect using GLAD-MACE Si nanowire substrates. The GLAD duration and surface drying method will be used to modulate the surface adhesion of the

superhydrophobic nanowire surfaces. These methods will be used to integrate lotus-like and petal-like surfaces on a single substrate.

Chapter 7 provides the lithium ion battery results of Si anodes based on metal-assisted chemically etched Si nanowires. The performance of monolithic Si thin film samples will be first discussed to understand the issues with Si anode, which will be followed by the investigation of the battery performance of GLAD-MACE and IL-MACE Si nanowire based anodes. The rate performance and areal specific capacity of different types of samples will also be compared.

Chapter 8 gives a brief conclusion of this thesis. The recommendations for future work will also be provided in this chapter.

Chapter 2 Literature Review

2.1 Introduction

This chapter provides a brief review of the scientific reports related to the topic of metal-assisted chemically etched Si nanowires and practical applications based on Si nanowires. First of all, the bottom-up and top-down methods for Si nanowire fabrication will be discussed, including vapor-liquid-solid mechanism, chemical vapor deposition, molecular beam epitaxy, laser ablation and reactive ion etching. Next, the novel method of metal-assisted chemical etching for Si nanowire fabrication will be introduced. The background information, etching mechanism of metal-assisted chemical etching will be reviewed, which will be followed by the discussions of etching rate, etching direction and porosity. This chapter will end with the review of bioanalytic, biomimetic and energy storage applications using Si nanowires.

2.2 Fabrication of Silicon Nanowires

The synthesis of Si nanowires can be generally categorized into two approaches, which are bottom-up and top-down methods. The various methods have distinct characteristics and can produce Si nanowires with different structural and chemical properties.[4]-[28] In the following sections, these methods will be briefly introduced together with their advantages and limitations.

2.2.1 Bottom-up Methods

The basic working principle for bottom-up approach to produce Si nanowires is based on nucleation and crystal growth of molecular Si precursors (e.g. SiH_4, $SiCl_4$) through thermodynamic and kinetic reactions.[4] The bottom-up approach to grow Si nanowires was pioneered by Wagner and Ellis, who developed the famous mechanism of vapor-liquid-solid (VLS) in 1960s.[5] The VLS mechanism was demonstrated by introducing gaseous Si precursors to a catalytic liquid alloy at eutectic temperature (e.g. Au-Si alloy at over 363ºC). As the name VLS indicates, during this reaction, liquid alloy droplet rapidly adsorbed and decomposed vapor phase precursor and caused Si crystal growth at the liquid-solid interface (See Figure 2.1).[5] In the past decades, VLS mechanism was the most common way to grow single crystalline Si nanowires and it established the foundation for numerous bottom-up fabrication techniques, including chemical vapor deposition (CVD), molecular beam epitaxy (MBE) and laser ablation.[5]-[19]

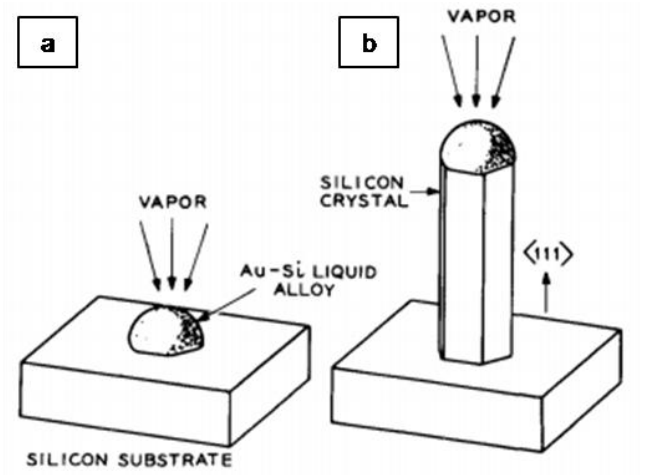

Figure 2.1: Schematic diagram of growth of single crystal Si by VLS mechanism. (a) is the initial growth condition, (b) is the Si wire formed with the catalyst at the tip. [5]

CVD was originally designed for thin film deposition. With catalytic nanoparticles such as gold, nickel and iron, this technique can be utilized to grow epitaxially aligned single crystalline Si nanowires using VLS mechanism.[6]-[9] As shown in Figure 2.2, the Si samples with deposited metal particles were annealed at elevated temperature (above eutectic temperature) to form liquid catalyst, which was supersaturated with Si after exposure to gas phase Si precursors.[10] As the alloys of the above mentioned metal catalysts and Si have low eutectic temperatures, the CVD process has relatively low thermal budget and may be compatible for applications with requirement of low processing temperature. Since the epitaxial growth of Si nanowires is dependent on the catalyst particles, the diameter and location of the nanowires can be determined by the initial morphology of the catalyst particles.[5],[11],[12] In addition, the growth rate can be modulated by different types of metal catalysts and processing

temperatures. The length of Si nanowires can be simply controlled by growth duration.[13]

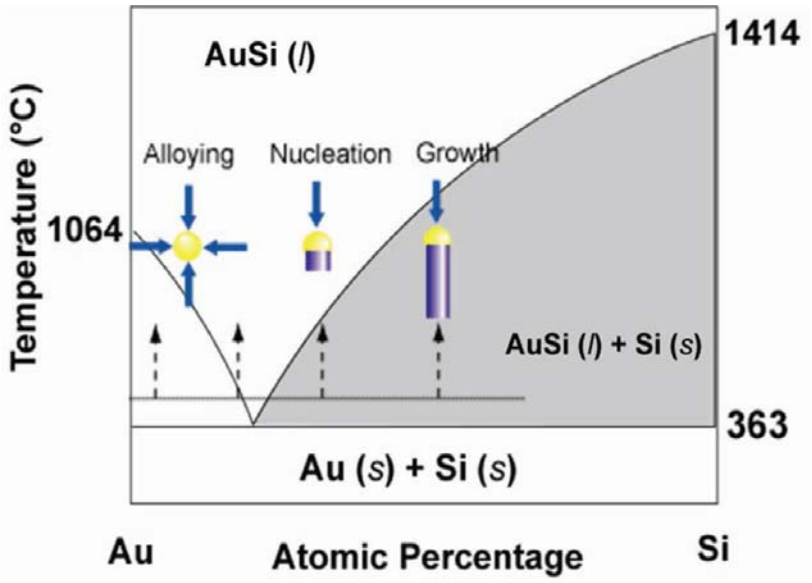

Figure 2.2: Phase diagram illustrating the different stages (alloying, nucleation, growth) involved in the VLS growth of Si nanowires catalyzed by Au nanoparticles above eutectic temperature of Au-Si. [10]

Similar to the CVD technique, MBE was initially used to grow thin film material when it was invented in 1970s.[14] MBE is an ultrahigh vacuum technique to deposit material with high purity and crystallinity. In a MBE system, a solid high-purity Si source is heated till evaporation and the gaseous Si atoms are directed towards the substrates for epitaxial deposition. In order to grow Si nanowires, metal particles are also used as catalysts in MBE.[16] As no precursor gas is used in MBE for decomposition, the Si nanowire growth is governed by flux of Si atoms. Precise control of thin film composition and doping can be

achieved by this technique at ultrahigh vacuum environment.[16],[17] However, the MBE method is not commonly used due to high cost as compared to CVD.

Laser ablation in combination with VLS growth is another technique to create ultra-slim single crystal Si nanowires. This method was introduced by Morales and Lieber in 1998.[18] Laser ablation was used to produce nanoscale catalyst clusters for VLS growth of Si nanowires. The photonic energy supplied by laser ablation converted the target material with elemental compositions of Si and metal catalysts into vapor phase. The vapor at high temperature was mixed with cold inert gas to condense into liquid clusters of Si and metal species. After the liquid alloy was supersaturated, Si nanowires were formed and the growth continued as long as the catalyst alloy remained in liquid form by high temperature. This method has good flexibility to control the nanowire composition by using different target material and the growth of high aspect ratio nanowires does not require the use of a solid substrate.[9],[19]

In general, there are certain limitations with the bottom-up methods.[20] Without the assistance of a top-down technique (e.g. photolithography), it is difficult to obtain regular Si nanowires. In addition, the metal catalyst used in the synthesis of VLS Si nanowires may cause contamination during the Si nanowire formation process due to remaining catalyst at the bottom or in the middle of the nanowires. More importantly, the bottom-up methods are generally inferior to top-down methods in terms of size variability as the size of metal catalysts cannot be well controlled during de-wetting.

2.2.2 Top-down Methods

The top-down methods for Si nanowire fabrication typically come with a combination of lithographic and etching processes. With the development of modern microelectronic technology, a variety of lithographic techniques have been developed including photolithography and electron beam lithography.[21] Other patterning methods such as polymer based nanosphere lithography and anodic aluminum oxide template based process have also been used to create close-packed nanostructures in large scale.[22] Even though these two methods do not require lithographic photomask, it has been proven difficult to create defect-free perfectly periodic patterns over long range using these mask-less techniques. Recently, interference lithography with a Lloyd's mirror configuration was developed. This technique was capable of creating ordered pattern with good control of the period, diameter and cross-sectional shape in the nanometer range.[20]

Etching is an important process to transfer the pattern defined by photoresist or other templates into Si structures. The most commonly used etching method to fabricate Si nanowires is dry etching, such as reactive ion etching. This is because wet etching of Si is mostly isotropic. One exception for Si wet etching is the anisotropic etching of Si by certain alkaline solution (e.g. KOH, TMAH) due to the slowest etching orientation along Si(111).[23] For the alkaline etching of Si (100), an inverted pyramid shape was formed with slanted sidewall along Si (111) plane. This process has very limited use due to etching direction induced limited aspect ratio of the etching profile. On the other hand, dry etching is

capable of fabricating anisotropic Si nanostructures with high aspect ratio.[24],[25] The directional etching is realized by accelerating the ionized gas phase etchant towards the sample surface. The etching profile can be tuned by simply adjusting the physical and chemical components of the dry etching process. To date, many dry etching methods have been developed, including reactive ion etching, inductively coupled plasma etching, magnetically enhanced ion etching and electron cyclotron resonance etching.[26],[27] It should be noted that the resolution of the dry etching of Si is mostly determined by the patterning process prior to the etching step. Despite the advantages in reliability and repeatability, dry etching has its limitation of surface damage of the nanostructures caused by ion bombardment.[28] In view of this, an anisotropic wet etching method, so called metal-assisted chemical etching, was developed recently with the assistance of catalytic noble metals.[2] This method is able to fabricate Si nanostructures with high aspect ratio, good crystal quality and directionality. Detail of the metal-assisted chemical etching will be reviewed in the following sections.

2.3 Metal-Assisted Chemical Etching of Silicon

2.3.1 Background

Metal-assisted chemical etching (MACE) of Si has attracted extensive research interest in the last decade.[2] The catalytic etching behavior of noble metal coated Si in a MACE etching solution was first demonstrated by Li and Bohn in 2000.[32] The typical MACE etching solution for Si consists of a removing agent of HF and an oxidizing agent of H_2O_2. The reported noble metal

catalysts for MACE of Si include Au, Pt, Ag, Pd and Cu.[2],[3] As Si underneath the metal catalyst is etched much faster than the rest of the region, Si nanostructures can be synthesized according to the initial morphology of the metal catalysts. For example, Si nanowires can be fabricated with a perforated noble metal film as shown in Figure 2.3.[32]

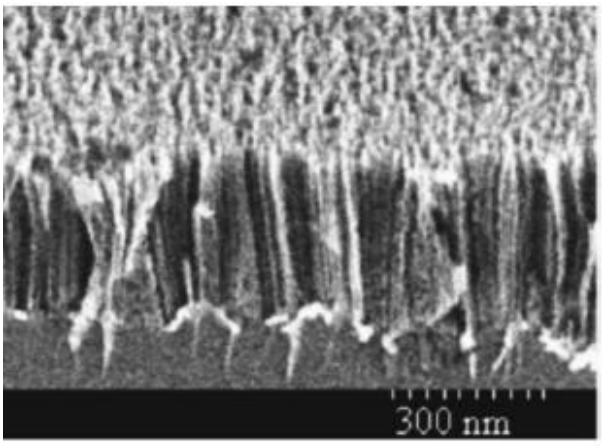

Figure 2.3: SEM image of the Si nanowires fabricated on Au patterned Si (100) substrate in a MACE solution of HF and H_2O_2. [32]

MACE has several advantages over other methods.[2],[3] First of all, this method is simple, low-cost and scalable with good repeatability. Secondly, MACE is an anisotropic etching method with easy and good control of the etching orientation, doping, diameter, shape and height of the resulting nanostructures. Thirdly, the crystalline quality of the MACE Si nanowires is better than that of VLS Si nanowires. Lastly but not least, this method has good variability of the nanowire orientation and cross-sectional shapes as compared to other methods.

2.3.2 Etching Mechanism

The etching mechanism of MACE has been proposed in many reports.[32]-[34] It is commonly accepted that noble metals serve as local cathode to accelerate the reduction of the oxidizing agent (e.g. H_2O_2). The reduction reaction generates large amount of holes (h^+), which are injected into the valance band of the Si via the metal catalysts for oxidation reaction as illustrated in Figure 2.4.[3] As the hole concentrates at the metal/Si interface, Si underneath the noble metal is preferentially oxidized and the resulting byproduct is removed by HF. The excess holes will diffuse to the surrounding region to cause surface and sidewall roughening. The equations for the redox reactions were proposed by Li and Bohn as [32]

Cathode:

$$H_2O_2 + 2H^+ \rightarrow 2H_2O + 2h^+ \quad (2.1)$$

$$2H^+ \rightarrow H_2\uparrow + 2h^+ \quad (2.2)$$

Anode:

$$Si + 4h^+ + 4HF \rightarrow SiF_4 + 4H^+ \quad (2.3)$$

$$SiF_4 + 2HF \rightarrow H_2SiF_6 \quad (2.4)$$

Due to lack of in-situ etching characterization methods, the actual mechanism of MACE still remains as an open question. Other proposed etching equations can be found in the literature.[33],[34]

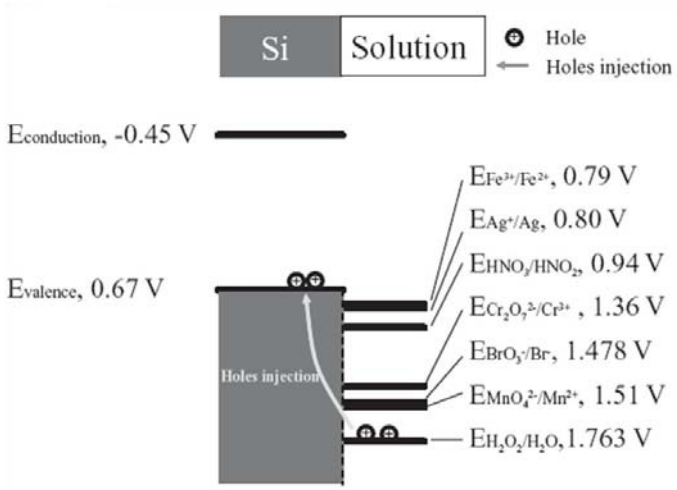

Figure 2.4: Energy band diagram schematics with potentials of Si and standard oxidants.[3]

2.3.3 Etch rate

It has been reported that the etching depth in MACE system is typically proportional to the etching duration. As shown in Figure 2.5, Cheng et al. summarized the etching results at different temperatures and concluded that the linear relationship and constant etching rate were valid at fixed etching condition.[35] Rykaczewski et al. also carried out a study to systematically investigate the effect of noble metal geometry on the MACE etching rate of Si.[36] The results indicated that isolated metal patterns with same area and different shapes had similar etch rate. In contrast, the etch rate generally increased with smaller size of the catalysts. It should be noted that isolated and interconnected metal patterns with same area did not lead to similar etching rate.

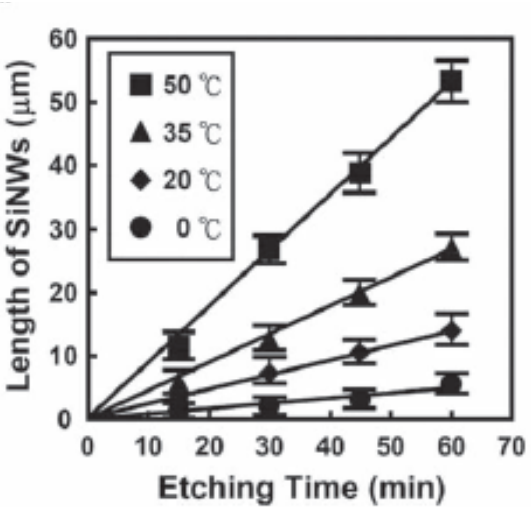

Figure 2.5: Plots of the etching depth over etching time at varied experimental temperature, indicating a linear relationship. [36]

2.3.4 Etch Direction

The etching direction of MACE of Si can be generally explained by the back-bond breaking theory, which has been used for many etching phenomenon, including the anisotropic etching behavior of Si etched in alkaline solution and anodic etching of Si.[37],[38] As wet etching is actually a bond breaking process, the strength of the back-bond along different crystal orientations largely affects the corresponding etch rate. For Si, there are two back-bonds for each atom on the (100) plane and three back-bonds for those on the (110) or (111) surface.[39] As a result, MACE of Si is intrinsically anisotropic along the <100> orientation. However, several studies have shown that the etching direction can be modulated by varied etchant concentration in the etching solution.[40],[41] Chern et al. reported that nanowires with crystallographic orientation of <100> and <111> were obtained on p-type Si(100) samples by different concentrations of HF and

H_2O_2.[40] One of the possible explanations for the concentration dependent etching direction is the weakened back-bond strength due to increased oxidant concentration.[42]

2.3.5 Porosity

The results of porous surface formation of MACE etched Si have been reported since the very early demonstration by Li and Bohn.[32] The results shown in Figure 2.6 indicate that less and smaller pores were formed for the off-metal area of Au coated p^- sample as compared to Au coated p^+ sample. In contrast, densely located larger pores were created for the Pt coated p^- sample. Apparently, both doping concentration of the Si wafer and the catalyst type have influence on the porous Si formation process.

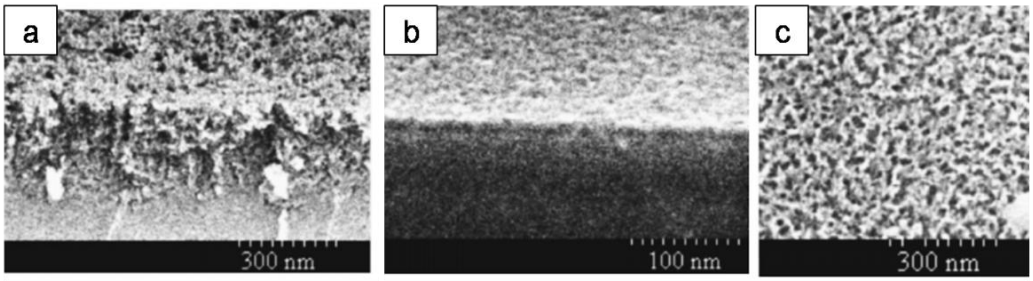

Figure 2.6: SEM results of the porous surface formed in the off-metal area of (a) Au coated p^+ , (b) Au coated p^- and (c) Pt coated p^- Si samples with fixed etching duration and etchant concentrations. [32]

Making use of the relationship between porosity and Si doping, Si nanowires with very high porosity were fabricated by immersing a heavily doped (resistivity < 0.005 Ω-cm) p-type Si wafer in an etching solution of $AgNO_3$ and HF.[43] The structural characterization results are summarized in Figure 2.7. The

mesoporous Si nanowires fabricated in this experiment have high aspect ratio and remain single crystalline after etching. The high total surface area and pore volume were characterized by Brunauer-Emett-Teller (BET) gas sorption technique.

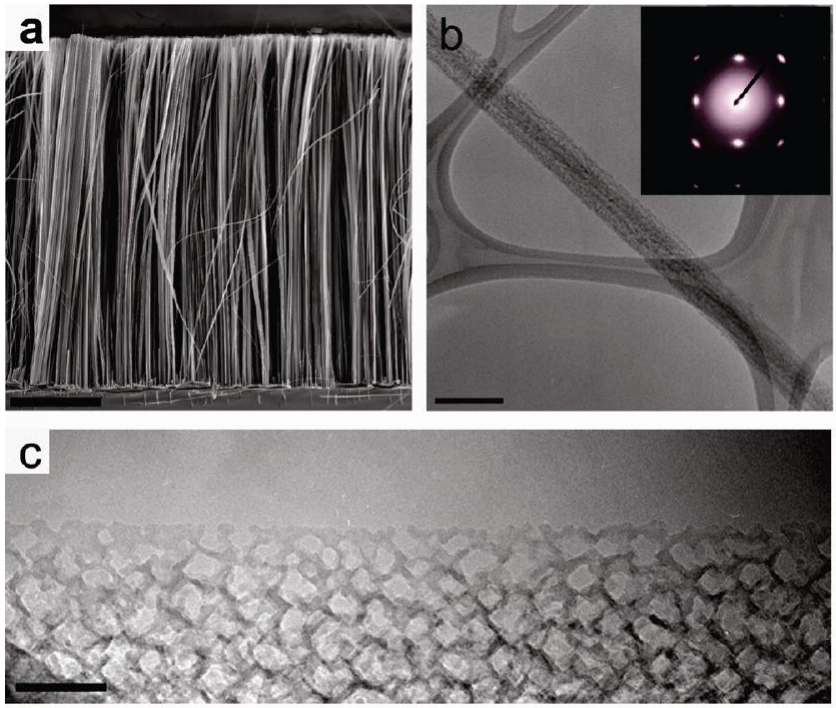

Figure 2.7: Structural characterization results of the highly doped Si nanowires after MACE in a solution of $AgNO_3$ and HF. (a) is the cross-sectional SEM of the nanowires. (b) TEM of a porous Si nanowire with Selected Area Electron Diffraction (SAED) in the inset indicating the crystallinity of the nanowire. (c) HRTEM clearly shows the mesoporosity of the Si nanowire. The scale bars are 10 µm, 200 nm, 50 nm, respectively. [43]

As discussed in the hole injection model of MACE etching mechanism, porosity of the MACE etched structures is induced by the excess holes diffused away from the etching front. Since holes are generated from H_2O_2 reduction, an

increase in H_2O_2 concentration will lead to larger amount of excess holes. The effect of etchant composition (ρ = [HF] / ([H_2O_2] +[HF])) on the etched morphologies was systematically investigated by Chartier et al. using Ag particles coated p-type Si(100) as shown in Figure 2.8.[33] It was found that the porous Si formation was closely related to the etchant concentrations. With 100% > ρ > 70% (i.e. very high HF concentration), straight cylindrical pores were formed with a diameter similar to the size of the Ag nanoparticles as almost all the holes were immediately consumed near the catalysts. When the concentration is changed to 70% > ρ > 20%, pores widened openings were observed as shown in the inset of Figure 2.8(d) & (f). The diameter of the opening of the pore is larger than the Ag nanopaticles, which was caused by diffused excess holes. With very small ρ, the injection of large amount of holes due to high H_2O_2 concentration leads to reduced localized etching and enhanced surface polishing.

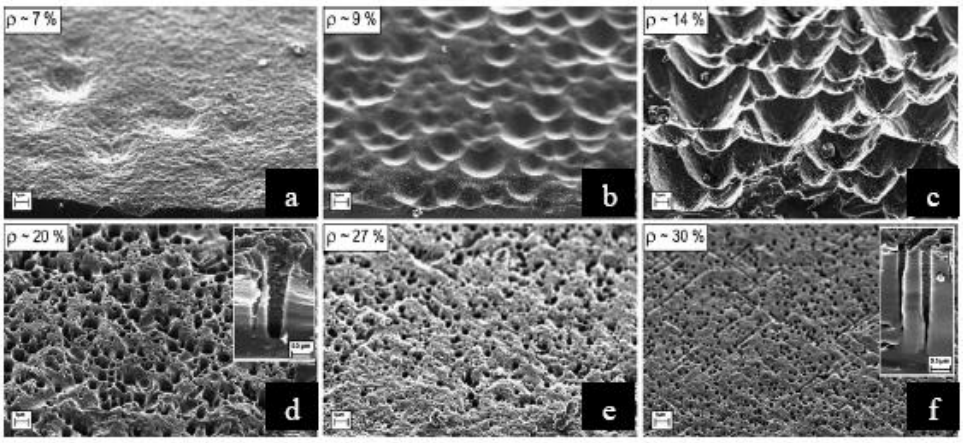

Figure 2.8: SEM results of the surface morphologies of p-type Si(100) samples etched in MACE solution with varied etchant concentrations. [33]

2.4 Application of Silicon Nanowire

2.4.1 Silicon Nanowires for Bioanalytic Applications

Nanomaterial has demonstrated great potential for biomedical applications recently.[2],[29] Substantial efforts have been spent to develop Si nanowires for bioanalytic diagnostic devices because of their tunable surface morphology and surface chemistry, large surface to volume ratio and their comparable size to biological species.[2],[29] Biosensing applications with low cost, fast response and high sensitivity are of particular interest for effective disease diagnosis. Several detection systems have been extensively studied for Si nanowire based bioanalytic devices, including fluorescent sensing, surface enhanced Raman scattering techniques, nanoparticle based techniques, FET based electrochemical sensing and surface plasmon resonance.[44]-[49] Among them, label-free FET based biosensing systems have utilized Si nanowires to achieve highly sensitive detections.[45],[46] When a charged target biomolecule is attached to the surface of a Si nanowire in a FET sensing device, the change in electrical conductance will be detected by electrical instruments.

On the other hand, even though fluorescence sensing methods have advantages in ease of setup, availability of reagents and simple instrument requirements, much less work has been done to integrate Si nanowires into fluorescent detection methods for improved performance. Murthy et al. fabricated DNA microarray using high aspect ratio Si nanopillars.[47] The surface of Si nanowires was functionalized by (3-Aminopropyl)triethoxysilane (APTES) for

immobilization of sense DNA probes. A maximum of 6.5 fold signal intensity increase for DNA detection was observed on Si nanopillar surface as compared to flat Si samples. Similarly, DNA hybridization was also demonstrated on Si nanowires grown by Au catalyzed VLS mechanism as shown in Figure 2.9(a).[48] The fluorescence results in Figure 2.9(b) summarized the signal intensities obtained on the DNA hybridization samples together with negative controls, which indicate that enhanced DNA detection results with good signal-to-noise ratio were obtained on the Si nanowire substrate.

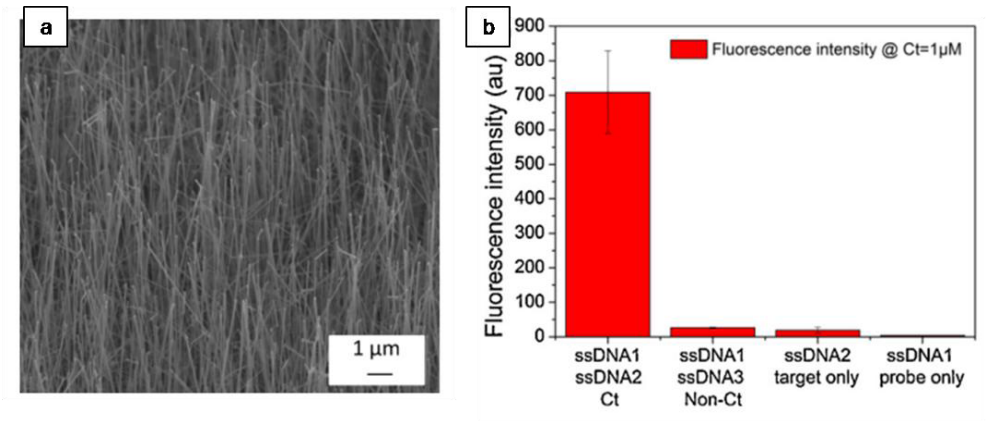

Figure 2.9: (a) Si nanowires grown by VLS mechanism. (b) Fluorescence intensity of complementary antisense DNA on sense DNA, non-complementary antisense DNA on sense DNA, antisense DNA without sense DNA and sense DNA without antisense DNA (from left to right), respectively.[48]

Han et al. reported direct coupling results of protein molecules on MACE (0.03M AgNO3 & 4.9M HF) etched Si nanowires with a height of ~8 µm and a diameter of ~150 nm.[49] Bovine serum albumin (BSA) proteins were immobilized onto the APTES functionalized substrates to evaluate the surface

loading capacity of the Si nanowires, which was 14 times higher than that of flat Si substrates. This platform was further developed for direct coupling of anti-IgG and anti-IgM proteins, with the results summarized in Figure 2.10. As compared to flat Si substrate, the Si nanowire samples showed increased signal intensities of protein detections of up to 7 fold. The detection limits of anti-IgG and anti-IgM on the Si nanowire samples were found to be ~10 ng/ml and 1 ng/ml, while those on flat Si were ~ 10^3 ng/ml. These results indicate that Si nanowire substrates have enhanced protein detection capabilities.

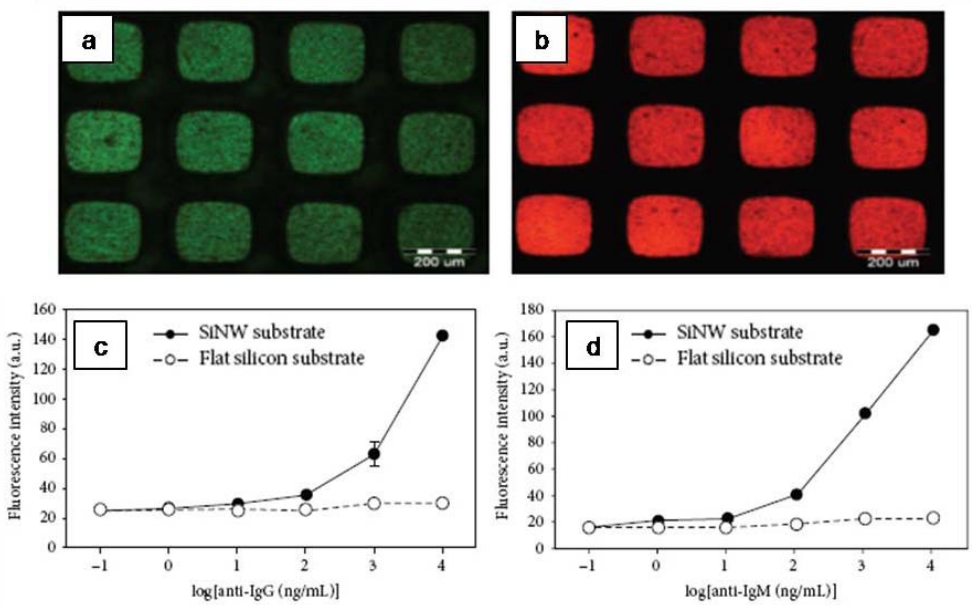

Figure 2.10: Direct protein coupling on Si nanowires and flat Si surface. Fluorescent images obtained from reaction (a) between IgG and FITC-anti IgG and (b) between IgM and Cy3-anti IgM. Fluorescent signal intensities on different substrates with varied concentration of (c) FITC-anti IgG and (d) Cy3-anti IgM.[49]

2.4.2 Silicon Nanowires for Biomimetic Applications

Wettability is a fundamental and essential property of a solid surface, which is determined by both the chemistry and texture of the surface.[50] Study of surface wetting characteristics was originally inspired by functional biological surfaces discovered in nature.[51]-[57] Superhydrophobicity is one of the most interesting wetting properties that keeps solid surface dry by maintaining the ball shape of a water droplet with a contact angle of around 150° or above.[51],[53],[56] Among numerous natural superhydrophobic surfaces, lotus leaves and rose petals with embedded hierarchical surface roughness are the most famous ones owing to their low- and high- adhesion to water droplets, more commonly known as the "lotus effect" and "petal effect".[51],[58]-[60] The surface morphologies of the corresponding lotus and petal surfaces are shown in Figure 2.11. [51],[60]

In the past decades, there have been large amount of studies on artificially replicating the functional wettability of biological surfaces. [51]-[57] As most of the natural surfaces with interesting wettability have complex designs of topographical surface structures in micro- and (or) nanometer scale, controllable and reproducible fabrication techniques of micro- and (or) nanostructures become very important for the biomimetic research. Various approaches have since been used to create surface roughness for mimicking lotus and petal effect.[51], [53],[54],[61] It was demonstrated that tunable water adhesion could be achieved on superhydrophobic surfaces by simply adjusting the roughness and surface chemistry.[60],[62],[63]

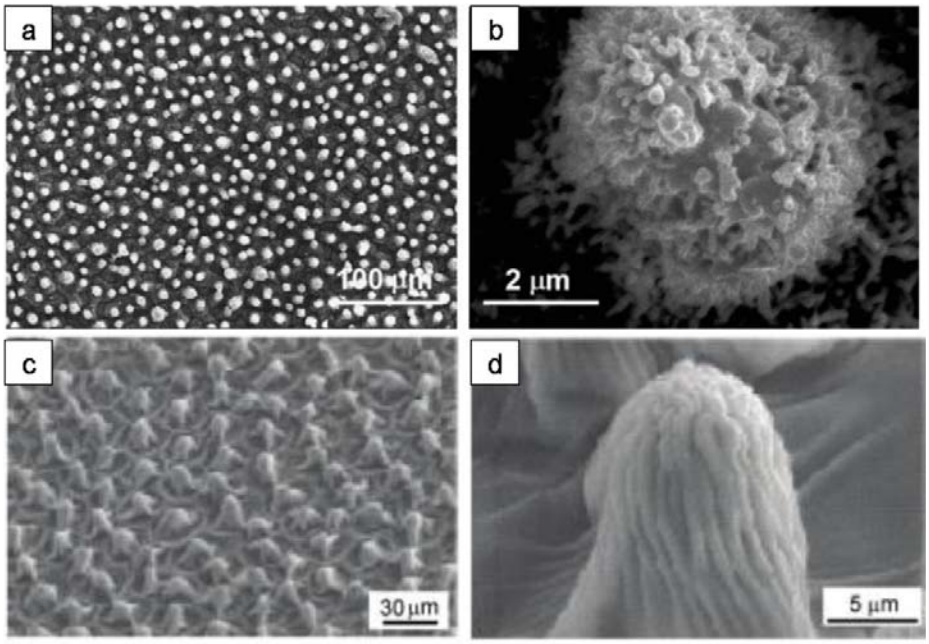

Figure 2.11: Surface texture of lotus leaf with (a) low and (b) high magnification and rose petal with (c) low and (d) high magnification.[51],[60]

One example of the biomimetic studies is the simple method reported by Bhushan and Her to systematically investigate lotus-like and petal-like surfaces created by forming hierarchical structures with epoxy molding (microstructures) and self-assembly of alkane n-hexatriacontane (nanostructures) as shown in Figure 2.12.[60] Superhydrophobic surfaces with both high- and low- adhesion were obtained by tuning the microscale pitch and nanoscale roughness of the surface structures.

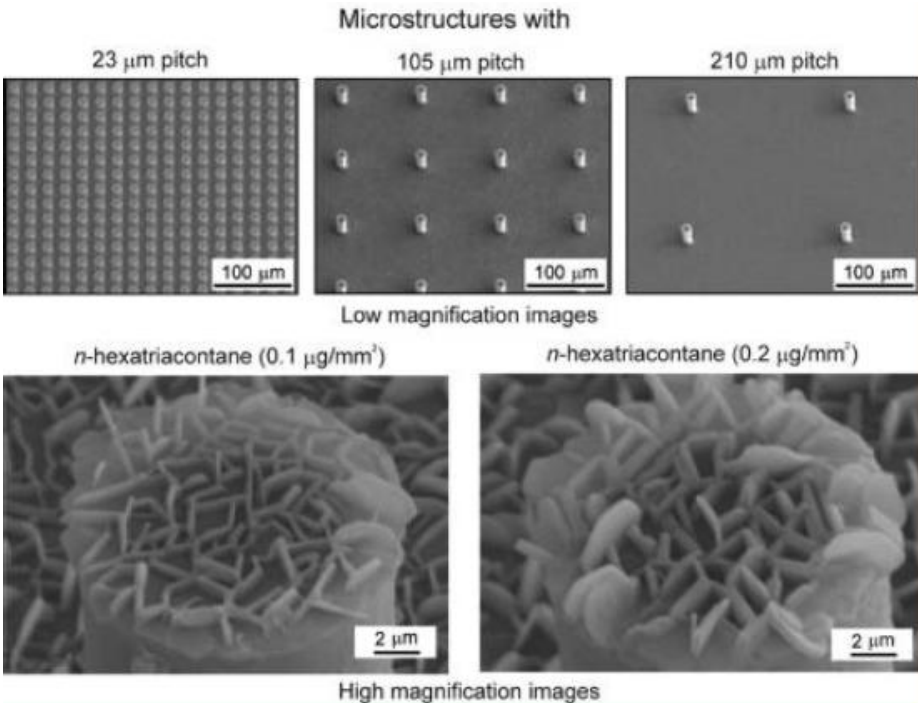

Figure 2.12: SEM images for artificially fabricated samples with hierarchical structures with varied roughness in micrometer and nanometer scale.[60]

2.4.3 Silicon Nanowires for Energy Storage Applications

Lithium-ion micro-battery with high energy storage capacity and long cycle time is an essential module for advanced portable electronic devices. Current rechargeable battery technology suffers from limited performance due to low specific capacity of the commercially available carbon based anode (~372 $mAhg^{-1}$).[64],[65] With a much higher theoretical capacity of ~4200 $mAhg^{-1}$ and a low discharge voltage of ~0.4 V, Si is a promising candidate to replace carbon for battery anode material.[64],[65] However, the alloying and dealloying of lithium-silicon can cause large volume change of Si (up to 400%) during lithiation and delithiation processes, which will lead to pulverization and poor capacity

retention as illustrated in Figure 2.13(a). [30] In order to mitigate such problem, Si nanowires can be integrated into battery anode for its advantages in efficient charge transport along the nanowires, robust electrical connection, facile strain relaxation of the Si nanowires and the ability to accommodate large volume change with sufficient inter-wire space as shown in Figure 2.13(b) & (c).[66]

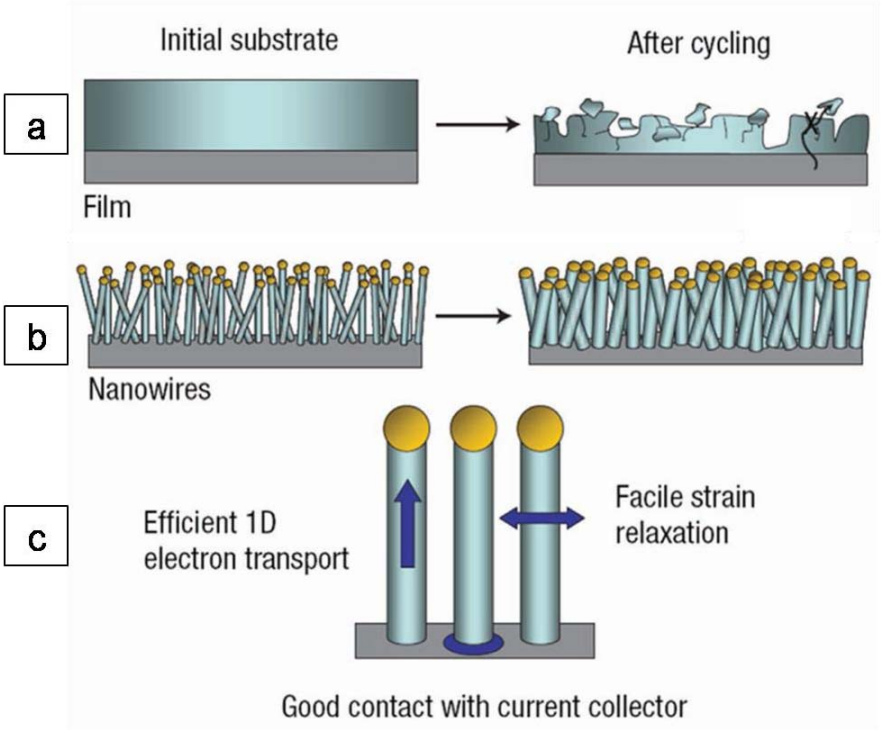

Figure 2.13: Schematic diagrams illustrating the structural change of (a) Si thin film and (b) Si nanowires during cycling. The advantages of Si nanowires as anode material are shown in (c). [30]

Chan et al. reported the first VLS-grown Si nanowire based lithium ion battery with a stainless steel substrate as the anode collector.[30] The morphologies of the Si nanowires before and after cycling are shown in Figure 2.14(a) & (b). The Si nanowires synthesized by VLS method had an average

diameter of ~89 nm and length of larger than 10 μm. After cycling, the Si nanowires had an average diameter of ~141 nm with a much rougher surface. As the Si nanowires accommodated large volume changes and prevented pulverization during cycling, the battery anode maintained a good delithiation capacity of ~3000 $mAhg^{-1}$ after 10 charging and discharging cycles as shown in Figure 2.14(c). Nevertheless, capacity degradation was observed after 16 cycles in a following report from their group.[67] The capacity retained at only 61% after 50 cycles.

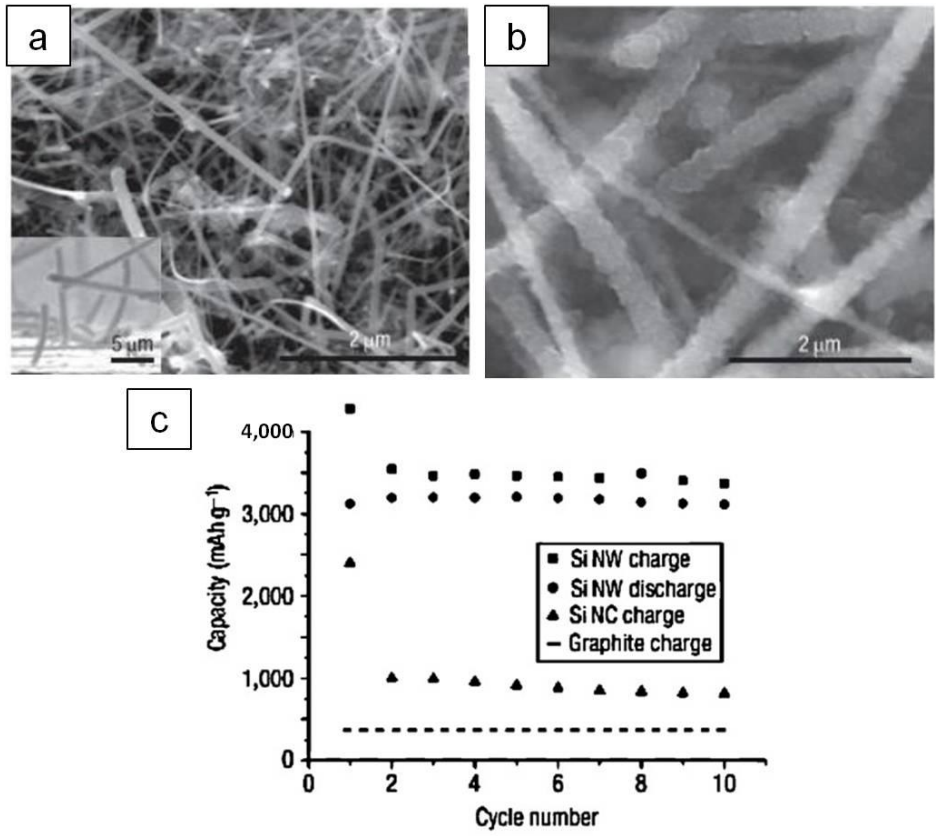

Figure 2.14: SEM image of the VLS-grown Si nanowires (a) before and (b) after lithiation / delithiation processes. (c) is the cycling performance of this Si nanowire based battery.[30]

Metal-assisted chemically etched Si nanowires have also been used as battery anode in the literature.[68],[69] Unlike VLS-grown Si nanowires, the MACE etched Si nanowire do not require additional doping to enhance electrical conductivity. In addition, the increased surface roughness and porosity make MACE etched Si nanowires better candidate for anode material as compared to other types of Si nanowires. Peng et al. presented MACE Si nanowires as anode material with relatively good performance.[68] As shown in Figure 2.15(a) & (b), the MACE Si nanowires remained intact after cycling. As these nanowires were fabricated on a Si substrate, it was not possible to calculate the specific capacity of the lithium ion battery in this experiment due to the contribution of the bulk Si substrate. The cycling capacity of MACE Si nanowires based battery anode was further investigated by Huang et al. by assembling coin cells using MACE etched Si nanowires in Figure 2.15(c).[69] As shown in Figure 2.15(d) & (e), both carbon coated and bare Si nanowires based anodes showed degraded performance within 10-25 cycles, which were possibly due to the poor adhesion between the nanowires and the current collector.

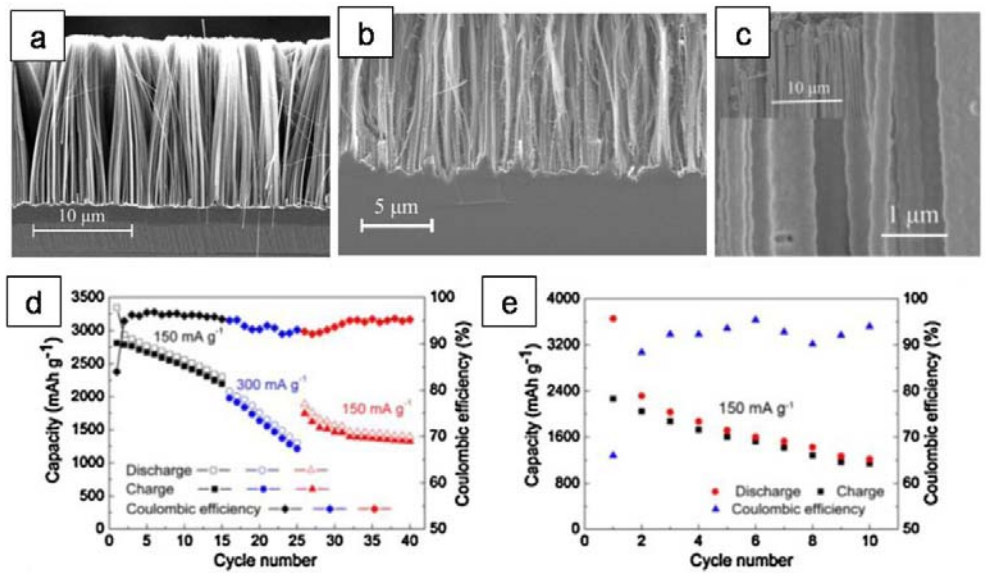

Figure 2.15: Cross-sectional SEM SEM image of MACE Si nanowires (a) before and (b) after cycling. (c) is the SEM images of carbon coated Si nanowires. (d) and (e) are the cycling performance of carbon-coated and uncoated Si nanowire film[68],[69]

2.5 Summary

In this chapter, various bottom-up and top-down Si nanowire fabrication methods were briefly reviewed. This was followed by the introduction of metal-assisted chemical etching of Si for its potential in fabricating Si nanostructures with high aspect ratio, good crystal quality, controlled directionality and high surface porosity. The discussions of MACE focused on the background, etching mechanism, etching rate, etching direction and porosity. The applications of Si nanowires were also review in the research fields of bioanalytic detection platforms, biomimetics of the superhydrophobic lotus and petal surfaces and Si nanowire based lithium ion battery anode.

Chapter 3 Experimental Details

3.1 Introduction

This chapter describes the experimental procedures employed in the sample preparation, fabrication and characterization processes in this study. First, the cleaning and preparation of single-crystal Si wafer and amorphous Si samples will be discussed. Next, the experimental details of interference lithography, optical lithography, thermal evaporation and lift-off processes will be elaborated. This will be followed by a brief description of glancing angle deposition of metal particles. After these patterning steps, metal-assisted chemical etching and thermal oxidation of Si nanowires will be discussed. This Chapter will end with a brief discussion of the characterization techniques, including SEM, TEM, BET and thermoporometry.

3.2 Si Wafer Cleaning

The single-crystal Si substrates used in this study are 2-inch n-type <100> Si wafers with resistivity of 8-12 Ω-cm. Before any processing, the Si wafers were first cleaned using standard two-step RCA cleaning method, which was developed by Kern and Puotinen in 1970.[70] The detailed procedures are described as follows.

SC-1 cleaning is the first step of RCA cleaning of Si wafers. The purpose is to remove organic contamination and particles. The SC-1 solution of a high pH value is made of a mixture of hydrogen-peroxide (H_2O_2), ammonium hydroxide (NH_4OH) and de-ionized water (DI water) in volume ratio of 1:1:5. The Si wafers

were immersed in the SC-1 solution for 10-15 minutes after the solution was heated to 80 - 90 °C, which was followed by rinsing in DI water with nitrogen (N_2) bubbler for another 10 - 15 minutes.

SC-2 cleaning serves to remove most metallic contaminants on the Si wafers. The SC-2 solution of low pH value consists of hydrochloric acid (HCl), H_2O_2 and DI water in volume ratio of 1:1:6. In this step, the SC-1 cleaned Si wafers were immersed in the SC-2 solution at 80 - 90 °C for 10 -15 minutes. After SC-2 cleaning, the wafers were rinsed in DI water with N_2 bubbler again for 10 – 15 minutes. At the end of the RCA cleaning, the wafers were blown dry by N_2 gas.

3.3 Amorphous Si Sample Preparation

The amorphous Si samples used in the energy storage application (Chapter 7) of this study are sputtered Si films on stainless steel substrates. The preparation of amorphous Si samples consists of two steps, which are the preparation of stainless steel substrates and deposition of monolithic Si film by sputtering.

3.3.1 Stainless Steel Substrate Preparation

316-grade stainless steel was used as the substrate material to be deposited with monolithic Si films. The properties of reasonable electrical conductivity, high surface rigidity and low chemical reactivity make stainless steel a good current collector and metal substrate. Discs of 1.2 cm diameter were cut from a sheet of stainless steel with 0.5 mm thickness. The discs were polished to a mirror-finish to provide a flat and uniform surface for the subsequent deposition of Si and fabrication of embedded Si nanowires. The polishing process started

with extensively polishing on the 600 and 800 grit silicon carbide polishing paper, followed by polishing in a suspended alumina solution with progressively finer particle sizes. To remove any residual alumina and contaminant, the stainless steel substrates were cleaned in separate ultrasonic baths in acetone and DI water. Then the samples were blown dry by N_2 gas.

3.3.2 Silicon Sputtering

Amorphous Si was deposited onto the stainless steel substrates by sputtering from an n-doped Si sputtering target (3-inch) with resistivity of 0.005 – 0.020 Ω-cm in a radio frequency magnetron sputtering system at room temperature with an Ar flow rate of 30 sccm. The target was pre-sputtered at 100 W for 10 minutes and 30 W for 5 minutes. The Si sputtering process was conducted at a sputtering power of 30 W, as depositing at higher powers resulted in film delamination in subsequent fabrication processes.

3.4 Native Oxide Removal

Native oxide was formed on single-crystal and amorphous Si samples after the cleaning and preparation processes. It is very important to make sure that native oxide was removed right before the Si nanowire fabrication processes. The native oxide will not only affect the electrical properties of the Si samples, but also lead to fabrication issues in the subsequent processes due to its fast etch rate in hydrofluoric acid (HF) as compared to Si and its poor adhesion with photoresist and metal. The removal methods of native oxide for single-crystal Si wafers and amorphous Si samples are described in the following subsections.

3.4.1 Diluted HF Cleaning

The native oxide on the Si wafers was removed by immersing in 10 wt.% HF for 1 minute. The wafers were rinsed in DI water and blown dry by N_2 gas. The diluted HF cleaning of native oxide was carried out right before the following steps.

- Spin coating of photoresist
- Thermal evaporation
- Glancing angle deposition

3.4.2 BHF Cleaning

The native oxide on the amorphous Si samples was removed by immersing in diluted buffered HF (BHF) solution for 20 seconds. The BHF solution is made of NH_4F, HF and DI water with volume ratio of 6:1:70. The diluted BHF provides relatively good etching selectivity of SiO_2 over stainless steel substrate. After the removal of native oxide, the amorphous Si samples were rinsed in DI water and blown dry by N_2 gas. The BHF cleaning of native oxide was carried out right before the following steps.

- Spin coating of photoresist
- Thermal evaporation
- Glancing angle deposition
- Assembly of half cells for nanostructured anode

3.5 Interference Lithography

Mask-less interference lithography technique was applied in this study to create regular photoresist patterns in nanoscale. A thin layer of photoresist was first spin coated on the Si samples. The photoresist was exposed by interference lithography using Lloyd's mirror setup.[71] The exposed photoresist was developed and the residue was removed by oxygen plasma etching.

3.5.1 Spin Coating of Photoresist

The photoresist used in this work was positive resist Ultra-i 123. The sample was loaded in the spin coater and the surface of the sample was covered by manually dispensed photoresist. The spin coating process includes two steps, which are 6 seconds spin coating at 3000 rpm and following 50 seconds spin coating at 6000 rpm. The two-step configuration was designed for uniform spreading and coating of photoresist on the sample surface. This is followed by a soft bake process at 90 °C for 90 seconds on a hot plate to improve the adhesion of photoresist on the Si surface by driving out excess solvent.

3.5.2 Exposure using Lloyd's Mirror Setup

Lloyd's mirror interference lithography setup is demonstrated in Figure 3.1.[72] The light source is helium-cadmium (He-Cd) laser emitting at 325 nm. The coherent laser beam was focused by a lens to pass through a pinhole to get expanded over a large distance (~ 1 meter). This spatial filter configuration removes high frequency noise from the intensity profile of the laser beam. An UV-enhanced aluminum coating mirror with high reflectance was maintained at

90° to the sample stage, while the intersection point of the setup was located on a rotational stage at the center of the Gaussian profile of the laser output. Lloyd's mirror configuration allows two mutually coherent beams of light to interfere and form a standing wave pattern in the region where the two beams overlap.

The period (p) of the grating patterns exposed on the samples is determined by the wavelength of the light source and the interference angle between the mirror and the optical axis, which is given by

$$p = \frac{\lambda}{(2 \sin\theta)} \tag{3.1}$$

where λ is the wavelength of the light source at 325 nm and θ is half the angle between the two interfering beams.

To create periodic nano-dot pattern, the sample was rotated by 90° for a second exposure for the same duration. In this study, the θ was adjusted from 9° to 18° to obtain patterns with period from ~525 nm to ~1039 nm and diameter of nano-dot from ~262 nm to ~519 nm.

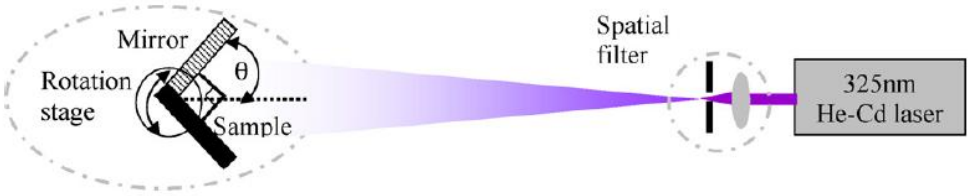

Figure 3.1: Lloyd's mirror interference lithography setup. [72]

3.5.3 Development of Photoresist

After the interference lithography, the sample was baked at 110°C for 60 seconds. The exposed photoresist was removed by immersing the sample in Microposit MF CD-26 developer for 40-60 seconds depending on the exposure power and duration. The samples was then rinsed in DI water and blown dry by N_2 gas.

3.5.4 Oxygen Plasma Etching

It was found that a thin layer of photoresist residue may remain on the exposed region of the Si surface after the exposure and development processes. This residue was removed by oxygen plasma etching at 200 W and 0.2 Torr for 5-15 seconds.

3.6 Optical Lithography

Contact printing of optical lithography was used to create macroscopic photoresist patterns on the surface of the samples employed in this study. The samples coated with photoresist were exposed for 300 – 360 seconds underneath a glass / plastic photo-mask using a UV light source with wavelength of 320 nm. The spin coating, developing and oxygen plasma etching processes used in this technique were similar to what has been described in Section 3.5.

3.7 Thermal Evaporation

After periodic photoresist dots were patterned on the sample surface, the single-crystal and amorphous Si samples were coated with a thin film of noble

metal (Au) using thermal evaporation. A schematic diagram of a thermal evaporator, a physical vapor deposition tool commonly employed for metal deposition, is shown in Figure 3.2. In this process, the required heat was generated by passing an electrical current through a filament (usually in the shape of boat or crucible) of electrical resistive material with high melting temperature (typically Ta, Mo or W). The solid phase metal placed on top of the filament/boat was heated, melted and evaporated in a high vacuum chamber and condensed on the sample surface. This technique is suitable for thin film evaporation of materials of low melting point, such as Al, Cu, Ag and Au. The thermal evaporation process was conducted at a pressure of ~ 3 x 10^{-6} Torr and the deposited film thickness was measured by a crystal oscillator.

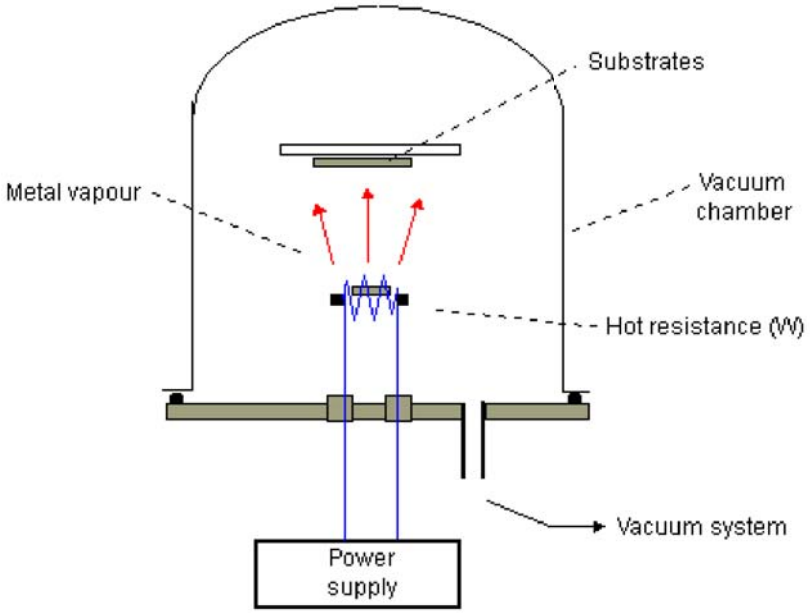

Figure 3.2: Schematic diagram of a thermal evaporator. [73]

3.8 Lift-off

Thermal evaporation was followed by a lift-off process in order to transfer the photoresist patterns into an inverted pattern of metal thin film on the Si samples. In this step, the photoresist features on the samples were removed in an ultrasonic bath in acetone for 5 – 10 minutes. The samples were rinsed in DI water and blown dry by N_2 gas. It is important that native oxide was completely removed before thermal evaporation of metal to avoid detaching of metal thin film on the Si during lift-off.

3.9 Glancing Angle Deposition

Glancing angle deposition technique was used to deposit densely arranged discontinuous metal particles on the Si substrates in this study. The experimental set up is based on a modified E-beam evaporator (see Figure 3.3(a)). In this evaporator, an electron beam is generated from an electron gun and directed to the deposited material by a magnetic field. The electron bombardment heats the metal and causes it to evaporate in a high vacuum environment for thin film deposition.

Unlike conventional thermal evaporation and E-beam evaporation, the sample to be deposited using glancing angle deposition technique is mounted on a rotational stage inside the evaporator with an oblique angle to the deposition flux. The oblique angle configuration leads to lateral growth of the deposited material and the rotation resolves the overall growth direction and surface morphology. The randomly deposited atoms in the initial stage serve as seeds for further growth and the growth rate varies at different locations due to the shadowing

effect as illustrated in Figure 3.3(b). Thus, the resulting thin film deposited by GLAD process may be in a discontinuous or porous form. In this study, the substrate normal of the samples were fixed at 87° to the incoming flux. The evaporation was carried out at a pressure of 10^{-6} Torr with the substrate rotation rate at 0.2 rpm. The progress of the GLAD deposition was monitored by measuring the reference thickness obtained from a crystal oscillator. It should be noted that due to the oblique angle configuration, the recorded reference thickness is not equal to the actual thickness of the deposited material on the sample and the deposited material may not be in the form of a continuous thin film.

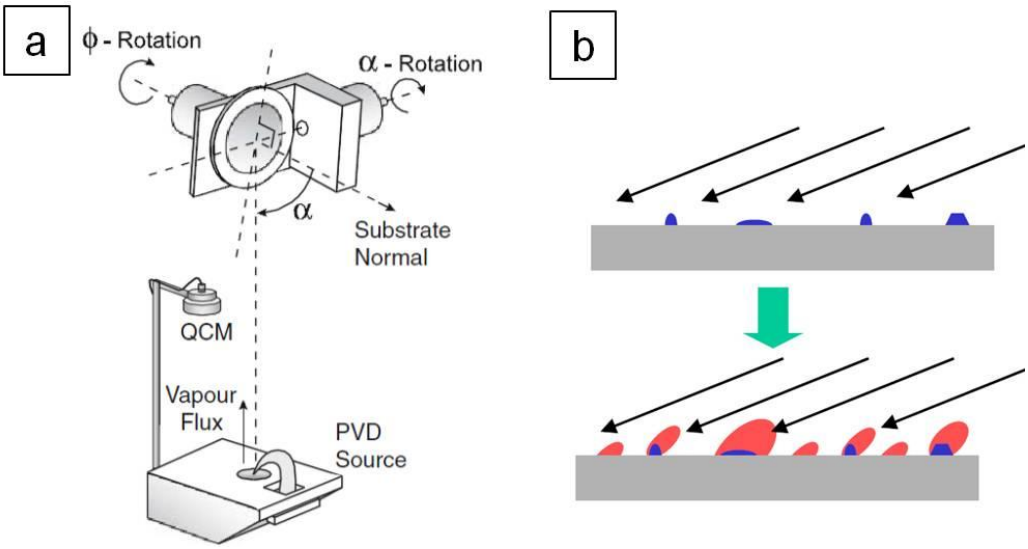

Figure 3.3: Schematic diagram of (a) the glancing angle deposition configuration in an E-beam evaporator [74] and (b) the shadowing effect during oblique angle deposition.[75]

3.10 Metal-Assisted Chemical Etching of Silicon

The noble metal coated on Si surface served as catalyst during the subsequent metal-assisted chemical etching process. The mechanism of metal-assisted chemical etching of Si has been elaborated in Chapter 2. During this pattern transfer process, the Si underneath the metal catalyst is etched much faster as compared to rest of the Si. As a result, the shape, diameter and pitch of the Si nanowires depend largely on the initial morphology of the regular and irregular noble metal patterns defined by interference lithography and glancing angle deposition, respectively. The etching was conducted in a mixed solution of HF, H_2O_2 and H_2O at room temperature. The concentration of the etching solution was fixed at 4.6 M of HF and 0.44 M of H_2O_2 for all experiments. The height of the Si nanowires can be simply controlled by the etching duration. After etching, the samples were rinsed in DI water and dried by N_2 gas.

3.11 Thermal Oxidation

Thermal oxidation was used in this study to oxidize the surface of Si nanowires and the substrate. The oxidation was conducted at 900 °C for 30 minutes with pure O_2 supply to grow a thin layer of oxide (~ 7 nm). Dry oxidation method was used to ensure the oxide film quality. The chemical reaction occurring at the Si surface during dry oxidation is $Si + O_2 \rightarrow SiO_2$.

3.12 Scanning Electron Microscopy

The surface morphology of the samples was examined by high resolution scanning electron microscope (SEM). As illustrated in Figure 3.4(a), in a typical

configuration of SEM, an electron beam is generated from thermionic source or field emission cathode in an electron gun and focused by a condenser or magnetic lens for the required resolution. The scanning position of the focused electron beam can be manipulated by the magnetic field created from the scanning coils. The energy of the electrons may range from 0.1 keV to 30 keV and the beam size can be as small as 1 nm.

When the incident electron beam is scattered in the sample, various signals (e.g. secondary electrons, backscattered electrons and Auger electrons) are generated and the corresponding interaction volume of each signal is depicted in Figure 3.4(b). Standard SEM detects the signal of secondary electrons and backscattered electrons emitted from the sample. Secondary electrons are low energy electrons formed through inelastic collisions between the incident electrons and the outer electrons of the sample atoms. Only the secondary electrons near to the sample surface can be emitted, therefore, the signal of secondary electrons can respond according to the surface topology and provide the information of the surface morphology of the sample. Backscattered electrons are high energy electrons ejected from the sample after a series of elastic collisions between the primary electrons and sample atom's nucleus. As the signal is related to the atomic number of the material, backscattered electrons are more often used to provide information on the material composition of the sample. In this work, the SEM analysis was conducted using FEI NOVA NanoSEM 230 at an accelerating voltage of 5 to 15 keV.

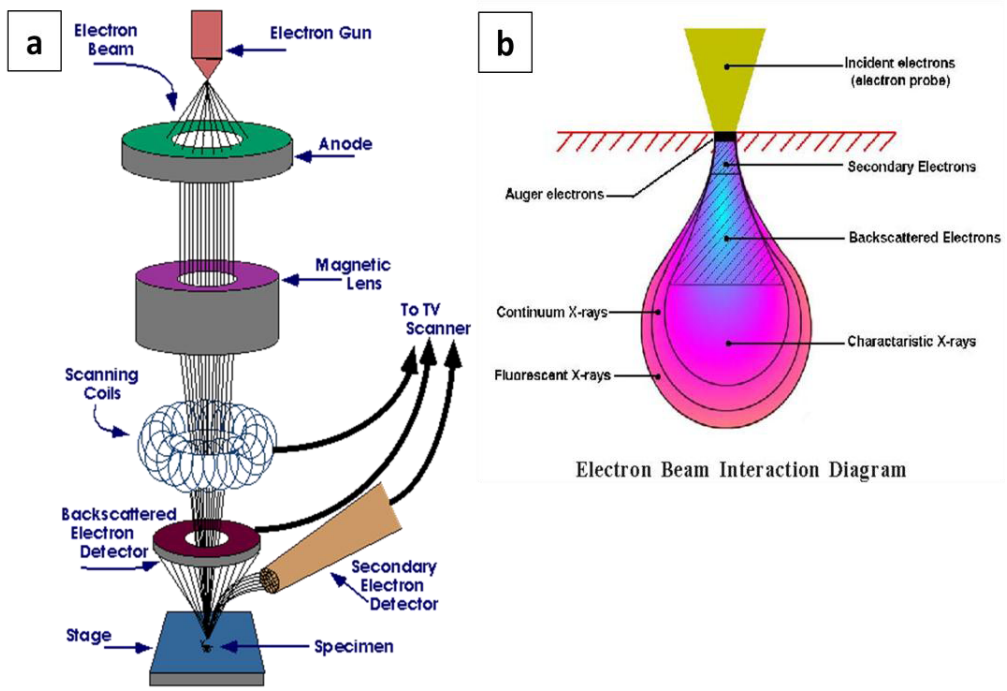

Figure 3.4: Schematic diagram of (a) the SEM configuration and (b) the various signals generated in the sample when an incident electron beam is scanned on the surface. [76]

3.13 Transmission Electron Microscopy

Transmission electron microscopy (TEM) is an advanced microscopy technology with very high resolution. TEM images can provide clear image of crystal structure, crystal defect and grain size at atomic level. In this work, Si nanowires were manually scraped off the samples with a clean razaor blade. The collected powder form sample was dispersed and ultrasonicated in methanol to avoid agglomeration and collected by a carbon-coated copper grid. The TEM microscopy was carried out using JEOL 2010F TEM system. In typical TEM configuration (see Figure 3.5), the electron beam is accelerated at high voltage (100 – 1000 keV) and focused on the sample by condenser lenses. After the

electrons transmit through an ultra-thin sample, the image and diffraction patterns of the samples can be formed by an objective lens in the back focal plane and image plane, respectively. In image mode shown in Figure 3.5(a), an objective aperture is inserted in the back focal plane to select the transmitted beam. In diffraction mode shown in Figure 3.5(b), the back focal plane is taken as the objective plane for intermediate lens and projective lens. The diffraction or imaging signal carrying the structural information of the sample is magnified by intermediate lenses and recorded by an imaging device (fluorescent screen, photographic film) or light sensitive sensor (e.g. CCD camera).

Successful imaging of nano-material using TEM is highly dependent on the contrast obtained. Contrast of TEM image is related to the absorption of electrons in the sample and varies with different sample thickness and composition. It can be generated in several ways via different operation modes. In image mode, diffraction contrast is generated by aperture in objective lens in the back focal plane. The aperture diameter determines diffraction contrast for low magnification (resolution larger than 1 nm) images. In addition, the aperture position is also related to the operation mode of TEM. When the objective aperture is located at the center of direct beam on the back focal plane, TEM is working in bright field imaging mode and the strongly diffracting area is dark. When the direct beam is blocked, it is under dark field mode and the region without sample appears dark. As compared to diffraction contrast, high-resolution images are based on phase contrast. The sample is illuminated by parallel electron

beams and the HRTEM image is formed by the different phases of the incident electron wave.

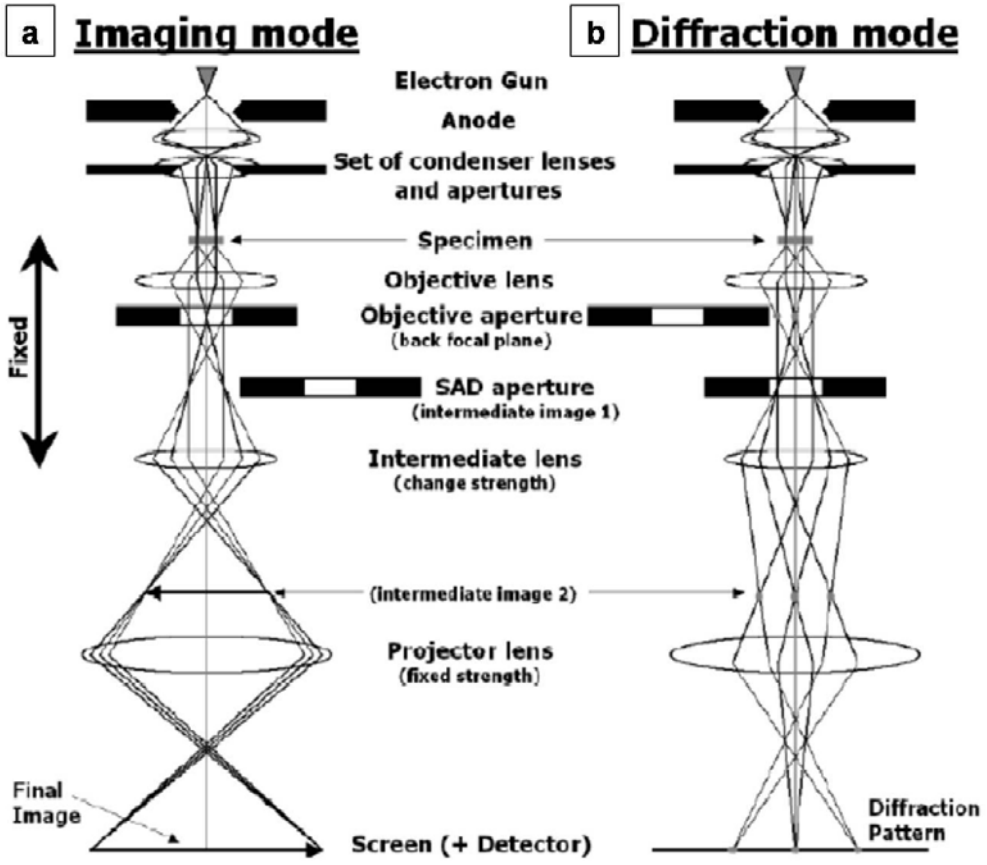

Figure 3.5: TEM configuration diagram illustrating the image formation in (a) imaging mode and (b) diffraction mode.[77]

3.14 BET Gas Sorption

BET gas adsorption/desorption method is a reliable method to characterize nanoporous material. Gas sorption experiment is designed to quantitatively analyze the actual surface area of solid substance, including the surface irregularity and porosity, which cannot be simply calculated based on the shape and size of the solid material. Physical sorption of gas molecules on solid surface

is not only determined by solid surface area, but also temperature, gas pressure and interaction between solid surface and gas. Therefore, when the temperature is fixed, the amount of gas adsorbed at given pressure allows us to determine the surface area of the solid substance.

To start the gas sorption experiment, the sample was first purged with inert gas (e.g. N_2) while being heated at 100 – 250 °C for a few hours to remove surface moisture and volatile contamination. Then, it was evacuated and cooled to a low temperature of 77 K, the temperature of liquid nitrogen, to facilitate measurable adsorption. The gas adsorption process began by exposing the sample to the adsorptive (i.e. the gas to be adsorbed) at very low relative pressure. The filling of micropores (diameter smaller than 2nm) is the dominating effect at this stage. As the relative pressure of the gas increased, the gas molecules started to be adsorbed on the solid surface. The total surface area of the sample can be calculated when a complete monolayer of gas molecules were formed on the sample surface. It should be noted that the gas sorption process would not stop after monolayer adsorption. Additional molecules continued to be adsorbed to form multiple molecular layers. At higher relative gas pressure, the mesopores (diameter in between 2 nm and 50 nm) started to be filled, which was named as capillary condensation. When the pores were fully filled, the equilibrium state was reached and the isotherm continued with the gas desorption process at a reducing pressure.

BET model, introduced by Brunauer, Emett and Teller in 1938, was developed to determine the surface area and pore size distribution of finely

divided and porous substances based on the data obtained from gas sorption experiments. BET theory was built from Langmuir isotherm of monolayer adsorption and modified for multilayer gas sorption. The model was built with the assumptions: (1) homogeneous surface, (2) no interaction between adsorbed molecules, (3) uppermost layer is in equilibrium with vapor phase and (4) infinite gas molecule layers adsorb on the solid surface at saturation pressure.

The mathematical equation of the BET model is given in equation (3.2)[78]

$$\frac{1}{V[(P_0/P)-1]} = \frac{1}{V_m C} + \frac{C-1}{V_m C}\left(\frac{P}{P_0}\right) \tag{3.2}$$

Where P/P_0 is the relative pressure of the inert gas (P_0 is the saturation pressure of the adsorptive at a given temperature), V is the amount of gas adsorbed, V_m is the quantity of gas adsorbed for a monolayer, C is an empirical BET constant indicating the strength of adsorbent-adsorbate interaction. BET model was usually employed to calculate the sample surface area with the data from the isotherm in the classic range of $0.05 < P/P_0 < 0.3$.

The BET gas sorption experiments in this work were performed with a Quantachrome NOVA 4200e surface area and pore size analyzer. The pore size distribution and total pore volume were estimated by the Barrett−Joyner−Halenda (BJH) model, which was built based on the modified Kelvin equation. The Si nanowires were manually scraped off the samples with a clean razaor blade and collected in a glass tube for degassing for 2 hours at 120°C before gas sorption experiment. The experimental data of the mesoporous Si samples were analyzed by Quantachrome NovaWin 11.0.

3.15 Thermoporometry

Thermoporometry, also known as thermoporosimetry, is a sensitive calorimetric method that determines surface porosity and pore size distribution of a porous material based on the melting or crystallization point depression of a liquid filling a porous structure.[79],[80] As compared to the conventional porosity measurement methods (e.g. mercury intrusion, BET gas sorption), thermoporometry is a relatively new method that makes use of differential scanning calorimeter (DSC) to precisely measure the small temperature shifts due to exothermic freezing and endothermic melting transitions. The solid-liquid phase transition shift of the triple point temperature for a liquid confined in pores is determined by the radius of curvature of the interface between the solid and liquid phases, which is often referred to the pore size.

The working principle is based on a thermodynamical relationship known as the Gibb-Thomson equation. The relationship between the shift of triple point temperature of a condensate (confined solvent) in the porous material and the radius of the pore where the phase transition occurs is shown in equation (3.3).[80]

$$\frac{\Delta T}{T_0} = \frac{2\gamma_{ls}}{\Delta H_0}\frac{\nu_l}{R_p} \qquad (3.3)$$

where γ_{ls} is the liquid-solid interfacial tension, ΔH_0 is the molar heat of fusion, ν_l is the liquid phase molar volume, R_p is the pore radius, and the phase transition shift of temperature is given by $\Delta T = T - T_0$, with T_0 being the triple point temperature of the liquid. The difference in phase transition temperature, ΔT,

between confined and bulk solvent can be detected calorimetrically by differential scanning calorimetry (DSC). This can be re-written as equation (3.4).[80]

$$R_p = -\frac{A}{\Delta T} + t \tag{3.4}$$

where A is a constant depending on the solvent and t is the thickness of the layer of solvent which is not involved in the freezing or melting, but remains adsorbed on the surface of the pore.

The sample preparation procedure for thermoporometry measurement is relatively simple. Commonly used liquid probe for this technique include water, benzene, nitrobenzene, etc. The sensitivity of this characterization method relies on the choice of filling liquid. Water is a common probe liquid, which is relevant for examining materials and coatings designed specifically to absorb aqueous solutions. More importantly, the large enthalpy of fusion of water (ΔH_f = 334 J/g) allows sensitive measurement using DSC technique for samples supplied in low quantity.

The TPM measurements were performed on a Mettler Toledo DSC I with an HSS2 sensor and a heat-flow sensitivity of 0.2 μW. DI water (16 MΩ, Millipore Milli-Q system) was chosen as the pore-filling liquid to allow a lower sample heating rate for improved sample equilibration and peak resolution. Prior to DSC measurements, the samples were immersed in water and placed in a vacuum for degassing for at least 2 hours. The samples were flash frozen to -50 °C or less, and the melting curves were taken at heating rates of between 0.5 °C/min and 10 °C/min.

Chapter 4 Synthesis and Characterization of Metal-Assisted Chemically Etched Silicon Nanowires

4.1 Introduction

In this chapter, the fabrication methods and characterization results of metal-assisted chemically etched Si nanowires will be discussed. The process flow and preparation procedures will be presented for both IL-MACE and GLAD-MACE Si nanowire substrates. As single crystalline Si substrate and sputtered amorphous Si on stainless steel plate will be used for different applications in this report, the SEM surface morphology analysis for IL-MACE and GLAD-MACE samples will be separately discussed for different substrates. In addition, the surface roughness and porosity of the GLAD-MACE nanowires will be investigated by TEM. This chapter will end with quantitative surface porosity analysis of the metal-assisted chemically etched Si nanowires by BET gas sorption and thermoporometry methods.

4.2 IL-MACE Si Nanowires

IL-MACE method was used to create ordered Si nanowires on Si surface. The fabrication process flow is shown in Figure 4.1. Cleaned Si samples (single crystalline Si wafers or sputtered amorphous Si on stainless steel substrates) of size ~ 1 cm^2 were coated with a thin layer of photoresist (Ultra-i 123) and cured at 90°C for 90s. After two perpendicular IL exposures for 1 min, the samples were developed in CD26 solution for ~ 40 seconds and cleaned by oxygen plasma etching to remove any photoresist residue. Au was thermally evaporated onto the

patterned Si substrates to a thickness of ~15 - 25 nm at a pressure of ~ 3 x 10^{-6} torr. Photoresist lift-off process was conducted in an ultrasonication bath of acetone for ~ 10 minutes. Then the samples were etched in a mixed solution of H_2O, HF and H_2O_2 at room temperature, with the concentrations of HF and H_2O_2 fixed at 4.6 M and 0.44 M, respectively. The height of the IL-MACE Si nanowires was controlled by etching duration. The samples were rinsed in DI water and dried by a nitrogen gun after the etching process. The remaining Au was removed using a standard Au etchant.

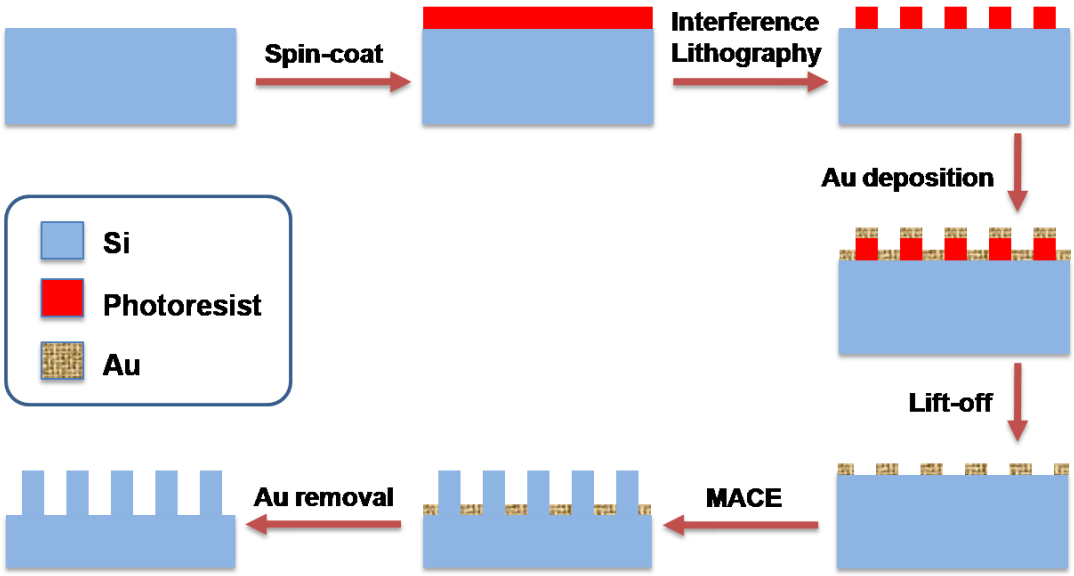

Figure 4.1: Schematic diagram of the fabrication process flow for IL-MACE Si nanowires.

4.2.1 IL-MACE Si Nanowires on Si wafer

IL technique was used to create regular photoresist nano-dot patterns with period ~1 μm and diameter of from ~300 nm to ~500 nm. The SEM results of IL patterned photoresist features on Si surface are presented in Figure 4.2(a). The

oxygen plasma cleaning may further shrink the diameter of the photoresist dots while maintaining the period of the pattern. With a thin film of Au evaporated onto the photoresist patterned Si wafer, the IL defined regular pattern can be transferred to single crystalline Si by MACE. Figure 4.2(b) shows periodic IL-MACE Si nanowires with good uniformity over large area. The inset of Figure 4.2(b) reveals that the IL-MACE Si nanowires are aligned perpendicular to the sample surface and the diameter remains nearly constant along the nanowires.

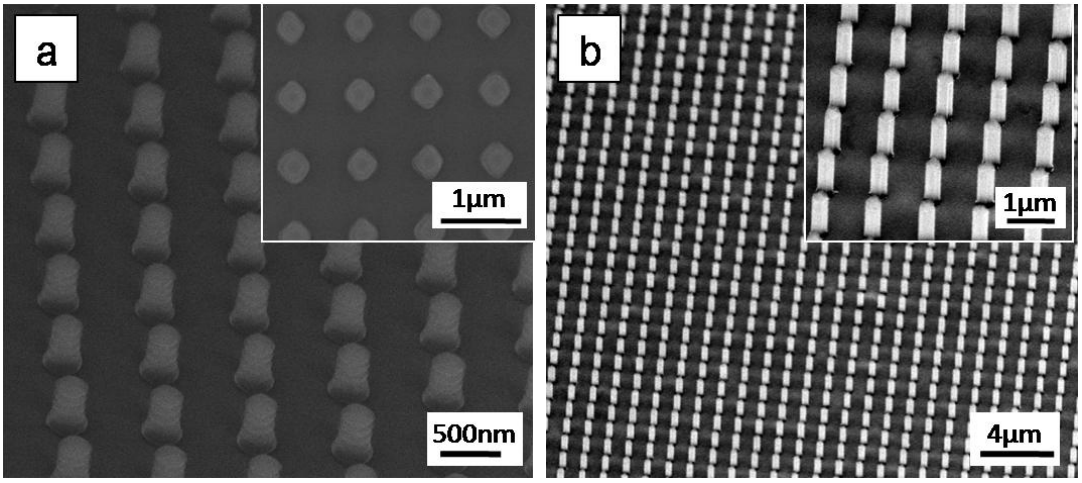

Figure 4.2: SEM images of (a) IL patterned regular photoresist nano-dots and (b) zoom-out view of regular IL-MACE Si nanowires fabricated on a Si wafer. The inset of (a) is the top view image of the photoresist nano-dots. The inset of (b) is high magnification tilted SEM image of IL-MACE Si nanowires.

4.2.2 IL-MACE Si Nanowires on Stainless Steel Substrate

Regular IL-MACE nanowires were also created on sputtered amorphous Si thin film on stainless steel substrate as anode material for Lithium ion battery application in Chapter 7. Figure 4.3 shows the nanowires with a height of 450 nm

and 750 nm. The etching process was carefully controlled to leave a residual Si thin film layer underneath the IL-MACE nanowires for better adhesion. The SEM images in Figure 4.3 were taken before battery testing and were used as a reference to compare with the surface morphology after lithiation/delithiation.

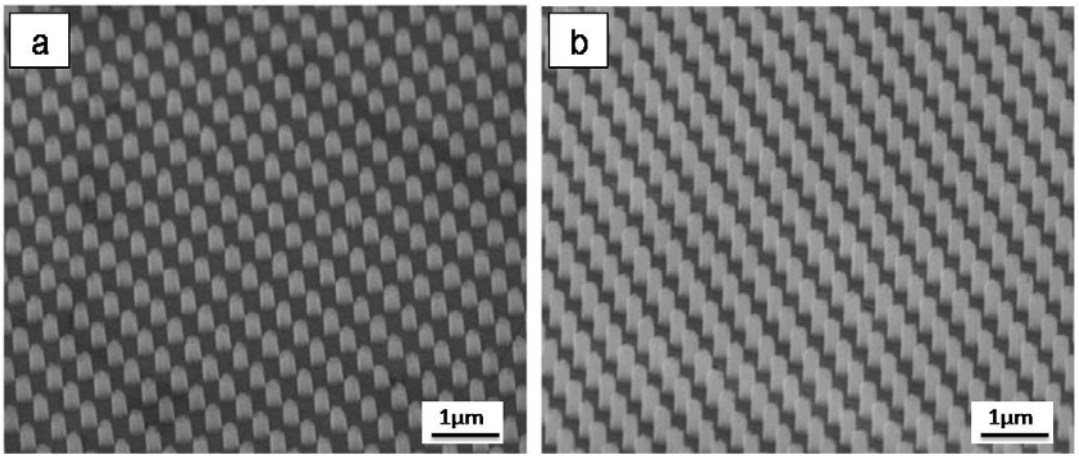

Figure 4.3: SEM images of sputtered IL-MACE Si nanowires with height of (a) 450 nm and (b) 750 nm.

4.3 GLAD-MACE Si Nanowires

GLAD-MACE is a mask-less, highly scalable technique for fabrication of randomly located Si nanowires on Si surface. The process flow for GLAD-MACE Si nanowire fabrication is depicted in Figure 4.4. Cleaned Si samples (single crystalline Si wafers or sputtered amorphous Si on stainless steel substrates) of large surface area were subjected to native oxide removal in diluted HF solution prior to loading into an electron-beam evaporator. The chamber was pumped down to the pressure of ~1 x 10^6 torr before commencing the GLAD process. The substrate normal was placed at an angle of 87° to the direction of the incoming

flux and the substrate was rotated at a rate of 0.2 rpm. The evaporation process was stopped when the reference thickness of the deposited Au (or other noble metal) reached 200 nm unless specified otherwise. The samples were then etched in a mixed solution of H_2O, HF and H_2O_2 at room temperature with the concentrations of HF and H_2O_2 fixed at 4.6 M and 0.44 M, respectively. The height of GLAD-MACE Si nanowires was modulated by different etching duration. The samples were rinsed in DI water and dried with a nitrogen gun after the etching process. Finally, the samples were immersed in a standard Au etchant to remove the remaining Au on the surface.

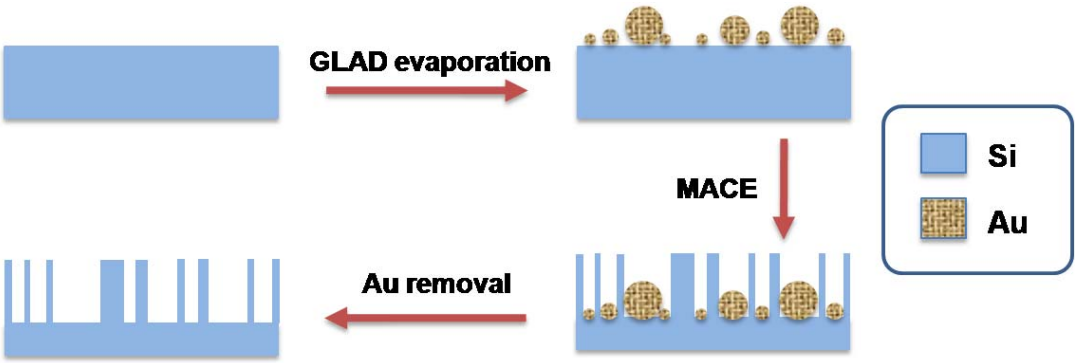

Figure 4.4: Schematic diagram of the fabrication process flow for GLAD-MACE Si nanowires.

4.3.1 GLAD-MACE Si Nanowires on Si wafer

Noble metal (e.g. Au) serves as catalyst during MACE of Si. In fact, the Si underneath noble metal can etch with a much higher rate as compared to the rest of the region, as a result, the shape, diameter and period of metal-assisted chemically etched Si nanowires are highly related to the initial morphology of Au on Si surface. To create densely located Si nanowires with small diameters,

GLAD was employed to deposit close-packed Au nanoparticles with a wide distribution of sizes on Si surface as shown in Figure 4.5(a). A clearer view of Au nanoparticle network deposited by GLAD (200 nm in reference thickness) presented in the inset of Figure 4.5(a) reveals many smaller nanoparticles embedded in vicinity to the larger ones. This distribution of nanoparticles were formed due to shadowing effect associated with the GLAD process, which caused larger particles to continue to grow while smaller particles stopped growing once they were shadowed by larger particles nearby.[81] During MACE, Au nanoparticles sank collectively into Si and the resulting etching profile is shown in the tilted view and top view SEM images in Figure 4.5(b). The GLAD-MACE Si nanowires with extremely high aspect ratio were prone to bend due to capillary force exerted on the nanowires during the drying process after etching.[82] The clumped nanowires formed into permanent nanoclusters by short-range van der Waals force after the samples were completely dried.[83] GLAD-MACE Si nanowires were found to be completely mesoporous according to the TEM image shown in Figure 4.5(c). The high porosity also explains the poor rigidity of the Si nanowires, which will be further elaborated in Chapter 6.[84]

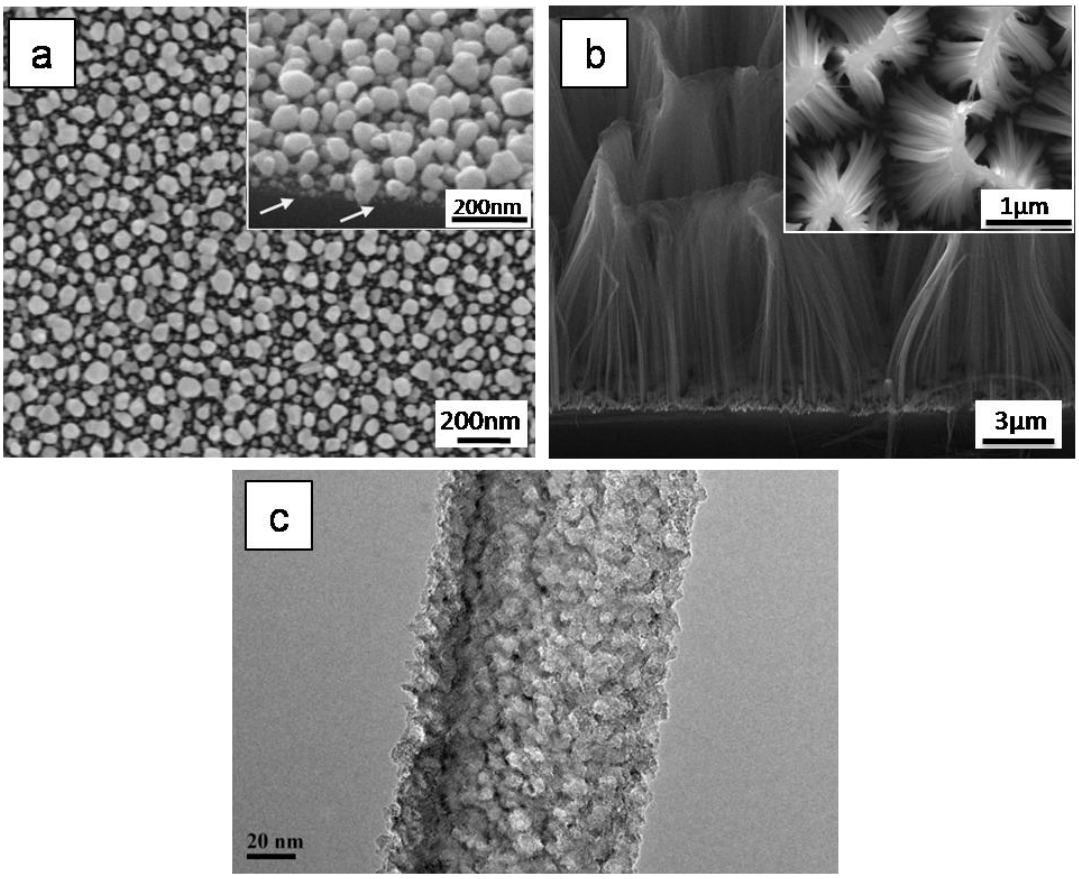

Figure 4.5: SEM results of (a) top view image of Au nanoparticles deposited by GLAD for 200nm in reference thickness and (b) tilted view image of resulting GLAD-MACE Si nanowires with etching duration of 20 minutes. Inset of (a) is the tilted view image of Au nanoparticles formed by shadowing effect of GLAD. Inset of (b) is the top view SEM image of GLAD-MACE nanowires. (c) is the TEM image of a GLAD-MACE nanowire.

4.3.2 GLAD-MACE Si Nanowires on Stainless Steel Substrate

Similar to the IL-MACE samples in Section 4.2.2, GLAD-MACE nanowires were fabricated on sputtered amorphous Si thin film on stainless steel

substrate for Lithium ion battery application. The GLAD conditions were exactly the same as those for single crystalline Si nanowires. Figure 4.6 shows the dense amorphous GLAD-MACE nanowires with a height of 450 nm and 750 nm. The etching process was carefully controlled to keep a residual Si thin film layer underneath the nanowires for better adhesion. The SEM images were compared with the morphology of the samples after lithiation/delithiation for battery performance evaluation.

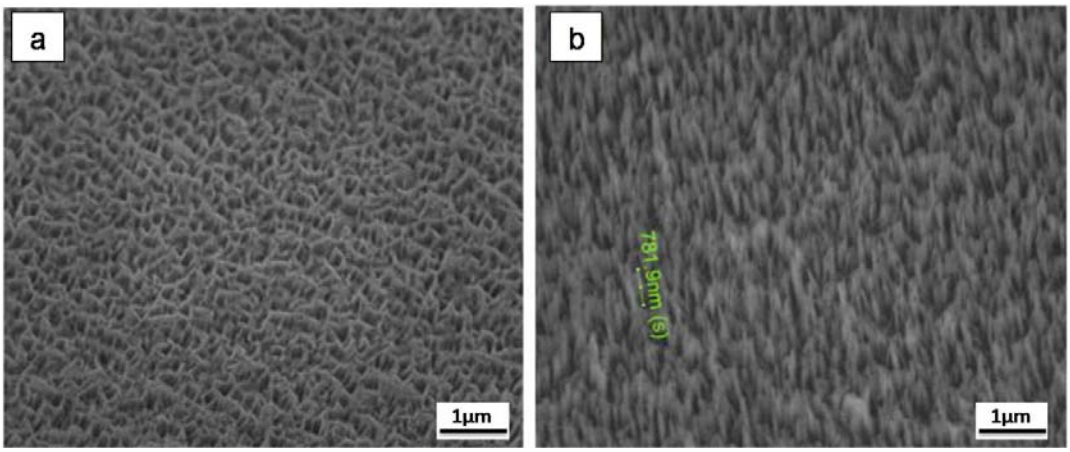

Figure 4.6: SEM images of sputtered GLAD-MACE Si nanowires with height of (a) 450 nm and (b) 750 nm.

4.4 Surface Porosity Characterization of Metal-Assisted Chemically Etched Si Nanowires

Porosity is a unique property for metal-assisted chemically etched Si nanowires. As a matter of fact, the formation of porous regions in the vicinity to the noble metals has been widely reported in the literature.[32],[33],[85],[86] MACE is a redox reaction comprising of oxidation and reduction at anode and cathode.[32],[87] Noble metals catalyze the reaction to inject large amount of

holes into Si during the charge transfer process of MACE.[32],[88],[89] As the holes cannot be completely consumed at the etch front, the excess holes may diffuse to the region nearby and cause the formation of porous surface on the etched structures.[33] Mesoporous structures have been clearly observed on GLAD-MACE Si nanowires as shown in Figure 4.5(c). The surface of IL-MACE Si nanowires are actually also porous but to a lesser extent. Even though the porosity cannot be observed from the SEM images in Figure 4.2, it can be indirectly proven by the fast oxide formation for porous structure in ambient environment. Dawood et al. reported that the top part of IL-MACE Si nanowires were porous as cone shape Si core was obtained by dipping the ambient oxidized IL-MACE nanowires in diluted HF.[90] Since porosity affects many properties of nanowires, including surface area and mechanical strength, it is crucial to study this factor in a quantitative manner. The results of BET gas sorption and thermoporometry surface porosity analysis will be presented in the following sections.

4.4.1 BET Gas Sorption Analysis

BET gas sorption is a classic surface porosity measurement method with well-established theories.[78] BET has been previously used to investigate the porosity of metal-assisted chemically etched highly doped p-type Si nanowires by Hochbaum et al. In this study, GLAD-MACE Si nanowires (~37.6mg) were scraped and collected from multiple wafers prepared with the same recipe. The adsorption and desorption isotherms are plotted in Figure 4.7(a). A mean surface area of 75.68 m^2/g was obtained from multipoint BET analysis and the pore

volume is 0.115 cm^3/g as concluded by BJH analysis. As shown in Figure 4.7(b), the peak of the pore size distribution occurs at 3.86nm, which is consistent with the mesoporous structure observed in the TEM image in Figure 4.5(c). It should be noted that BET gas sorption analysis requires large amount of porous sample in powder phase, which makes it difficult to work on samples with low porosity. More importantly, the fabrication of IL-MACE Si nanowires has much lower throughput as compared to GLAD-MACE process. Therefore, the porosity result of IL-MACE Si nanowires cannot be obtained using BET method.

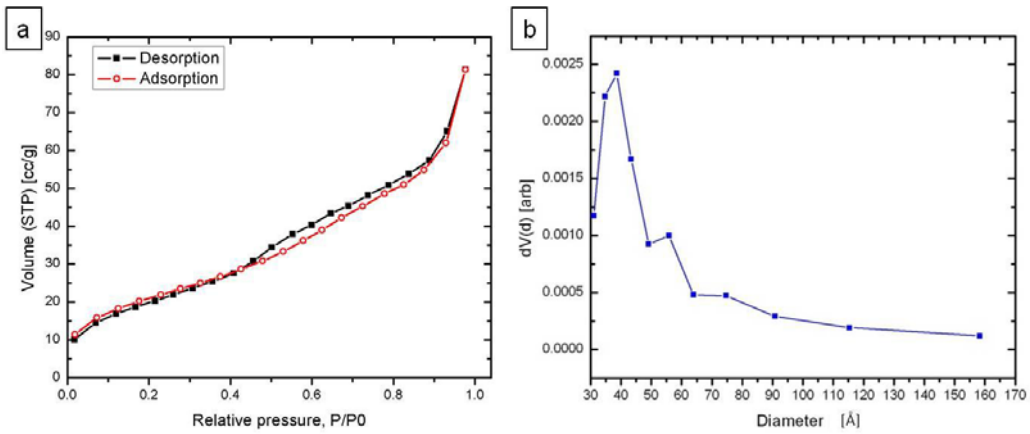

Figure 4.7: BET surface porosity analysis of GLAD-MACE Si nanowires. (a) is the plot of gas sorption isotherm. (b) shows the estimated pore size distribution of GLAD-MACE Si nanowires calculated by BJH model.

4.4.2 Thermoporometry Characterization

Thermoporometry is a sensitive method to measure the porosity by detecting the difference in phase-transition temperature of the material trapped inside pores versus bulk phases. Both GLAD-MACE and IL-MACE Si nanowires (10 – 15 μm in height) were investigated using this method. The pore size

distribution results are shown in Figure 4.8. The GLAD-MACE nanowires have much stronger signal (pore diameter in the range of 5 nm to 8 nm) as compared to IL-MACE samples. The calculated results are summarized in Table 4.1. Little difference was observed for the results obtained using different assumptions of the pore shape (z). The pore diameter of IL-MACE nanowires are ~4 times of that for GLAD-MACE diameters. However, the total pore volume and total surface area of GLAD-MACE nanowires are ~10 and ~50 times larger than that of IL-MACE nanowires. These results indicate that the thin GLAD-MACE nanowires have smaller but much denser mesopores as compared to IL-MACE nanowires. The advantage of this method is that it requires smaller amount of sample (~15-20 mg) and much shorter characterization duration (10 – 80 minutes) as compared to BET gas sorption.

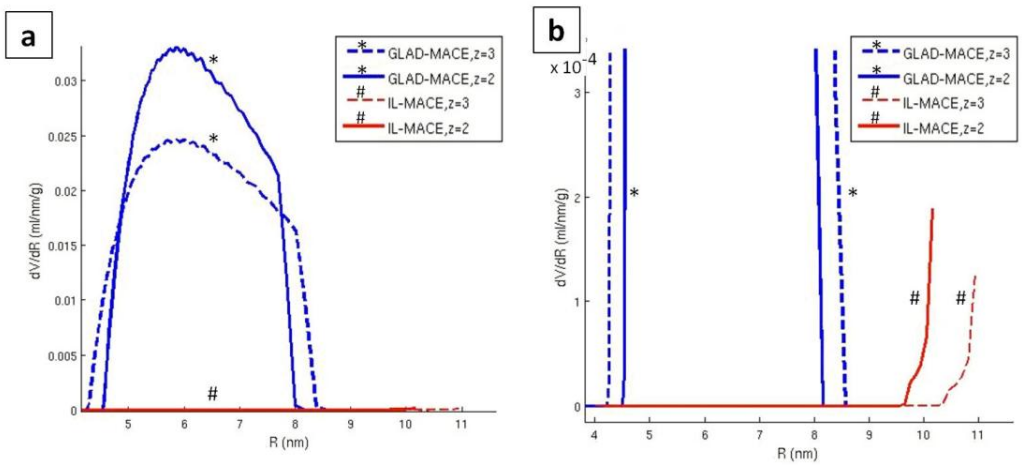

Figure 4.8: (a) Pore size distribution (PSD) of GLAD-MACE and IL-MACE nanowire samples calculated from thermoporometry results obtained from a heating rate of 5°C/min (b) Zoomed in view of IL-MACE nanowire PSD plot. (z is the shape factor for the presumed shape of the pores, which is equal to 2 or 3 for cylindrical or spherical pores, respectively.)

Table 4.1: Calculated values of the pore diameter (Rp), total pore volume (V_{DSC}), and total pore surface area (A_{DSC}) of GLAD-MACE and IL-MACE nanowires based on thermoporometry results. (z is the shape factor for the presumed shape of the pores, which is equal to 2 or 3 for cylindrical or spherical pores, respectively.)

	GLAD-MACE		IL-MACE nanowires	
	$z = 2$	$z = 3$	$z = 2$	$z = 3$
R_p (nm)	5.86	5.90	20.48	23.07
V_{DSC} (mL/g)	0.087	0.078	0.0085	0.0084
A_{DSC} (m^2/g)	54.30	51.24	0.93	0.91

4.5 Summary

In this chapter, the process flow and preparation methods for IL-MACE and GLAD-MACE Si nanowires were introduced. The surface morphology of the Si nanowires on Si wafers and sputtered Si thin film on stainless steel substrates were investigated. The porosity of GLAD-MACE nanowires was confirmed by TEM. To quantitatively study the porosity of GLAD-MACE and IL-MACE nanowires, BET gas sorption and thermoporometry methods were used to determine the pore size distribution, total pore volume and total surface area of the samples.

Chapter 5 Silicon Nanowires for Bioanalytic Applications

5.1 Introduction

In this chapter, the bioanalytic results of DNA and DNA directed analyte captured on metal-assisted chemically etched Si nanowires will be discussed. The novel capturing strategy adopted in this study will be firstly introduced. This will be followed by the experimental conditions for substrate fabrications, surface loading capacity measurements and DNA, protein and sepsis capture. Next, the surface loading capacities of Si nanowire substrates fabricated by different methods will be evaluated. The contribution of surface area and surface porosity to the loading capacity will be further discussed. Last but not least, the bioanalytic capability of the Si nanowire substrates will be presented by the successful capturing results of DNA, protein and sepsis on GLAD-MACE microarrays.

5.2 Capturing Strategy

The capturing strategy used in this study is depicted in Figure 5.1. One of the crucial parts of this strategy is the homogeneous phase interaction method for elimination of undesirable multiphase probe-analyte diffusion-limited interfacial interactions.[91] In particular, the target analyte is homogeneously mixed with anti-sense single strand DNA (ssDNA) conjugated antibodies in liquid phase before it is addressed to the substrate. This method can effectively eliminate the diffusion barrier for biochemical reagents on a solid surface and enhance the capturing efficiency of analyte by the antibody. The analyte-antibody-DNA complex is addressed to the substrate by DNA hybridization, which minimizes the

denaturation of antibody by avoiding antibody-surface interaction commonly encountered in conventional microarray detection methods.[91]

Another important part of the strategy is the preparation of substrates with high surface loading capacity. Densely packed Si nanowires were fabricated using metal-assisted chemical etching based techniques to increase the surface area of the substrates. The increased surface area leads to larger amount and higher density of probe sites for sense ssDNA to be attached to, which results in improved capturing results of anti-sense ssDNA and anti-sense ssDNA conjugated antibody with analyte.

By integrating these two parts, the capturing strategy in this study is capable of achieving high signal-to-noise ratio, which is critical for bioanalytic applications. The DNA-directed self-assembled analyte capturing strategy is versatile for both DNA and protein microarrays.

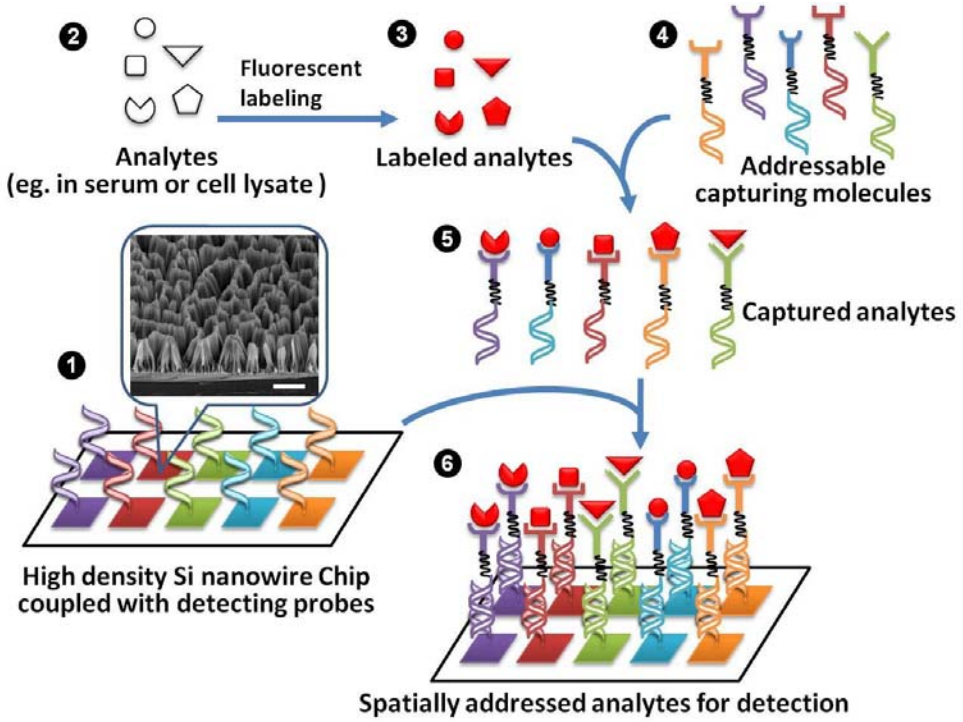

Figure 5.1: DNA directed analyte-specific capturing strategy on high density 3-D Si nanowire microarray. Homogeneous phase mixing method is employed to eliminate undesirable probe-analyte diffusion-limited interfacial interactions and minimize protein denaturation due to antibody-surface interaction. SEM of GLAD-MACE (Au) sample is used in step 1 to demonstrate the Si nanowire substrate. The scale bar in the SEM image is 10μm.

5.3 Experimental Conditions

Four types of Si substrates were used for the study of their bioanalytic performance in this Chapter, which are IL-MACE samples, GLAD-MACE (Au) samples, GLAD-MACE (Ag) samples and the control samples of flat Si wafers. GLAD-MACE sample is denoted as GLAD-MACE (Au) in Sections 5.3 & 5.4 of this chapter to differentiate from the samples prepared by Ag facilitated GLAD-

MACE process. In this chapter, RCA cleaned Si wafers (see Section 3.2) were used as starting material for all the samples. Optical lithography was used to pre-define Si microarray detection sites (2.5mm x 2.5mm) prior to Si nanowire fabrication. The fabrication processes of IL-MACE and GLAD-MACE (Au) Si nanowires on Si substrates have been elaborated in Sections 4.2 and 4.3, respectively. Similar to Au facilitated GLAD-MACE process, to prepare GLAD-MACE (Ag) sample, 200 nm Ag (reference thickness measured by crystal oscillator) was evaporated in glancing angle onto rotating Si wafer. Both GLAD-MACE (Au) and GLAD-MACE (Ag) samples were etched in MACE solution for 20 minutes, while IL-MACE samples were etched for 10 minutes. All of the Si nanowire samples and flat Si control samples were oxidized in O_2 at 900°C for 30 minutes to be chemically compatible with subsequent surface functionalization procedures. The detailed experimental procedures of surface loading density measurement, DNA and protein detections are summarized in Figure 5.2 and described in the following paragraphs of this section. All the bioanalytic results were obtained using fluorescent signals detected by GenePix 4000B Array Scanner (Molecular Devices, CA, USA) and the data analysis was carried out using GenePix Pro Version 4 software (Molecular Devices).

The surface loading capacities of the substrates were examined by directly conjugating dye molecules to the sample surface. The substrates were first aminated with 2% 3-aminopropyltriethoxysilane (APTES) in absolute ethanol for 12 hours (Step 1 of Figure 5.2) and then washed with ethanol for 3 times, and dried at 60°C for 24 hours. The direct couplings of Cy5-1-hydroxy-2-

nitrobenzene-4-sulfonic acid (Cy5-NHS) ester were carried out in 0.1 M MES buffer (pH 6.3) for 2 hours at 37°C in a humidity chamber (Step 2 of Figure 5.2). The substrates were then washed in 0.1% sodium dodecyl sulfate (SDS) at 60˚C, rinsed with double-distilled water and dried with absolute ethanol. The relative fluorescent unit (RFU) of the coupled Cy5-NHS on each substrate was quantified from nine replicate positions.

DNA detection process started with amination of oxidized Si nanowire substrates using APTES and was followed by carboxylation with succinic anhydride (Step 1 & 3 of Figure 5.2). The sense-strand of oligonucleotide with 5'-amino and 3'-Cy3 modifications was coupled to the carboxyl-terminated Si nanowire surface using 1-Ethyl-3-(3-dimethylaminopropyl)carbodiimide (EDC) and 1-hydroxy-2-nitrobenzene-4-sulfonic acid (HNSA) (Step 4 of Figure 5.2). The target anti-sense oligonucleotide was captured by hybridization to the immobilized sense strand oligonucleotide (Step 5 of Figure 5.2). The samples were then washed with 2% TX-100 in phosphate buffered saline (PBS) for 3 times and dried with enthanol.

To investigate the capturing of protein with anti-sense conjugated antibody, human serum was spiked with different concentrations of the analyte, rabbit IgG (Cy5 labeled, 10 pM to 100 nM). To conjugate antibody with anti-sense, goat Anti-Rabbit IgG(546) was desalted and dissolved in PBS. Sulfo-SMCC was added in to the solution at 1000:1 molar ratio to react with Anti-Rabbit IgG at room temperature for 30 minutes. The mixture was then spun at 16000 g for 30 minutes and purified with desalting column. Thiol-modified anti-

sense DNA was decapped in 10 mM DTT at room temperature for 30 minutes, and then dissolved in acetone with sodium acetate. The mixture was stored at 20°C for 30 minutes and then spun at 16000 g for 10 minutes. The supernatant solution was discarded and the precipitate was washed with 100% ethanol before it was resuspened in PBS. The activated Anti-Rabbit IgG was then mixed with decapped anti-sense DNA at a 1:10 molar ratio in PBS for 2 hours at 45°C for the conjugation to happen. The Si nanowire substrate was functionalized with corresponding sense strand. The performance of the Si chips were tested by homogeneously mixing of the Cy5-labeled rabbit IgG and anti-sense-conjugated goat Anti-Rabbit antibody (i.e. analyte-specific-reagent (ASR)),[92] and then followed by the addressing of this analyte-ASR complex on sense-functionalized GLAD-MACE (Au) and flat Si substrates through sense and anti-sense hybridization for 30 minutes at room temperature (Step 6 of Figure 5.2). The chip was then washed with 2% TX-100 in PBS and dried for scanning.

Interleukin-8 (IL-8) protein is one of the key biomarkers for sepsis detection. As the concentration of sepsis biomarkers are extremely low during early stage diagnosis, it is crucial to modify the standard protein capturing process and amplify the signal generated from limited target protein. First of all, the GLAD-MACE (Au) nanowire detection sites were functionalized with sense oligonucleotide and the substrate was blocked by 1% filtered Bovine serum albumin (BSA) in PBS to reduce non-specific reactions. The experimental procedures of homogeneous phase conjugation of IL-8 antibody (2μg/ml) with corresponding anti-sense oligonucleotide were similar to those introduced for

standard protein capture. The conjugated primary antibody was then mixed with human serum with different concentrations of spiked analyte (IL-8 protein without dye labeling) in 1 X PBS, 0.05% tween and 1% BSA and addressed on functionalized Si nanowire surface for 3 hours (Step 6 of Figure 5.2). After cleaning the samples in 2% tween PBS at 37 °C for 2 times (10 minutes each), in 0.05% PBST at room temperature for 5 minutes and rinsing in DI water, biotinylated secondary IL-8 antibody was free incubated in 0.05% PBST at room temperature for 1 hour on the sample surface (Step 7 of Figure 5.2). The samples were cleaned again in PBST (0.05%) three times for 5-10 minutes and rinsed in DI water. Finally, fluorescent labeling molecules of Streptavidin-Cy3 were diluted by 1% BSA, 0.05% PBST in a ratio of 1:125 and free incubated on the sample surface for 30 minutes (Step 8 of Figure 5.2). The samples were cleaned in 2% tween in PBS at room temperature for 2 times (10 minutes each) and in 0.05% PBST at room temperature 2 times (10 minutes each) and rinsed in DI water and spin dried for 5 minutes.

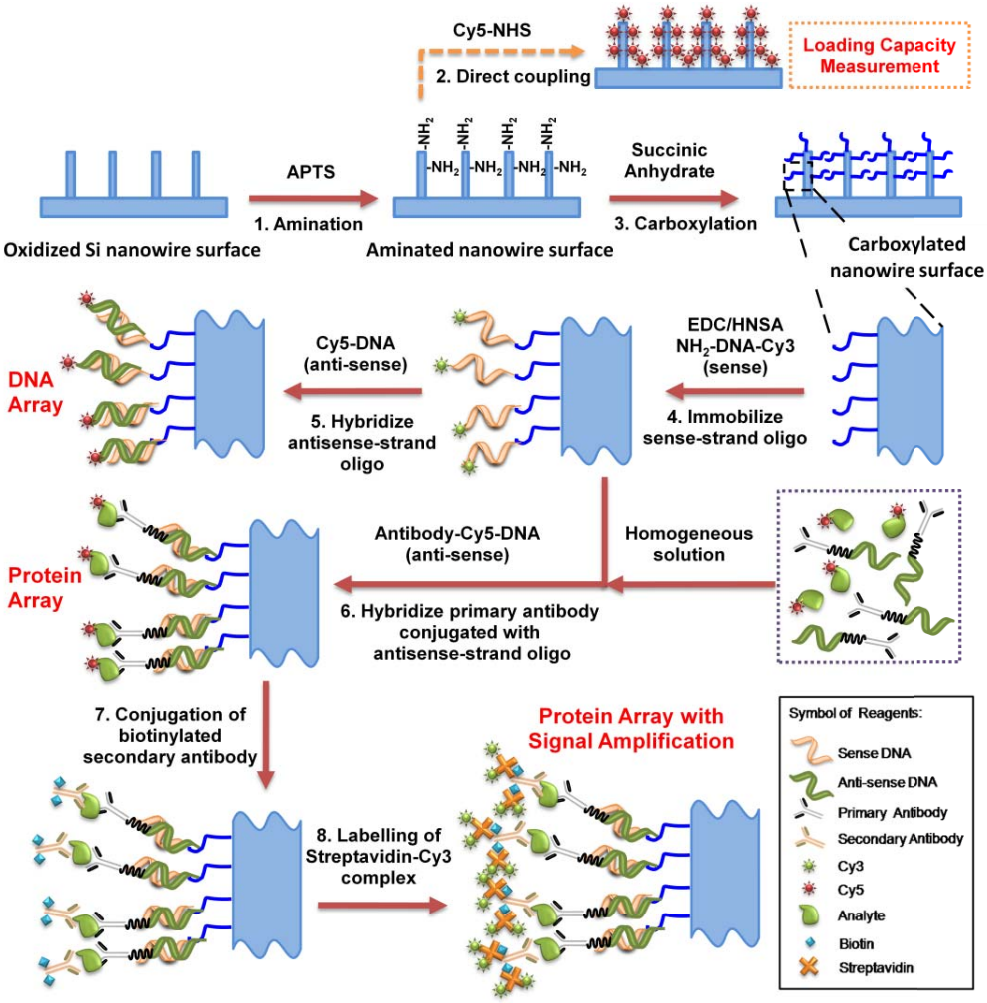

Figure 5.2: Process flow for loading capacity measurement, DNA detection, protein capture and enhanced protein capture with amplified signal for sepsis detection.

5.4 Surface Area and Loading Capacity Analysis

IL-MACE samples, GLAD-MACE (Au) samples, GLAD-MACE (Ag) samples and the control samples of flat Si wafers were tested and analyzed in this chapter to evaluate the surface loading capacity for best bioanalytic performance. Cy5-NHS direct coupling method is used to measure the loading capacities of

these samples and investigate the effect of increased surface area of the nanowire substrates as compared to a flat Si surface.

The structural characterization results of IL-MACE, GLAD-MACE samples have been discussed previously in Sections 4.2.1 and 4.3.1. The SEM and TEM results of IL-MACE, GLAD-MACE (Au) and GLAD-MACE (Ag) samples are summarized in Figures 5.3(a)-(f). It is obvious that the regularly arranged straight IL-MACE nanowires have larger diameter than the randomly arranged GLAD-MACE (Au) and GLAD-MACE (Ag) nanowires. The height of GLAD-MACE (Au) and GLAD-MACE (Ag) were measured to be both ~ 10 μm (images not shown in Figure 5.3).

An interesting finding from Figure 5.3(g) is that the Cy5-NHS coupling result of IL-MACE sample is ~40 fold higher than that of the flat Si control sample, while the surface area increase of IL-MACE samples to flat Si surface is only 2.5 times according to the dimensions of the IL-MACE nanowires (diameter ~400 nm, period ~ 1 μm, height ~2 μm). It is clear that the increase in apparent surface area of IL-MACE nanowires alone cannot account for the high signal response on IL-MACE samples. Similar result was also found on GLAD-MACE (Au) samples. Assuming all the GLAD-MACE (Au) nanowires are straight and isolated from each other, the apparent surface area increase of GLAD-MACE (Au) sample was calculated to be ~78.5 to 785 times to that of flat surface (considering the nanowire diameter as ~10 to 100 nm and the nanowire density in between 2.5×10^{7} mm^{-2} and 2.5×10^{9} mm^{-2}). However, as discussed in Section 4.3, when the MACE fabricated Si nanowires become longer and thinner, they are mechanically

weaker and become easier to bend and form nanowire clusters as shown in Figure 5.3(b). Therefore, the actual apparent surface area of the bent nanowires contributed to the loading capacity measurement should be much lower than the calculated value because a large portion of the calculated surface area was actually hindered after the cluster formation. With this consideration, the surface area increase due to apparent surface area of GLAD-MACE (Au) sample should be much lower than the increase of Cy5-NHS coupling efficiency on GLAD-MACE (Au) sample as compared to flat Si control sample (~500 fold). The surface area calculation and loading capacity analysis of both IL-MACE and GLAD-MACE (Au) samples indicate that there is at least another factor contributing to the high loading capacity of the MACE fabricated Si nanowires as compared to flat Si surface.

As explained in Chapter 4, electronic hole injections during metal-assisted chemical etching may induce Si surface damage and form porous Si surface.[32],[33],[88] It is also revealed by high resolution SEM and TEM images in Figures 5.3(d) & (e) that the surface of IL-MACE and GLAD-MACE (Au) nanowires was roughened during their formation. The surface porosity of MACE fabricated Si nanowires was further confirmed by BET and thermoporometry results as discussed in Chapter 4. As shown in Table 4.1, thermoporometry analysis has provided quantitative measurement results of the pore diameter, total pore surface area and total pore volume of the IL-MACE and GLAD-MACE (Au) samples. Both total pore surface area and total pore volume of GLAD-MACE (Au) samples are an order of magnitude higher than those of IL-MACE samples, which

is in good agreement with the loading capacity comparison. Hence, the mesoporous surface of metal-assisted chemically etched Si nanowires could have effectively increased the surface area for chemical reactions and resulted in high surface loading capacity.

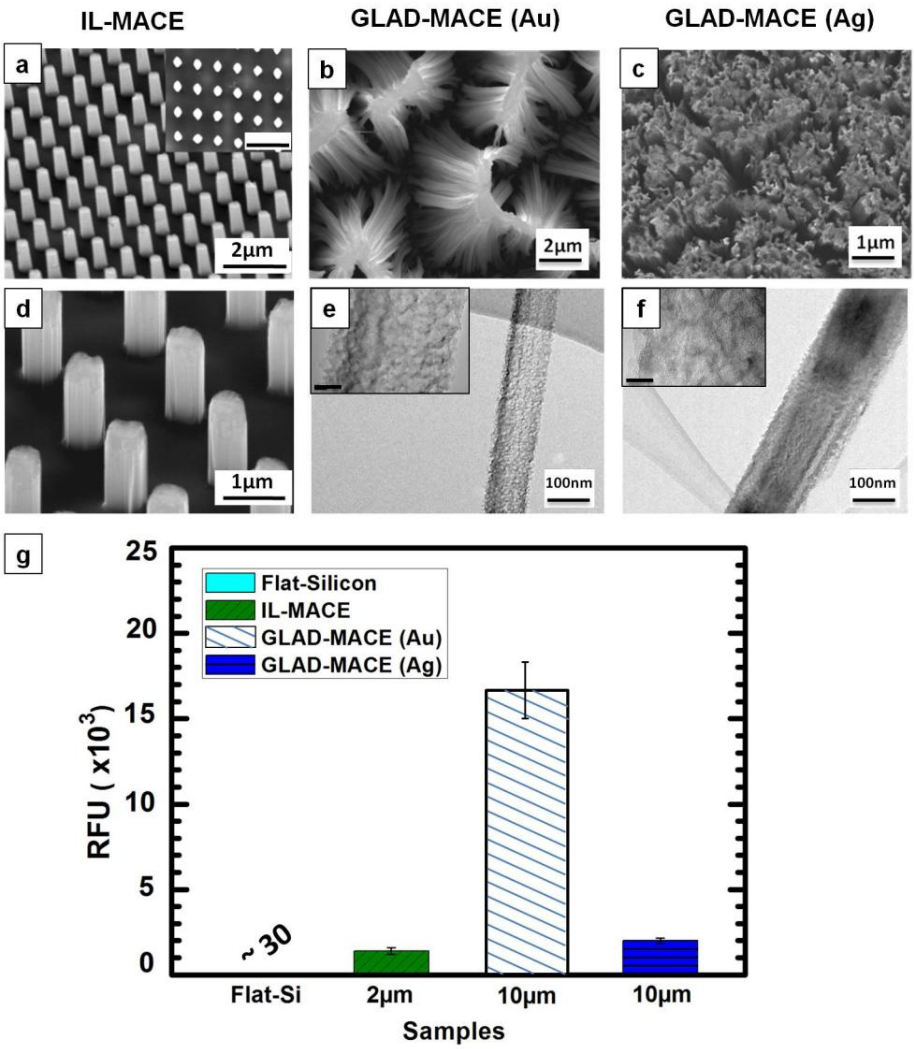

Figure 5.3: Morphology of Si nanowires and the loading capacity test results. (a) and (d) are tilted view SEM images of Si nanowires fabricated by IL-MACE method. The inset in (a) is the top view SEM with scale bar of 2μm. (b) and (c) are top view SEM images of Si nanowires obtained from the GLAD-MACE method with Au and Ag catalysts, respectively. (e) and (f) are TEM images of GLAD-MACE nanowires obtained with Au and Ag catalysts, respectively. The insets in (e) and (f) are the corresponding HRTEM images with scale bars of 10nm. The density of reactive amine group on these substrates are shown in (g) where the relative fluorescent unit (RFU) readings of directly coupled Cy5 (1:100).

A good method to examine the effect of surface porosity on surface loading capacity is to compare the results of GLAD-MACE (Au) samples with those of GLAD-MACE (Ag) samples. GLAD-MACE (Ag) nanowires were less porous and, as a result, less clumped than GLAD-MACE (Au) nanowires (see Figure 5.3). While the diameters and heights of GLAD-MACE (Au) and GLAD-MACE (Ag) nanowires are very similar, the straighter GLAD-MACE (Ag) sample should have larger apparent surface area exposed to chemical reagents. This is supported by the image analysis using software package ImageJ, which estimates the values of perimeter per unit area of these clumped nanowires to provide a measure of the "exposed" surfaces for loading capacity test. It can be seen from Table 5.1 that the apparent surface area of GLAD-MACE (Au) is only ~ 27% of that of GLAD-MACE (Ag) samples. However, the loading capacity of GLAD-MACE (Au) is 8 times higher than GLAD-MACE (Ag) as shown in Figure 5.3(g). From this comparison, we can conclude that the surface porosity is a dominating factor for determining the surface loading capacity of a nanowire substrate.

Table 5.1: The values of perimeter per unit area of GLAD-MACE samples obtained with Au and Ag catalysts with different drying processes

Sample			
Catalyst	Drying process	Perimeter per unit area/μm^{-1}	
Au	De-ionized water	1.82	
Au	De-ionized water with N_2 flow	2.09	**----GLAD-MACE (Au)**
Au	Methanol	1.92	
Ag	De-ionized water with N_2 flow	7.66	**----GLAD-MACE (Ag)**

The effect of the nanowire clumping to the surface loading capacity was further studied by preparing a set of GLAD-MACE (Au) substrates using different drying methods (i.e. dried in DI water, methanol and DI water by dried by N_2 gun) right after the etching process. The experiment was designed with our knowledge that the porous nanowires tend to stick together due to capillary force and short-ranged van der Waals force when the sample is left to dry after etching, and the degree of clumping of the Au-etched nanowires can be modulated by drying the nanowires in different medium such as de-ionized water, 2-propanol and methanol. The detailed mechanism of Si nanowire cluster formation will be further elaborated in Chapter 6. It can be seen from Table 5.1 that the magnitudes of the perimeter per unit area obtained from samples dried with methanol and N_2 flow are higher than that dried in DI water. The Cy5-NHS coupling efficiency of the purely DI water dried, DI water dried in N_2 flow, and methanol dried samples were 6.67×10^3, 1.36×10^4 and 9.73×10^3, respectively. Bearing in mind that all the nanowires here possessed almost the same porosity (i.e., prepared using the same GLAD and MACE conditions), it can be concluded that sample with larger

exposed surface (i.e., higher value of perimeter per unit area) has higher Cy5-NHS coupling efficiency. Note that, regardless of the drying methods, the loading capacities of the GLAD-MACE (Au) samples are all much larger than the result of GLAD-MACE (Ag) samples, even though GLAD-MACE (Ag) samples have much higher value of perimeter per unit area (see Table 5.1) These results confirm that the clumping of nanowires is a secondary factor for surface loading capacity of metal-assisted chemically etched Si nanowires.

5.5 DNA Capture

The GLAD-MACE (Au) substrates have demonstrated the highest loading capacity among all of our samples in Section 5.4. As a result, it was used as the platform for the rest of the bioanalytic experiments in this Chapter and is denoted as GLAD-MACE substrate in the following sections.

The DNA capture process started with immobilization of single-strand sense DNA oligonucleotides (ssDNA) onto the substrate (base platform) to allow sequence-specific capturing of either the target DNA or complementary ssDNA-conjugated probes. In order to assess the improvement in the performance of the GLAD-MACE platform, we also simultaneously compared the ssDNA coupling efficiency on GLAD-MACE substrate with those of flat Si substrates (Step 4 of Figure 5.2). To this end, both surfaces were aminated (Step 1 of Figure 5.2) and further functionalized with succinic anhydride (Step 3 of Figure 5.2) to enable the covalent coupling of an amine-terminated Cy3-modified ssDNA (NH2-Oligo-Cy3).[93] The GLAD-MACE surface showed dose-dependent coupling of the

NH2-Oligo-Cy3 (6.4 nM to 20 μM), while a control reaction without cross-linker EDC confirmed that the coupling was not due to the non-specific adsorption of the oligonucleotide onto the GLAD-MACE substrate. The flat Si surface, in contrast, had significantly lower coupling efficiency under all conditions. In particular, the GLAD-MACE substrate showed a 250-fold increase in signal intensity as compared to that of flat Si substrate (see Figure 5.4(a)). This is a demonstration of increased density of detection sites.

To detect target anti-sense DNA, the substrates were first functionalized with increasing concentrations of NH2-Oligo-Cy3 at concentrations (6.4 nM to 20 μM). For negative controls, EDC was not added during functionalization. A complementary strand of Cy5 modified ssDNA (anti-sense oligonucleotide, 20 μM) was then hybridized (Figure 5.4(b)). Washing steps were carried out to minimize nonspecific adhesion to GLAD-MACE surface after funtionalization and hybridization. The result also gives a ~250 fold increase in signal response, indicating that the GLAD-MACE substrates provide a more superior platform than flat Si substrates for applications in DNA microarray.

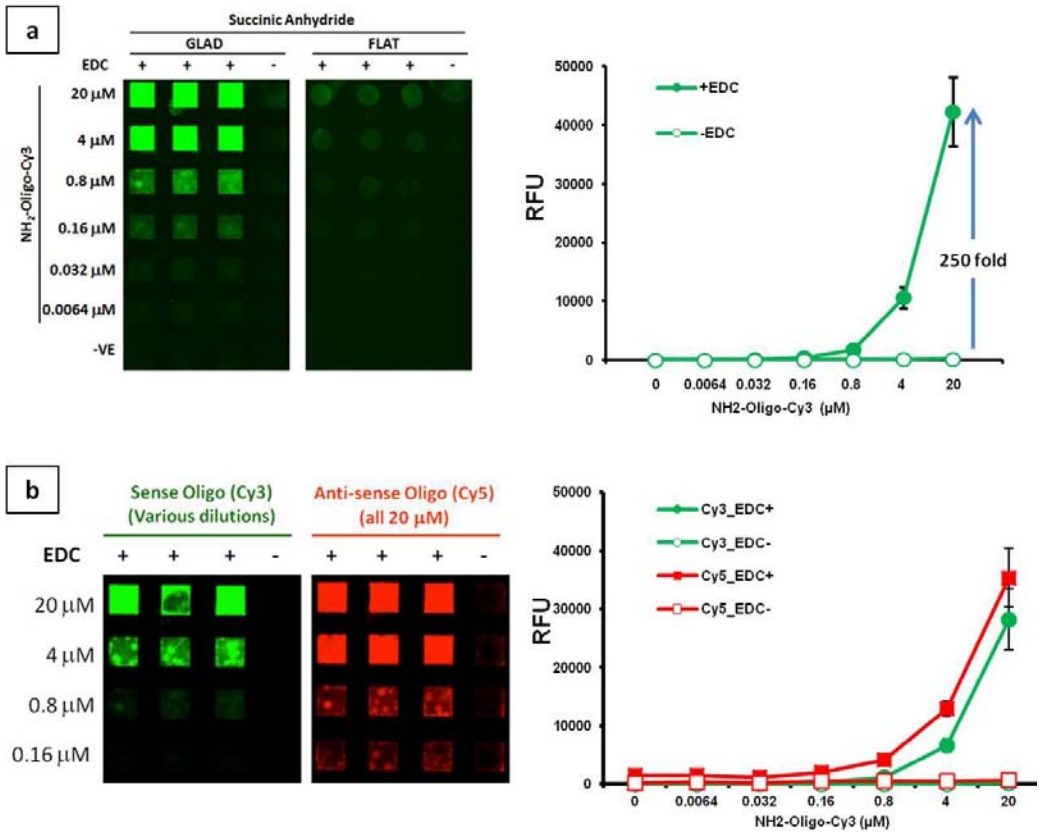

Figure 5.4: (a) Comparison of the coupling efficiency of ssDNA on GLAD-MACE substrates after free incubation of various concentrations of Cy3 labeled ssDNA oligos. (b) Comparison of the coupling efficiencies of sense and anti-sense ssDNA on GLAD-MACE microarray chip; the figure shows the florescent intensity of Cy3 coupled sense strand (green) and Cy5 coupled target strand on GLAD-MACE substrates at various concentrations of Cy3 labeled ssDNA oligos and Cy5 ssDNA anti-sense oligo at 20 µM.

5.6 Protein Capture

The capability of using GLAD-MACE Si nanowire platform to capture target protein was investigated by detection of analytes from complex biological fluids. Human serum was spiked with different concentrations of the analyte,

rabbit IgG (Cy5 labeled, 10 pM to 100 nM). The performance of the GLAD-MACE substrates was tested for homogeneous phase capturing of the Cy5-labeled rabbit IgG using ssDNA-conjugated goat anti-rabbit antibody. A dose-dependent detection of the analyte was observed in the case of both GLAD-MACE and flat Si substrates (Figure 5.5(a)). The negative control reaction on substrate without functionalized ssDNA confirmed that the hybridization was not due to non-specific adsorption of the analyte or ASR onto the GLAD-MACE substrate. Normalized RFU (analyte/ASR) showed that the GLAD-MACE substrate captured significantly more analyte than the flat Si substrate (up to 250 fold, see Figure 5.5(b)). This was in congruence with the previous observation on the differences in loading capacities of ssDNA on the two substrates. In addition, the GLAD-MACE substrate exhibited a higher assay dynamic range over the flat substrate. These results indicated that the GLAD-MACE array indeed offered a higher loading capacity and an improved SNR and can be adapted for the detection and quantification of various types of biomolecules in complex biological samples.

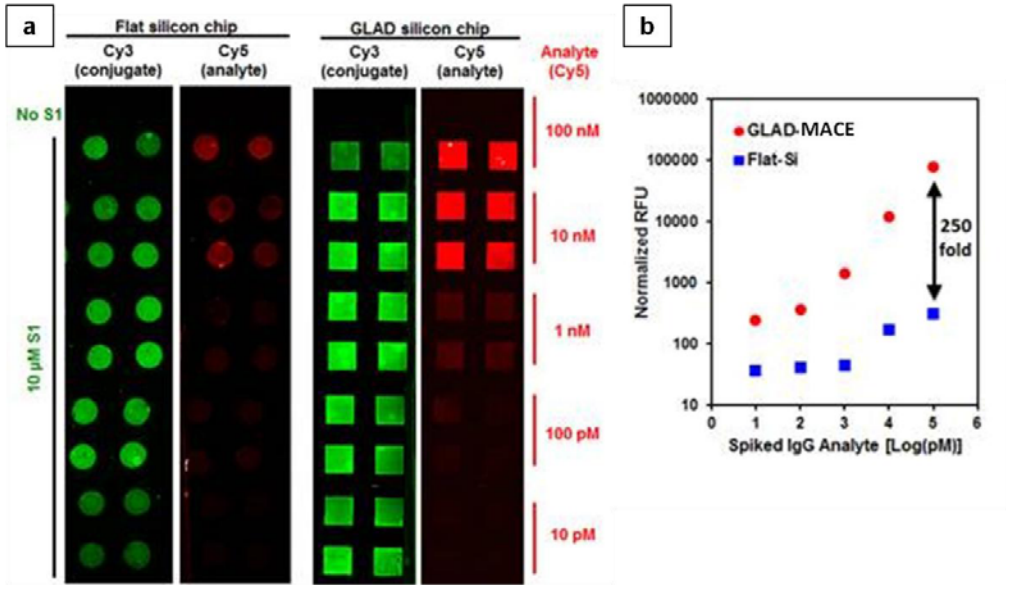

Figure 5.5: Detection of standard IgG protein analyte in human serum using GLAD-MACE substrate. Human serum was spiked with different concentrations of the analyte of interest (Cy5 labeled rabbit IgG, 10 pM to 100 nM). (a) is the representative fluorescent image of flat Si and GLAD-MACE substrates with captured analytes. (b) is normalized RFU (analyte/ASR, Cy5/Cy3) result.

5.7 Sepsis Capture

The superior performance of GLAD-MACE platform as standard protein microarray has demonstrated its potential in human disease detection. The high loading capacity of GLAD-MACE nanowire substrate and the positive experimental results of fast and sensitive protein capture in human blood serum make it a promising protein microarray for early stage disease diagnosis, such as sepsis diagnosis. Sepsis is a fatal disease caused by severe infection and immune system disruption. Due to the complicated symptoms and high mortality rate in short period of time, prompt diagnosis of sepsis through patient blood is critical

for effective early stage therapy. IL-8 protein, a proven important blood borne biomarker for early sepsis diagnosis,[94],[95] was identified as target protein in this preliminary study. As the concentration of sepsis biomarkers in human blood serum are extremely low during the early stage, standard protein capturing was modified to amplify the signal from the limited target protein. Prior to the sepsis capture process, the detection sites were functionalized with ssDNA specially designed for IL-8 protein and the rest of the area was passivated with BSA to reduce non-specific interaction. The primary IL-8 antibody was then conjugated with complementary anti-sense ssDNA and homogeneously mixed with different concentrations of IL-8 protein spiked in human serum. The signal amplification was achieved by attaching biotinylated second antibody to the analyte and coupling with Streptavidin-Cy3 complex as illustrated in Step 7 & 8 of Figure 5.2. The preliminary IL-8 protein detection result in Figure 5.6 indicates a lower detection limit of ~ 8 ng/ml (equivalent to 1 nM). The background signal in Figure 5.6 is generated from non-specific reactions of DNA conjugated analyte on carboxyl-terminated GLAD-MACE Si nanowire surface without functionalized ssDNA.

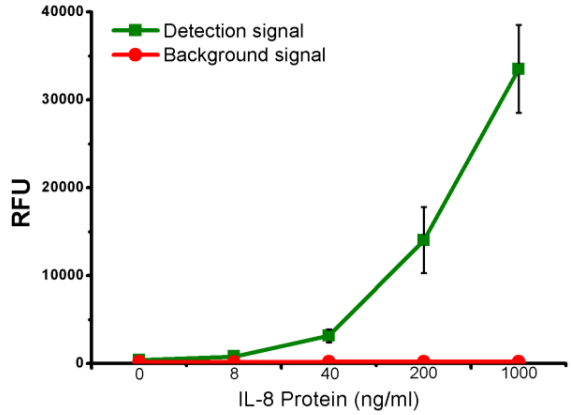

Figure 5.6: Normalized RFU results of detection of IL-8 protein analyte in human serum using GLAD-MACE substrate. Human serum was spiked with different concentrations of IL-8 protein (0 – 1000 ng/ml). The background signal is the non-specific coupling efficiency on carboxyl-terminated GLAD-MACE Si nanowire surface without functionalized ssDNA.

5.8 Summary

In this chapter, we have demonstrated the performance of Si nanowire substrates for the DNA and protein microarray applications. The novel homogeneous phase DNA-directed protein capturing strategy on 3D Si nanowire substrate was presented. The surface loading capacities of different Si nanowire substrates were compared. The effects of apparent surface area, surface porosity and degree of clumping of nanowires were studied for understanding of the causes of high loading density of MACE fabricated nanowire substrates. GLAD-MACE (Au) substrate with highest loading capacity was selected as the platform for DNA and protein capture. Eventually, the results of DNA capture, standard protein capture and IL-8 sepsis protein capture were successfully demonstrated on GLAD-MACE substrates.

Chapter 6 GLAD-MACE Silicon Nanowires for Lotus-like and Petal-like Biomimetic Surfaces

6.1 Introduction

Nature inspires human with many biological designs and functions.[51]-[63] The surfaces of lotus leave and rose petals have presented very interesting surface properties, both exhibiting high superhydrophobicity (very large static water contact angle) but very different surface adhesion (contact angle hysteresis).[59],[60],[96]-[99] Recently, artificially fabricated lotus-like and petal-like surfaces have demonstrated their potential in wide scope of applications, including self-cleaning and surface wetting manipulation.[52]-[54] In this chapter, lotus effect and petal effect will be mimicked in large surface area using randomly located GLAD-MACE Si nanowires. To investigate the surface wettability, the classic Wenzel model and Cassie-Baxter model are the most accepted theories.[100],[101] Wenzel model predicted that surface roughness can greatly enhance the surface hydrophilicity or hydrophobicity depending on the intrinsic surface property.[100] Although flat bare Si surface is intrinsically hydrophilic, the surface wettability can be altered by coating a uniform thin layer of hydrophobic organosilane on the sample surface. With high density Si nanowires embedded on the Si substrates, very high static water contact angle can be obtained on the surfaces of GLAD-MACE samples. The surface adhesion of the GLAD-MACE samples will be modulated by two methods in this study, in particular, varied GLAD duration and different drying methods. The versatility of

these methods will be demonstrated by integrating the lotus-like and petal-like surfaces on a single substrate.

6.2 Experimental Conditions

The fabrication method for GLAD-MACE Si nanowires has been presented in Section 4.3. Si wafers were cleaned and dipped in diluted HF before GLAD process. The GLAD duration was modulated to deposit Au of different reference thickness (from 60 nm to 200 nm) to form metal particles with different size distributions. The duration of the subsequent MACE process was fixed at 20 minutes. The etched samples were either dried with N_2 gun or immersed in pure DI water, 2-propanol or methanol to be dried in ambient environment. The Au on the Si surface was then removed using a commercial Au etchant. Next, the samples were etched in diluted HF to remove any native oxide before silanization. The silanization process was done by placing the samples together with 6 μl of tridecafluoro-(1, 1, 2, 2 tetrahydrooctyl)trichlorosilane [$CF_3(CF_2)_5(CH_2)_2SiCl_3$] in a desiccator for 12 hours under house vacuum (mTorr) for uniform coating. The surface contact angle of bare Si surface could be increased from ~76.6° to ~119.1° after the silanization process due to the low surface energy (13.22 mJm^{-2}) of the organosilane.[102] VCA Optima contact angle measurement goniometer was used to dispense DI water droplets of 4 - 6 μl on sample surface for all the contact angle measurements in this chapter. All the contact angle measurements in this study were carried out on silanzied Si samples and the results were obtained with an average of 5 measurements.

6.3 Fabrication of Lotus-like and Petal-like Surfaces by Different GLAD Durations

The experimental configuration and characterization results of GLAD process have been discussed previously in Sections 3.9 & 4.3. In this section, the duration of GLAD was varied to control the surface morphology of Au nanoparticles deposited onto Si surface. Figure 6.1(a) is the GLAD sample with shorter GLAD duration (with reference thickness of 60 nm) while Figure 6.1(b) corresponds to the GLAD process with longer duration (with reference thickness of 200 nm). A longer duration of GLAD evaporation generally led to larger Au nanoparticles. However, it is important to point out that a longer duration does not imply that all the nanoparticles would be larger. The histogram of Au nanoparticle size distribution in Figure 6.1(c) shows that a wide size distribution of Au nanoparticle (with diameter from 10 nm to 100 nm) could be observed for the samples fabricated with longer GLAD duration. In comparison, most of the Au nanoparticles on the sample deposited with shorter GLAD duration were less than 40 nm in diameter. The difference of Au particle size distributions was caused by atomic shadowing effect during the GLAD process. In the initial stage of GLAD process, the evaporated Au atoms (adatoms) condensed on Si surface and coalesced to form individual islands (nuclei) that geometrically shadowed the substrate due to the oblique arrival angle (of 87º) and the low surface diffusivity of the adatoms.[103] As a result, atomic shadowing effect prevented the formation of a continuous thin film. As the deposition process continued, the nuclei captured more adatoms and grew in the direction of the vapor source. By

rotating the substrate, the net direction of nuclei growth was resolved vertically.[103] Due to the competitive nature of the atomic shadowing process, as soon as a nucleus outgrew its neighboring nuclei, all further growth of the nuclei in its vicinity would be ceased. For shorter-duration GLAD process, most of the nuclei were grown at a similar rate, which resulted in nanoparticles of similar sizes (diameter less than 40 nm). As the GLAD process continued for a longer time, more and more nuclei were restricted from growing further due to atomic shadowing caused by larger nuclei, and these larger nuclei captured more adatoms and further increased in size over time, leading to a wider size distribution (with diameter 10 to 100 nm). The Au particles with tunable size distribution can be used to create GLAD-MACE Si nanowire surface with very different morphology.

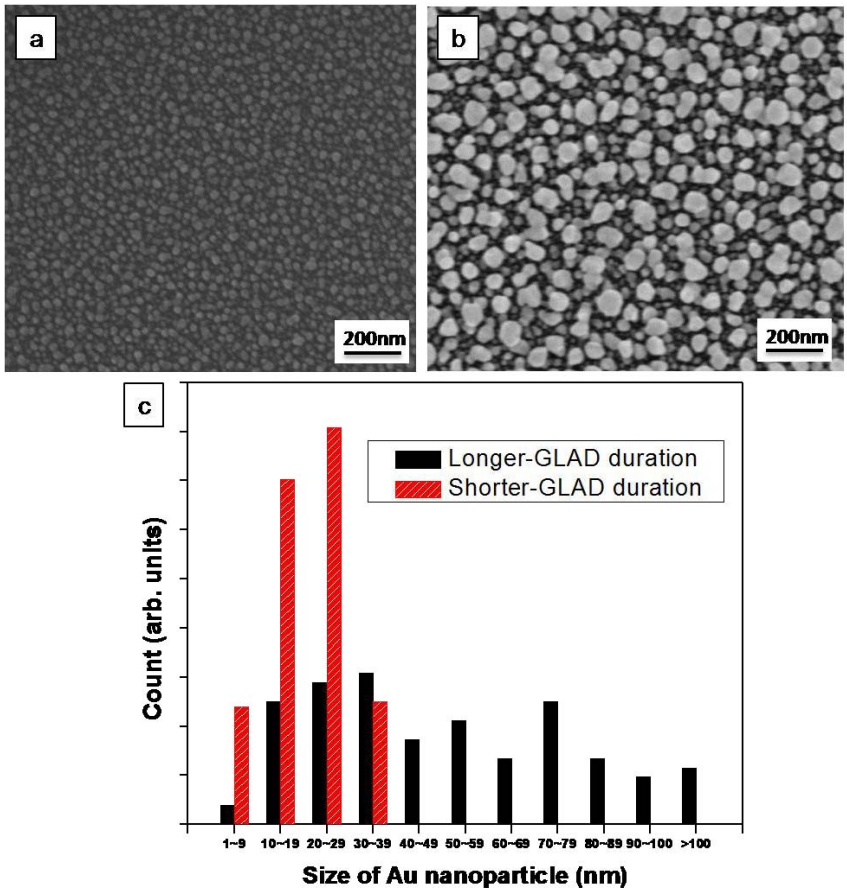

Figure 6.1: Analysis of Au nanoparticles on Si surface deposited by different GLAD durations. Top-view SEM images of Au nanoparticles deposited with (a) shorter GLAD process (with reference thickness of 60 nm) and (b) longer GLAD process (with reference thickness of 200 nm) on Si surfaces. (c) Histogram of the size distributions of Au nanoparticles deposited using shorter and longer GLAD durations. The nanoparticle sizes in the histogram were determined by statistical measurements in the SEM images similar to (a) and (b).

The SEM images of GLAD-MACE Si nanowires fabricated with shorter and longer GLAD durations are shown in Figures 6.2(a) & (b), respectively. The GLAD Si nanowires fabricated with shorter GLAD duration were relatively

straighter as compared to the longer GLAD duration samples. It should be noted that the diameter and height of these two types of nanowires were similar as shown in Figure 6.2. The difference in the degree of clumping of the shorter-duration and longer-duration GLAD-MACE Si nanowires could be explained by the different porosity indicated in the TEM images in Figures 6.2(c) & (d). In particular, Figure 6.2(c) shows a Si core surrounded by porous Si surface while a completely mesoporous Si nanowire could be observed in Figure 6.2(d). Magoariec and Danescu have reported that a higher porosity of Si leads to lower Young's modulus and poorer mechanical strength.[84] Therefore, the difference in porosity of nanowires in Figures 6.2(c) & (d) gave rise to nanowires of different rigidity. The Si nanowires fabricated with longer GLAD duration had smaller elastic force to overcome the capillary force during the surface drying process after MACE.[82] The different surface morphology of the GLAD-MACE Si nanowire samples was used to change the surface adhesion.

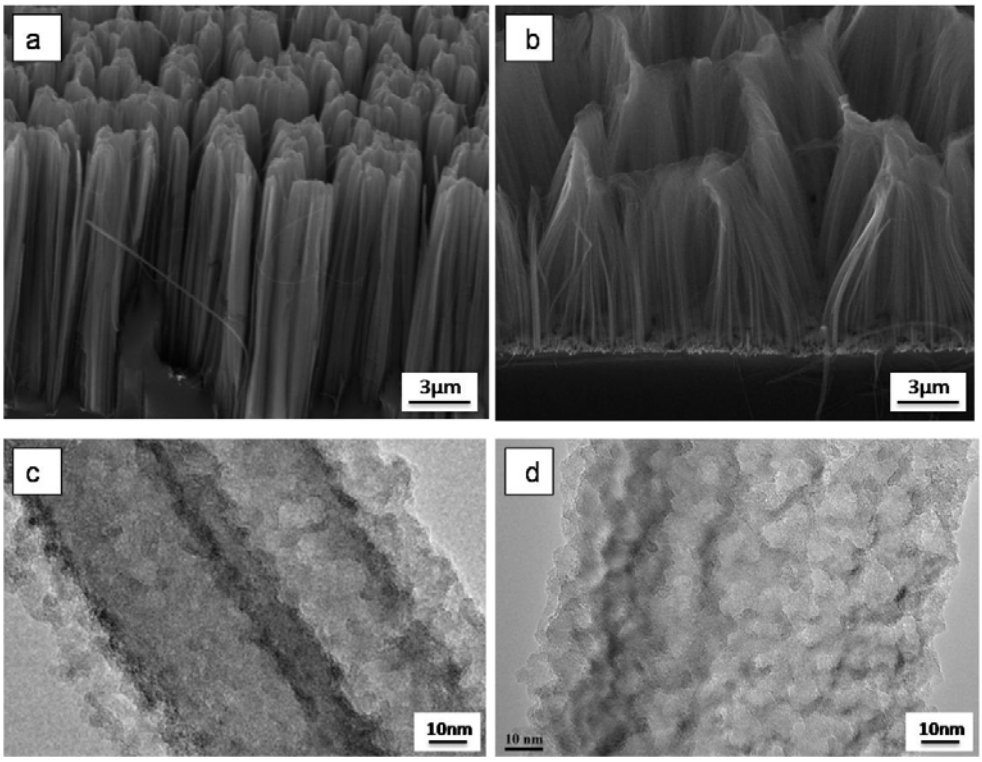

Figure 6.2: Structural characterization results of GLAD-MACE nanowires fabricated with different GLAD durations. SEM images of (a) shorter-duration and (b) longer-duration GLAD samples. TEM images of (c) shorter-duration and (d) longer-duration GLAD samples.

The static water contact angle measurement results on silanized GLAD-MACE Si nanowire surfaces are shown in Figure 6.3. The longer-duration GLAD sample exhibited a contact angle of 156° ± 0.5° (see Figure 6.3(a)) with negligible contact angle hysteresis. Contact angle hysteresis was measured by taking the difference between advancing contact angle and receding contact angle. Advancing contact angle was measured as the contact angle just before the contact line advances as water was dispensed on the surface. Similarly, the receding contact angle was measured as the contact angle just before the contact

line recedes as water was withdrawn from the surface. The surface of longer-duration GLAD samples was very effective at repelling water, that at least a 6 μl drop of water was needed for the contact angle measurements because droplets of smaller volumes would remain on the syringe. In addition, the droplets dispensed on the sample surface could easily roll off the surface due to any initial momentum, slight tilt or little vibration. These phenomenon indicate that the low-adhesion superhydrophobic surface properties of lotus leave were successfully mimicked on longer-duration GLAD samples. In contrast, although the shorter-duration GLAD samples had a large contact angle of 150° ± 2° (see Figure 6.3(b)), a high contact angle hysteresis of ~27° was obtained on the samples. These samples mimicked the rose petals with high superhydrophobicity and surface adhesion. The high surface adhesion enabled the sample surface to pin a droplet of water, even with a tilting of the surface upside down (i.e. at a tilting angle of 180°) as shown in Figure 6.3(c). The surface was able to hold liquid droplets of up to 6.5 μl, which corresponds to an estimated adhesion force of ~64 μN in order to keep the drop attached to the surface. This outperformed many other high-adhesion superhydrophobic surfaces reported in the literature. [59],[98],[104]

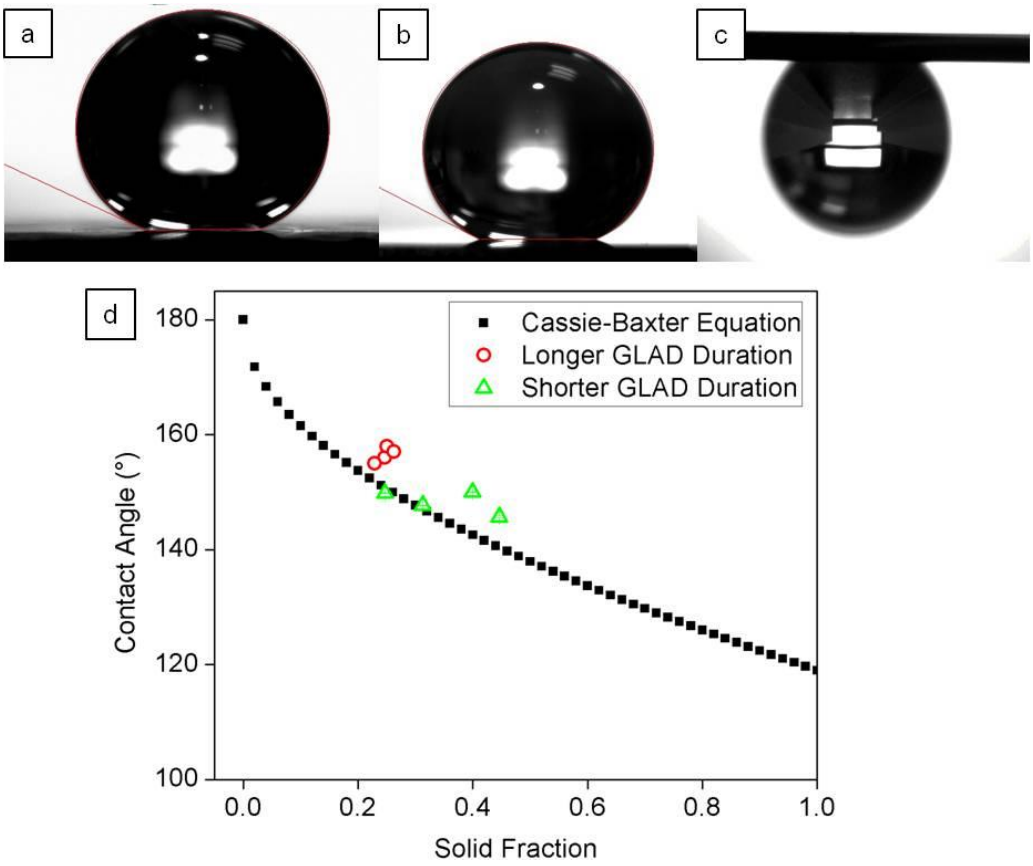

Figure 6.3: Surface wetting characteristics of silanized GLAD-MACE Si nanowire samples with longer and shorter GLAD duration. Static surface contact angle of GLAD-MACE samples with (a) longer GLAD duration and (b) shorter GLAD duration. The high adhesion of the surface of the sample with shorter GLAD duration was demonstrated using a 4µl droplet in (c). (d) is the fitting of surface water contact angles obtained from images similar to (a) and (b) to Cassie-Baxter equation.

The static water contact angles can be explained by the classic Cassie-Baxter model, which assumes that the water droplet rests on a 'pin-cushion' of nanowires and does not penetrate into the nanostructures (i.e. a heterogeneous flat interface comprise of solid surface and air pockets).[101] The Cassie-Baxter equation was given as

$$\cos\theta^* = -1 + f(\cos\theta_0 + 1) \tag{6.1}$$

where f is the fraction of the wetted surface comprised by the solid, θ_0 is the Young's angle on a smooth homogeneous surface of the solid material, θ^* is the contact angle on the rough surface.[105] To fit the measured contact angle to Cassie-Baxter equation, solid fraction was estimated from the top view SEM images of the GLAD-MACE Si nanowire surfaces. The SEM images were first converted from the original grayscale into black and white images by applying a suitable threshold using the MATLAB^{TM} image processing toolbox (MathWorks Inc.). The solid fraction f was calculated as the ratio of white pixels (indicating the tips of the nanowires) to the total number of pixels constituting the image. Figure 6.3 shows that the measured contact angles at the corresponding estimated solid fractions followed the predictions of the Cassie-Baxter equation quite closely. The longer-duration GLAD samples generally had lower solid fraction as compared to the shorter-duration GLAD samples with straighter nanowires.

To understand the surface adhesion of the GLAD-MACE samples, the surface morphology of the GLAD-MACE Si nanowires with different GLAD duration was analyzed. The longer-duration GLAD samples had relatively larger and interconnected nanowire clusters, with air gaps between adjacent clumped nanowire bundles in the 10 μm size range. The shorter-duration GLAD samples, on the other hand, had much more compact structures, with isolated air pockets of sub-micron width between adjacent bundles of nanowires. The high adhesion behavior of the shorter-duration GLAD samples cannot be explained by the impregnated Wenzel state (i.e. air gaps between nanowires replaced by water) as

the open interconnected structure of the longer-duration GLAD samples were more likely to have impregnation and therefore higher surface adhesion.[98] The high surface adhesion of the shorter-duration GLAD samples in the Cassie-Baxter state may be explained by a combination of attractive van der Waals forces, which is similar to the mechanism governing the remarkable adhesive properties of Gecko feet and capillary adhesion. Following the approach of Autumn et. al., the van der Waals force (F_V) between a straighter silanized nanowire bundle and a sitting water droplet may be estimated by approximating the tip of a bundle to be a sphere of fluorinated silane of radius R in contact with a plane water surface.[106] Assuming a radius R of 50 nm, a cut-off distance d of 0.165 nm,[107] and estimating a silane-water Hamaker constant A as $3.7\text{x}10^{-20}$ J ($A \approx (A_{sil}\, A_{water})^{1/2}$, where $A_{sil} = 3.8\text{x}10^{-20}$ J and $A_{water} = 3.7\text{x}10^{-20}$ J are the Hamaker constants of silane and water respectively,[108] we have $F_V = AR/6d^2 \approx 10$ nN. A 4 μL water drop supported upside-down exerts a force of F_G of 40 μN. Therefore, through this rough approximation, we estimate that a collective attractive force of ~5000 nanowires can indeed balance the weight of the drop. Another possible force to contribute to the high adhesion of the shorter-duration GLAD sample is the capillary adhesion. Air trapped in isolated pockets on this surface can exert a suction pressure P_S on a drop during its withdrawal from the surface. Assuming a typical pocket height h and radius r of 10 μm and 2 μm, respectively, one can estimate a suction pressure $P_S \approx P_0 \frac{r^2 h}{r^2 h + 2/3 r^3} - 2\frac{\sigma}{r} = 0.16 P_0$ per pocket, where P_0 is atmospheric pressure and $\sigma = 0.072$ Nm^{-1} is the air-water interfacial tension. This leads to a force per pocket of $F_C \sim 200$ nN; the collective effect of multiple

trapped air pockets could therefore contribute to the observed adhesion behavior. The results presented in this section are in good agreement with the report of Lai et al., who reported a similar high-adhesion behavior in nanopore and nanotube arrays and low adhesion in more open and porous nanostructures.[109]

6.4 Fabrication of Lotus-like and Petal-like Surfaces by Different Drying Methods

Another method to modulate the surface wettability of GLAD-MACE Si nanowire samples is using different drying methods during capillary nanocohesion process. To study the effect of different liquid medium used during surface drying, the samples were fabricated in a single batch with fixed GLAD duration (with reference thickness of 200 nm) and MACE conditions. Right after the etching process, the samples were rinsed in DI water and quickly transferred to DI water, 2-propanol or methanol solutions and left to dry in ambient environment. The surface morphologies of GLAD-MACE Si nanowire samples dried in different liquid medium are shown in the top view and tilted view SEM images in Figures 6.4(a)-(c) and the insets. It was found that different drying medium caused significantly different nanowire cluster morphologies. As the very thin GLAD-MACE Si nanowires were randomly distributed and clumped into nano-clusters, it was difficult to quantify the actual number of nanowires per cluster according to the SEM results. In general, the water-dried samples had the smallest clusters (~1 μm sized clusters at tips) while the methanol-dried samples consisted of largest clusters of nanowires (~5 μm sized clusters at tips).

Similar to the method introduced in Section 6.3, the solid fractions of the samples shown in Figures 6.4(a)-(c) were estimated from digitally analyzed SEM images and summarized in the histogram in Figure 6.4(d). The results in Figure 6.4 revealed the relation between the average cluster size and the solid fraction. The smaller nanowire clusters of the water-dried sample led to the smallest solid fraction of 0.17, the 2-propanol-dried sample resulted in a solid fraction of 0.21 while the methanol-dried sample, consisting of the largest nanowire clusters, resulted in the largest solid fraction of 0.29.

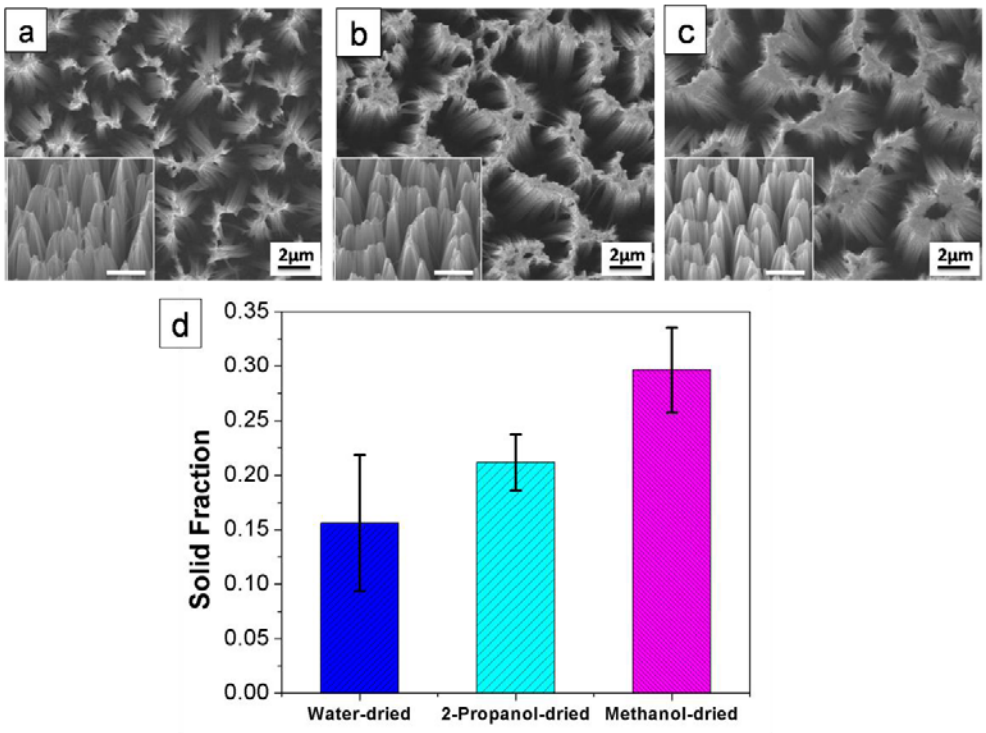

Figure 6.4: SEM images of GLAD-MACE nanowires dried in (a) water, (b) 2-propanol and (c) methanol. Insets are tilted SEM images of nanowire arrays with scale bar of 5 µm. (d) is the solid fraction of the samples similar to those shown in (a) – (c).

The nanowire cluster size observed on the samples were studied using force balance during the surface drying process in different liquid. In order for nanowires to clump together and remain so, the capillary forces exerted on the nanowires at the meniscus need to be larger than the counter balanced elastic force to sufficiently bend the nanowires to cause cohesion.[81]-[83],[110]-[112] Furthermore, to maintain the nanowires clusters after the drying process, the short-ranged van der Waals forces between the nanowires need to be larger than the elastic forces. The size of a nanowire cluster depends on the balance of the

three forces at work. Kang et al. modeled the net cluster size, N (average number of nanowires per cluster), based on static energy minimization as

$$N \sim \frac{E_C}{E_E} \sim \frac{\gamma_{la} h^3 \cos^2\theta_0}{D^2(p-D)^2 E} \tag{6.2}$$

where E_C is the capillary interaction energy, E_E is the elastic energy term, γ_{la} is the surface tension of the liquid, h is the height of the nanowires, θ_0 is Young's angle (contact angle of liquid on flat homogeneous solid surface), p is the distance between nanowires and D is the diameter of the nanowire.[81]

The capillary force exerted between two nanowires by surface tension is expressed by the surface tension, γ_{la}, and Young's angle, θ_0, as follows,[82],[113],[114]

$$F_{ST} = 2\pi\gamma_{la} R^2 \cos^2(\theta_0) \frac{1}{\sqrt{(p-D)(p+D)}} \tag{6.3}$$

In the liquid drying experiments of GLAD-MACE samples, surface tension and Young's angle were the only two variables. If the Young's angle is fixed, when the liquid medium is changed from DI water to 2-propanol/methanol, the reduction in surface tension should lead to smaller capillary force and smaller nanowire clusters as calculated by equations 6.2 & 6.3. However, Young's angles of DI water and 2-propanol/methanol on Si surface are actually very different. Table 1 summarizes reported values of γ_{la} and measured values of θ_0 in the above experiment. The different liquid medium used in the drying process gives very different value for the term $\gamma_{la}\cos^2\theta_0$ in equations 6.2 & 6.3. It should be noted that the low surface tension of methanol and 2-propanol resulted in a very small Young's angle ($\theta_0 \sim 0°$), which made $\cos^2\theta_0$ approximate to 1. As shown in Table

6.1, the term $\gamma_{la}\cos^2\theta_0$ for methanol is the largest while that for DI water is the smallest. These calculations are very consistent with the observations from the SEM images that the nanowires dried in water had the smallest cluster size of nanowires and the largest cluster size was obtained by drying the sample in methanol.

Table 6.1: Surface Tension and Contact Angle for Different Liquid on Si Surface

	γ_{la} (mN/m) at 25 °C	θ_0 (°)	$\cos^2\theta_0$	$\gamma_{la}\cos^2\theta_0$
DI water	73	77	0.05	4
2-propanol	21	~0	1	21
methanol	22	~0	1	22

In addition, if one models the nanowire as a cantilever beam fixed at one end, a force exerted at the free end of the beam results in the largest deflection, i.e., the nanowires experience the largest deflection when the liquid meniscus is at the tips of the nanowires. The elastic force required to bend the nanowires is given by

$$F_E = \frac{3\pi E D^4 \delta}{64 h^3}, \tag{6.4}$$

where δ is the deflection of the nanowire.[82] As discussed in Section 6.3, the GLAD-MACE nanowires fabricated with reference deposition thickness of 200 nm were mesoporous as shown in the TEM image in Figure 6.2(d), as a result, their Young Modulus, *E*, were relatively small.[84] During the drying process, the thin nanowires experienced the largest deflection when the liquid meniscus was at the tips of the nanowires. The large capillary force caused a sufficiently large deflection to cause neighboring nanowires to touch each other and thereby

remained in a cluster form due to strong short-range van der Waals forces.[81]-[83] When the liquid medium was changed from 2-proponal/methanol to water, the applied capillary force decreases, resulting in smaller deflection and therefore smaller sized clusters.

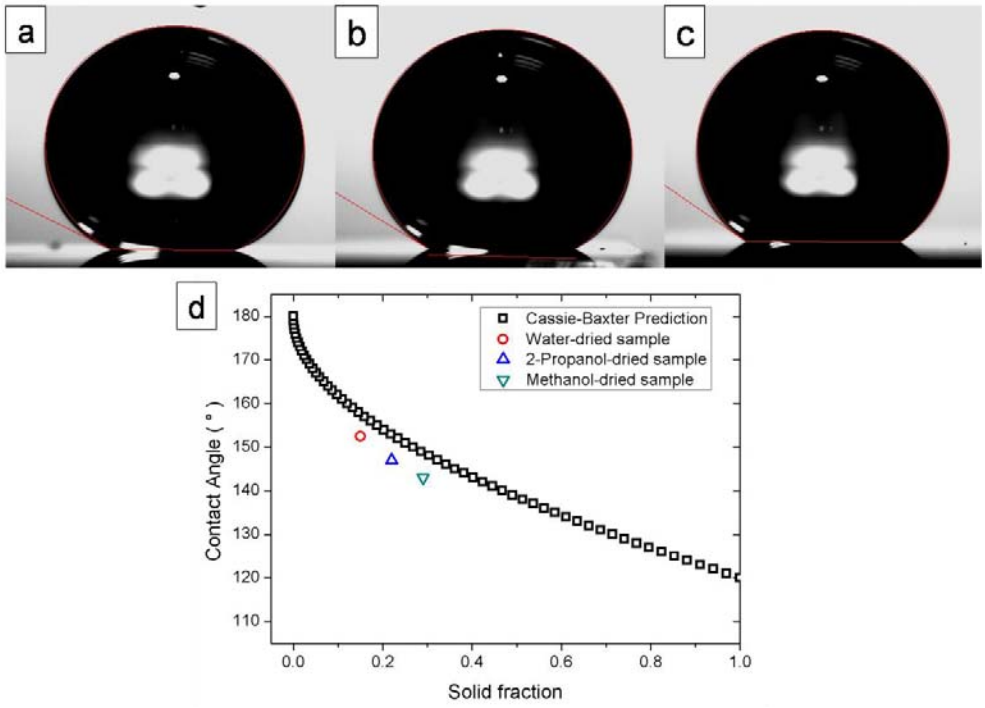

Figure 6.5: Contact angle measurements on (a) water-dried, (b) 2-propanol-dried and (c) methanol-dried silanized GLAD-MACE Si nanowire substrates. (d) The experimental contact angles at estimated corresponding solid fractions were compared with the Cassie-Baxter predicted values.

The static contact angle measurements on silanized GLAD-MACE Si nanowire surfaces dried by different liquid medium were demonstrated as depicted in Figures 6.5(a)-(c). The experimental results of the water contact angle and contact angle hysteresis on GLAD-MACE surfaces dried in water, 2-propanol and methanol were summarized in Table 6.2. Interestingly, the silanized water-

dried GLAD-CE sample exhibited the highest contact angle of 152.6° ± 0.2° with very low hysteresis of ~2°. In comparison, the 2-propanol dried sample exhibited a contact angle of 146.9° ± 0.1° with a hysteresis of 22° while the methanol-dried sample exhibited the smallest contact angle of 143.0° ± 0.1° with a hysteresis of 13°. These results showed that lotus effect and petal effect were successfully mimicked on GLAD-MACE Si nanowire surfaces dried in water and 2-propanol, respectively. As shown in Figure 6.5(d), the measured contact angles of these samples discussed above can be well explained by Cassie-Baxter equation (equation 6.1) using the solid factions estimated from the top-view SEM images of the nanostructures (Figure 6.4(a)-(c)).

Table 6.2: Experimental results of static water contact angle and contact angle hysteresis for GLAD-MACE surface dried by different liquid.

	contact angle (°)	contact angle hysteresis (°)
Water-dried	152.6 ± 0.2	2
2-propanol-dried	146.9 ± 0.1	22
Methanol-dried	143 ± 0.1	13

In order to understand the contact angle hysteresis of the GLAD-MACE samples with different cluster sizes, the percolation of the nanowire clusters were also analyzed using image processing techniques. Percolation describes the connectedness of nanowire clusters and represents the probability that there exists an open path from one end of the network of connected clusters to another.[115] Figure 6.5 shows the percolation results from digitally analyzed SEM images in Figures 6.4(a)-(c). To determine the percolation of the clusters obtained, the SEM

images were first digitized into black and white pixels to identify the tips of the nanowire clusters. The images at the bottom of Figure 6.6 denote the percolation analyzed by Matlab^{TM} image processing toolbox. For percolation analysis, the probability function, *g(r)*, that a site a distance *r* away belonging to the same cluster was calculated, with *g(r)* taken as an exponential $e^{-r/xi}$, where x_i is the percolation length. The image in Figure 6.6(a) indicates that the smaller clusters on the water-dried GLAD-MACE sample did not form percolation paths. Although the largest nanowire cluster size was obtained on methanol-dried sample, its percolation length was not as large as that for 2-propanol-dried sample as shown in Figures 6.5(b) & (c). The percolation results indicate that the nanowire clusters were more connected to each other when dried in 2-propanol as compared to methanol.

With the percolation analysis, the contact angle hysteresis of the samples can be explained using contact line pinning theory.[116]-[119] The contact line represents the region where the three phases, air liquid and solid meet. According to Quéré's model on a superhydrophobic surface with regular pillars in the Cassie state, contact line pinning occurs at the perimeter of the pillars as water recedes over the posts.[117] In addition, Dorrer and Rühe have shown that contact line pinning distorts the water meniscus of a water droplet resting on a post.[119] Both reports showed that as the droplet recedes, the greatest energy to move a contact line from one post to another occurs at the perimeter of the structure. In view of these arguments, it can be concluded that a larger perimeter leads to greater pinning and larger hysteresis.[117] If each nanowire cluster was assumed as a

single post, the circumference of the tips of the nanowire clusters gives the perimeter of this "post". The larger cluster size and percolation lengths in methanol-dried and 2-propanol-dried samples have a larger perimeter and therefore exhibit a larger pinning force on the water meniscus, which results in a larger contact angle hysteresis. The longer percolation length obtained from 2-propanol-dried sample represents a long contact line and therefore a large pinning capability, which explains the highest hysteresis obtained with this sample. The small cluster of nanowires in water-dried sample results in a small perimeter per cluster and has a smaller pinning capability and translates to the negligible contact angle hysteresis experimentally observed.

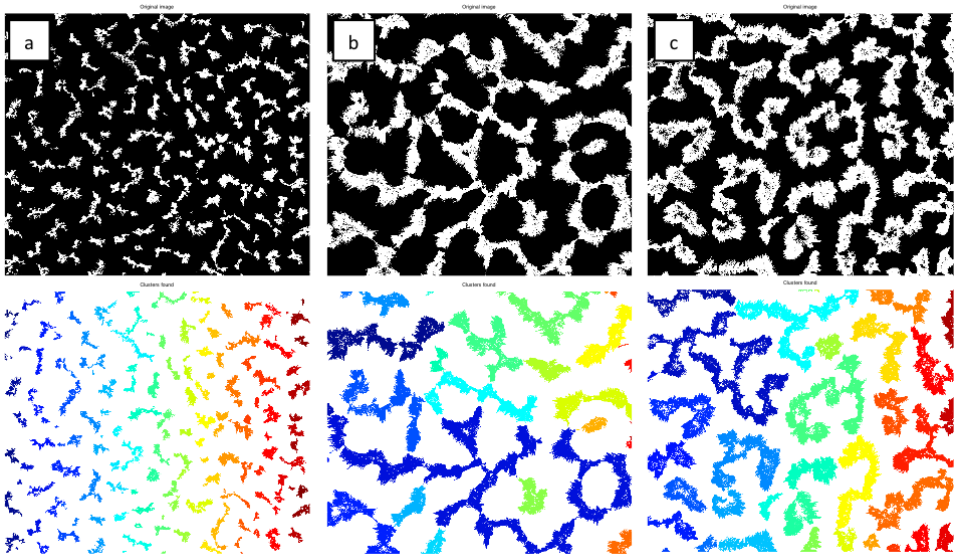

Figure 6.6: Percolation path simulated from digitized SEM images shown in Figure 6.4 (a)-(c). The top images represent the digitized SEM images selecting only the tips of the nanowire clusters. The images at the bottom show the percolation of (a) water-dried, (b) 2-propanol-dried and (c) methanol-dried samples.

6.5 Integrating Lotus-like and Petal-like surfaces on a Single Si Substrate

The versatility of the methods presented above in tuning the surface adhesion of superhydrophobic Si nanowire surfaces were further demonstrated by integrating the lotus-like and petal-like surfaces on a single substrate. Figure 6.7 shows the surface morphology of a GLAD-MACE sample with both straighter and clumped nanowires with a sharp boundary in between the two regions. The surface wetting characteristics of different regions is illustrated in the insets shown on the left. The lotus-like and petal-like surfaces were created on the same substrate by introducing a photolithographic photoresist patterning step prior to the GLAD process. After a short duration GLAD evaporation, the photoresist mask was removed, which was followed by an additional period of GLAD process on the entire sample surface so that Au nanoparticles of different size distributions could be formed in different regions. The photolithographic technique empowers this process with good patterning capability in terms of the shapes and sizes of the regions with surface morphology and wettability as demonstrate in the inset on the right of Figure 6.7.

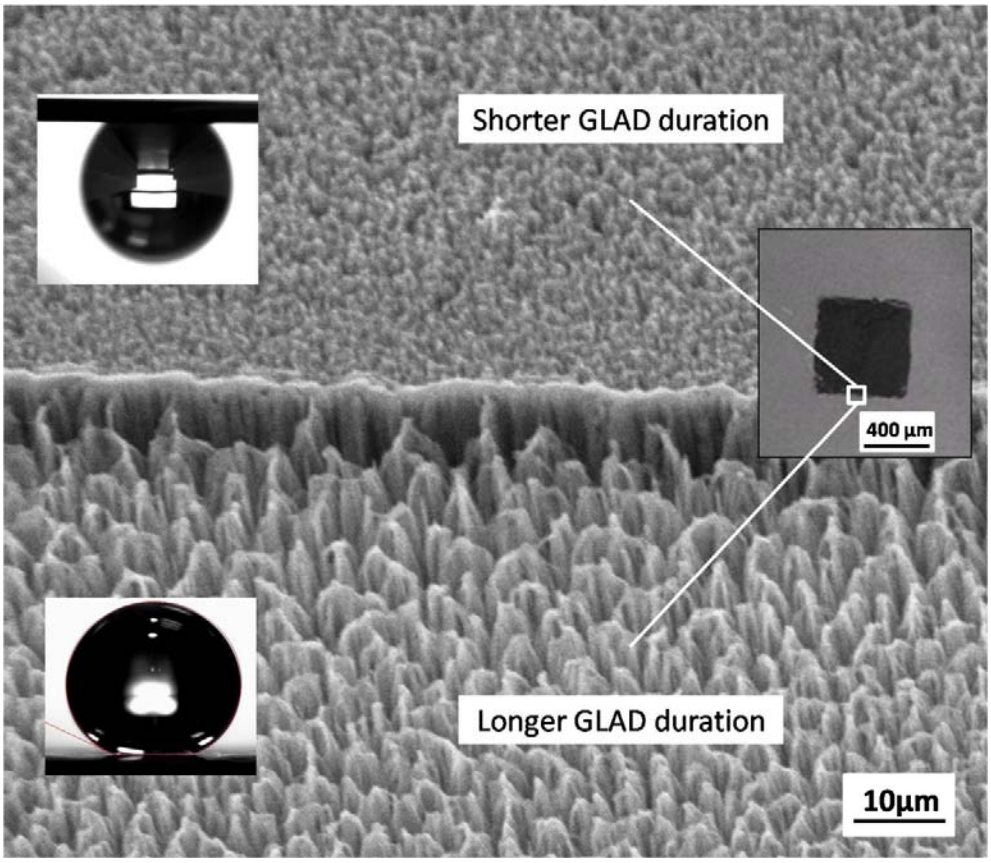

Figure 6.7: SEM of the hybrid lotus-like and petal-like GLAD-MACE Si nanowire surfaces on a single Si substrate fabricated using different GLAD durations. A sharp boundary was formed in between the high adhesion and low adhesion superhydrophobic surface. Insets on the left demonstrate the surface wettability at different regions. Inset on the right is the low magnification SEM image showing the regions of relatively straight and clumped nanowires (with straight nanowires inside the square).

Surface drying process after wet etching can also be used to create GLAD-MACE nanowire clusters of different sizes to spatially modulate the surface adhesion. Figure 6.8 depicts a GLAD-MACE sample with lotus-like and petal-like regions on the same substrate. When a droplet of water is placed on the DI water dried region, it tends to roll off the surface quickly. The droplet will be

pinned on the surface if it moves to the 2-propanol dried region. The water dried region and 2-propanol dried region are both superhydrophobic as proven by the static contact angle measurement results in the insets of Figure 6.8. Note that even though the surface drying method is simple, there will not be a sharp transition for the nanowire cluster sizes and the wetting behavior on this hybrid surface.

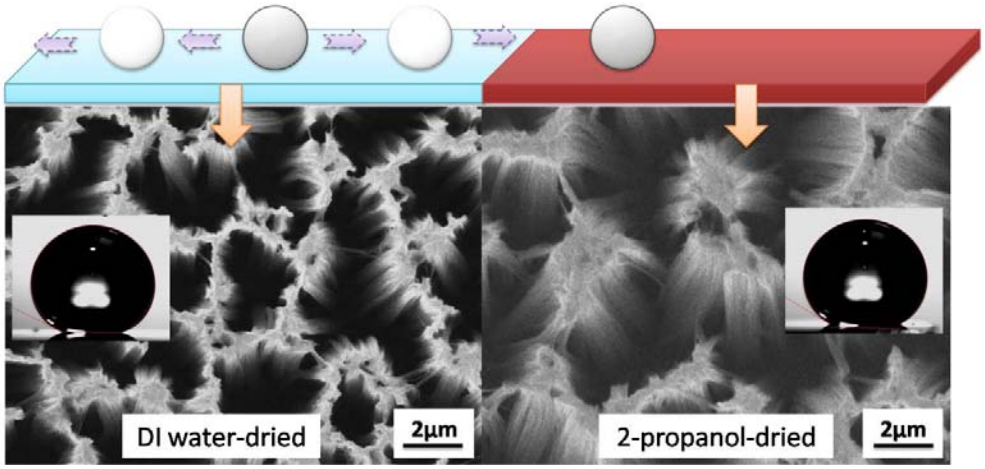

Figure 6.8: Integrating lotus-like and petal-like surfaces on a single GLAD-MACE sample by rinsing the freshly etched sample in DI water and half-immersed in 2-propanol. The surface morphologies of the regions dried by DI water and 2-propanol are shown in the SEM images. Surface contact angles measurements are also illustrated to show the superhydrophobicity of the sample.

6.6 Summary

In this chapter, the morphology of GLAD-MACE Si nanowire surface was controlled to modulate the surface wettability and mimick the lotus effect and petal effect. GLAD duration and surface drying medium were the two variables used to tune the surface adhesion while maintaining the surface superhydrophobicity. The surface contact angle measurement results on the Si

nanowire surfaces were analyzed with Cassie-Baxter model and the contact angle hysteresis results were also explained in this study. The lotus-like and petal-like surfaces were successfully integrated on a single substrate using these two simple methods.

Chapter 7 Silicon Nanowires as Anode for Lithium-ion Battery Application

7.1 Introduction

In this chapter, the performance of metal-assisted chemically etched sputtered Si nanowires as rechargeable lithium-ion (Li-ion) battery anode will be investigated. Firstly, the cycling performance of sputtered monolithic Si Li-ion battery anode will be studied with respect to varied Si thin film thickness. In order to reduce the impacts of pulverization and large volume change on battery capacity degradation during lithiation and delithiation cycles, IL-MACE and GLAD-MACE Si nanowires will be integrated into the battery anode. The cycling performance of IL-MACE and GLAD-MACE battery samples will be analyzed with respect to different nanowire heights. The rate performance and areal specific capacities of monolithic Si thin film, IL-MACE and GLAD-MACE Si nanowires based Li-ion batteries will also be investigated in this chapter.

7.2 Experimental Conditions

Sputtered Si films on stainless steel were used as starting substrates in this chapter. The substrate preparation procedures have been discussed in Section 3.3. Monolithic Si thin film was deposited at 85 W to investigate the effect of Si film thickness on the cycling performance of battery anode. The fabrication methods of IL-MACE and GLAD-MACE sputtered Si nanowires have been introduced in Chapter 4. The IL-MACE Si nanowires had a diameter of ~220 nm while the diameter of GLAD-MACE Si nanowires was around ~ 10 – 100 nm. Monolithic

Si films of different thickness were deposited at 30 W as higher deposition power might cause film delamination during MACE. Native oxide on the samples were removed by BOE etch (see Section 3.4.2) before battery assembly. The etching duration was controlled to form a remaining Si thin film with thickness of ~100 nm underneath the Si nanowires. If the Au catalysts reached the stainless steel surface, the Si nanowires were prone to delaminate due to over-etch. On the other hand, if the thickness of the remaining Si layer was too large, it might affect the battery performance.

Half-cells consisting of Si anodes were assembled in an Ar-filled glove box (with H_2O and O_2 levels less than 0.1 ppm). A schematic diagram of half-cell lithium-ion battery is illustrated in Figure 7.1. The Si on stainless steel substrate was used as the working electrode and a 1.2 cm diameter circular piece of Li foil was used as the reference counter electrode. The non-aqueous liquid electrolyte consisted of $LiPF_6$ (1.0 M) in 1 to 1 ratio of ethylene carbonate and diethyl carbonate. A glass micro-fiber filter was used to separate the two electrodes. The battery was assembled in an air tight two electrode cell with a plastic casing. Each of the electrode was connected to a stainless steel piston for electrical connection.

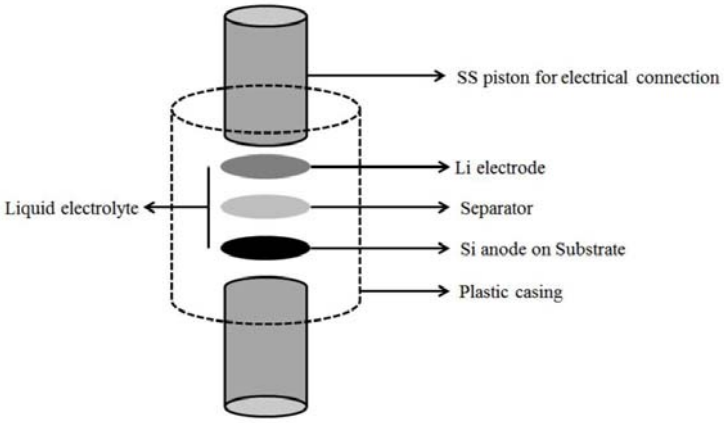

Figure 7.1: Schematic diagram of the assembly of a half-cell lithium ion battery.

Investigations of the electrochemical performance of our samples were performed outside the glove box. Galvanostatic cycling was carried out from 3.0 to 0.01 V with respect to the Li/Li^+ electrode using a NEWARE High Precision Battering Testing System. The discharge and charge cycles were referred to the lithiation and delithiation of the anode, respectively. The cycling process is depicted in Figure 7.2.[120] During the charge cycle, a constant current with a current density of 500 mAg^{-1} (except for rate performance experiments) passed through cathode (Li) and drove Li^+ in the electrolyte to Si anode. The Li^+ ions continued to react with Si to from alloys until the voltage drop to 0.01V. This was followed by the discharge cycle, which reversed the reaction and pushed Li+ back to the cathode. All the samples were weighed at appropriate stages using a RADWAG-MYA/2Y microbalance (with resolution ~0.001 mg) to determine the mass of the Si anode, for calculation of the gravimetric specific capacity. SEM was used to analyze the surface morphologies of the samples before and after

cycling. Before taking the SEM images, the cycled samples were rinsed in DI water to remove most of the solid-electrolyte interphase layer.

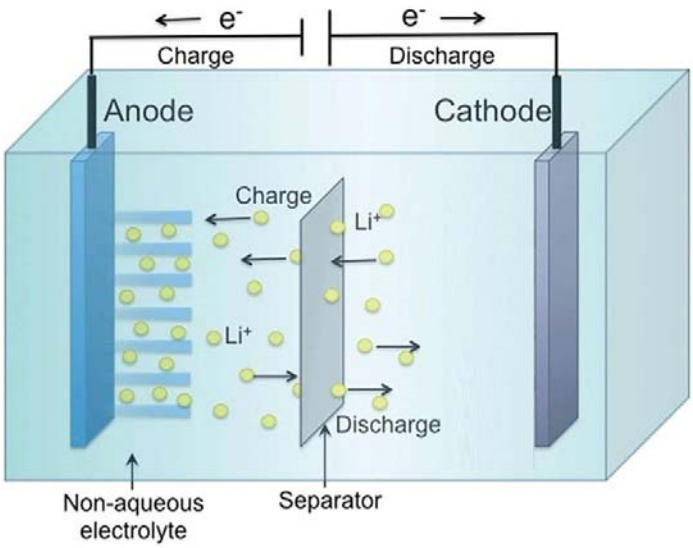

Figure 7.2: Schematic diagram of charge and discharge process of lithium ion battery.[120]

7.3 Monolithic Si as Battery Anode

Monolithic Si anodes were fabricated by sputtering Si thin films with a thickness of 200 nm, 550 nm and 1.1 μm on polished stainless steel substrate. Figure 7.3 shows that the cycling performance of the monolithic Si samples improves as the film thickness decreases. Severe capacity fade starting from the very early stage of the cycling process was observed on the 550 nm and 1.1 μm monolithic Si samples. At the mean time, cracking and delamination of Si thin films were observed on the 550 nm and 1.1 μm monolithic Si samples. As an example, the morphology change of thick Si thin film sample (1.1 μm) over 50 cycles of charging and discharging is shown in the insets of Figure 7.3. The

pulverization and delamination of the thick Si film was caused by the stress formed during the cycling process.[121] This morphology change resulted in loss of electrical contacts and could be accounted for the faster capacity degradation of the samples with thicker Si thin film. These results are in agreement with the report by Guo et al. [122] where a radio frequency sputtered 121 nm thick Si film showed much better cycling performance compared to another sample with a thickness of 523 nm. A similar dependence of cycling performance on film thickness was also reported by Takamura et al. [123] and Uehara et al. [124] for Si films deposited through evaporation.

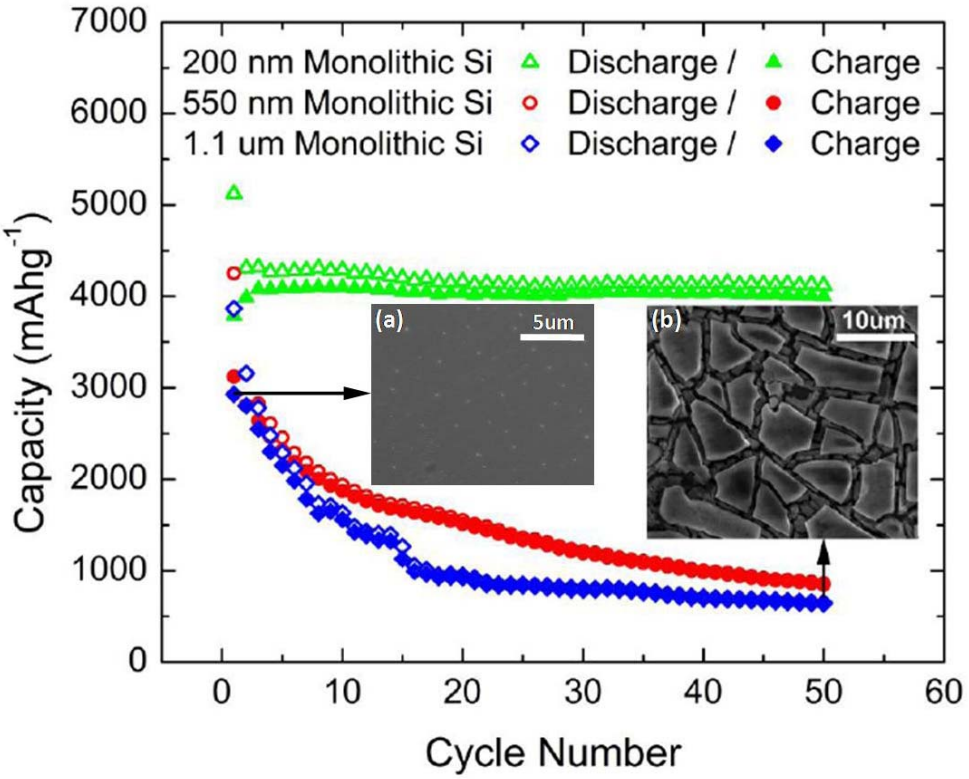

Figure 7.3: Cycling performance of monolithic sputtered Si thin film anode with different thicknesses. The SEM images in the insets illustrate the morphology of 1.1 µm monolithic Si sample (a) before and (b) after 50 cycles charge/discharge process.

7.4 GLAD-MACE Si Nanowires as Battery Anode

The synthesis method and characterization results of GLAD-MACE Si nanowires have been discussed previously in Section 4.3. In comparison to monolithic Si thin film, densely packed high aspect ratio GLAD-MACE Si nanowires have higher surface to volume ratio and more vacant space for volume expansion/extraction during lithiation/delithiation. The cycling performance of GLAD-MACE Si samples was investigated using GLAD-MACE nanowires with a height of 450 nm and 750 nm as anode material. It should be noted that a residual monolithic Si layer of ~100 nm thickness was maintained in between the nanowires and the stainless steel substrate to ensure good adhesion. Figure 7.4(c) shows the cycling performance of these two samples. Although the first-cycle gravimetric charge capacities of the samples were similar (750 nm: ~3200 $mAhg^{-1}$; 450 nm: ~3100 $mAhg^{-1}$), the 750 nm GLAD-MACE sample with higher Si nanowires had better cycling performance after 20 cycles (750 nm: 86% of initial capacity; 450 nm: 73% of initial capacity) and, therefore, was continued to test till 50 cycles. The different cycling performance of the battery anodes with shorter and longer Si nanowires can be explained by the change of surface morphology of the samples after the cycling process. SEM images of the GLAD-MACE samples before and after cycling are shown in Figures 7.4(a) & (b) and insets of Figure 7.4(c). The densely packed nanowires on the surface of the 450 nm GLAD-MACE sample (see Figure 7.4(a)) were reduced to a sparse distribution after 20 cycles (see inset (A) of Figure 7.4(c)). Though the 750 nm GLAD-MACE sample had relatively better cycling performance initially as compared to the 450 nm

sample, a marked degradation was found for the 750 nm sample after 20 cycles (see Figure 7.4(c)). SEM in inset (B) of Figure 7.4(c) reveals that GLAD-MACE Si nanowires disappeared after 50 cycles of lithiation and delithiation and large islands of Si with cracks were formed on the 750 nm GLAD-MACE sample, which was similar to the morphology of cycled thick monolithic Si thin film samples. These results indicate that GLAD-MACE Si nanowires were not robust enough to accommodate the volume change associated with pulverization and agglomeration during the cycling process.

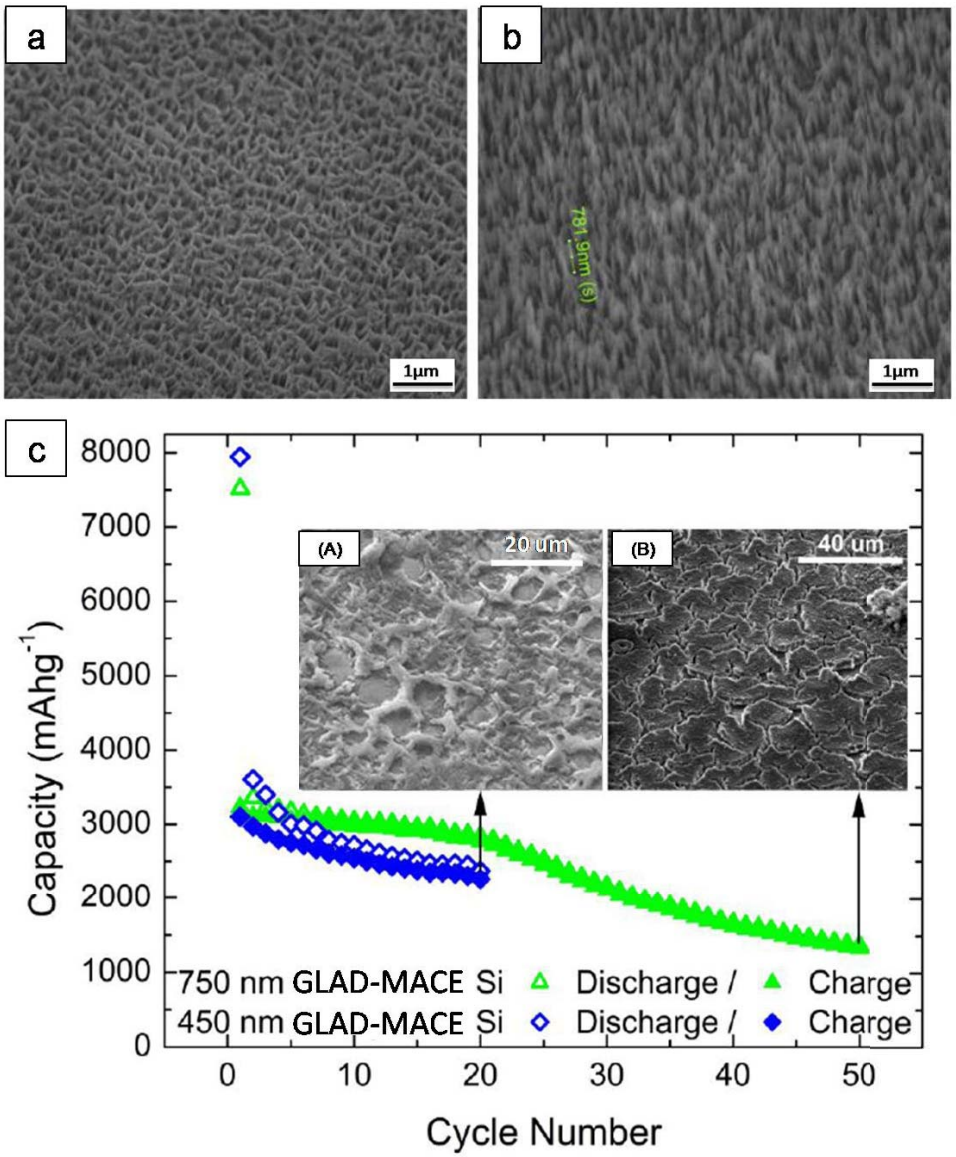

Figure 7.4: Surface morphology of GLAD-MACE samples with a Si nanowire height of (a) 450 nm and (b) 750 nm before cycling. (c) is the cycling performance plot for battery samples with GLAD-MACE Si nanowires as anode material. Insets of (c) are the surface morphologies of (A) 450 nm and (B) 750 nm GLAD-MACE samples after 20 and 50 cycles of lithiation and delithiation.

7.5 IL-MACE Si Nanowires as Battery Anode

To improve the cycling performance of Si nanowire based anode, battery samples with 450 nm and 750 nm long Si nanowires and ~100 nm residual monolithic Si layer were fabricated using IL-MACE technique. As compared to GLAD-MACE battery samples, IL-MACE sputtered Si nanowires with larger diameter and inter-wire distance were uniformly arranged on the substrate as depicted in Figure 7.5(a) & (b). As shown in Figure 7.5, the cycling performance of the IL-MACE samples with Si nanowires of different height were similar and both exhibited excellent cycling performance up to 50 cycles with good maximum charge capacity (750 nm: ~4000 $mAhg^{-1}$; 450 nm: ~3900 $mAhg^{-1}$). To understand the reason of the improved performance, IL-MACE samples were characterized by SEM and the results are shown in insets of Figure 7.5(c). It was found that the IL-MACE nanowires were still intact after 50 cycles of charging and discharging, despite the dimension changes of the nanowires (see insets of Figure 7.5(c)). The robustness of the nanowires was possibly contributed by the enhanced mechanical strength of the thicker and less porous nanowires to overcome volume expansion/extraction and the larger space between nanowires to better accommodate the volume change and avoid agglomeration. As the electrical connections were well maintained at the bottom of the IL-MACE Si nanowires, no severe capacity degradation was observed on the IL-MACE battery samples.

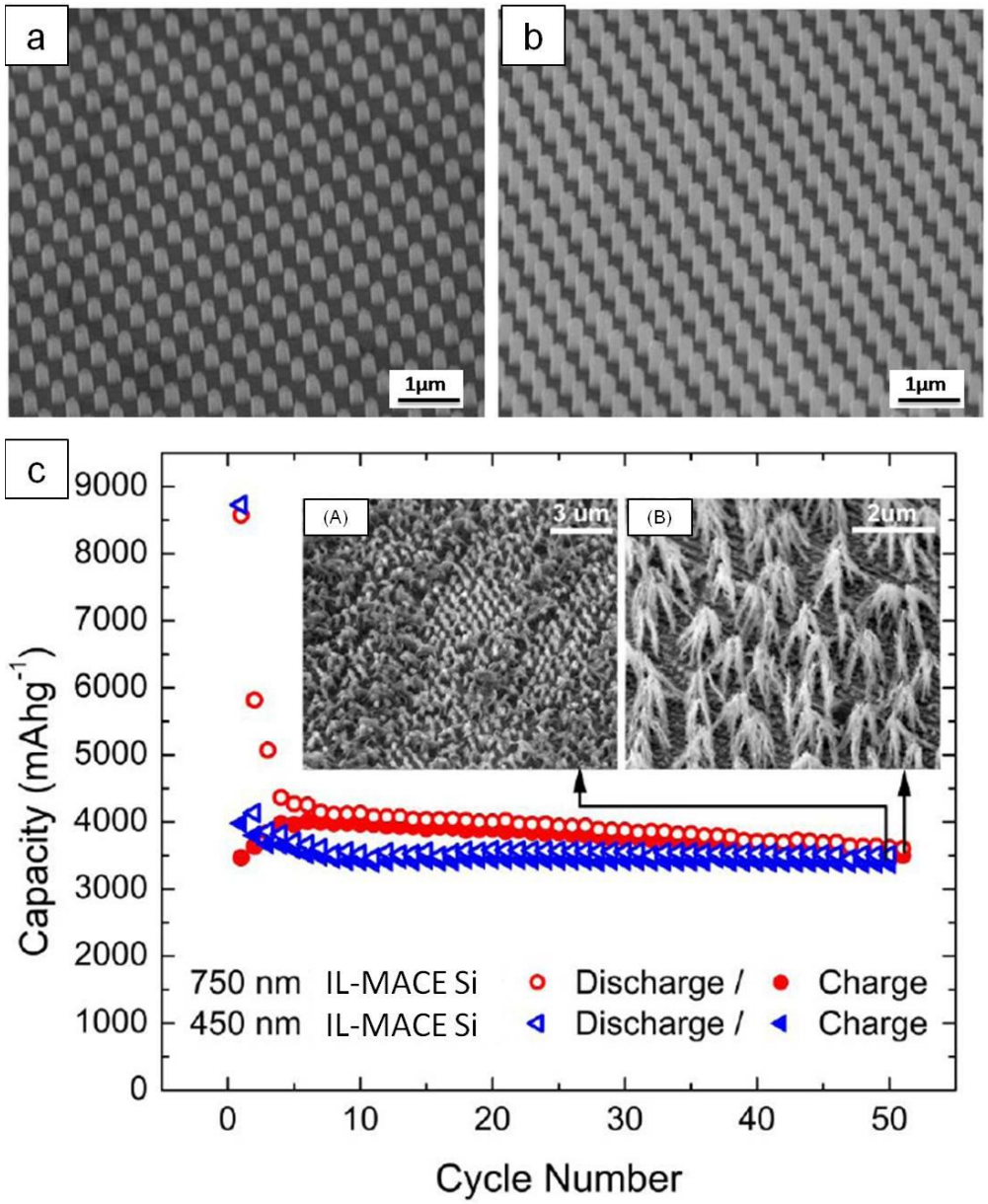

Figure 7.5: Surface morphology of IL-MACE samples with a Si nanoiwre height of (a) 450 nm and (b) 750 nm before cycling. (c) is the cycling performance plot for battery samples with IL-MACE Si nanowires as anode material. Insets of (c) are the surface morphologies of (A) 450 nm and (B) 750 nm IL-MACE samples after 20 and 50 cycles of lithiation and delithiation.

7.6 Rate Performance of Si Battery Anode

As discussed in Section 2.4.3, Si anodes have the advantage of higher specific capacity as compared to carbon. Nevertheless, since the diffusion coefficient of Li ions in Li-Si (~10^{-13} cm^2s^{-1}) is considerably lower than in Li-C (~10^{-10} cm^2s^{-1}), it is important to investigate the rate performance of Si anodes, especially at high current.[125]-[127] Figure 7.6 shows a comparison of the rate performance of 200 nm monolithic Si thin film, 450 nm IL-MACE Si nanowire and 450 nm GLAD-MACE Si nanowire samples. At 2000 mAg^{-1}, GLAD-MACE sample retained ~ 80% of its initial charge capacity at 500 mAg^{-1}, while IL-MACE sample had ~74% of its initial charge capacity at 500 mAg^{-1}. The rate performance of the Si nanowires samples was much better than that of the monolithic Si sample (only 62% of its 500 mAg^{-1} capacity at 2000 mAg^{-1}). The improved rate performance of the IL-MACE and GLAD-MACE samples could be explained by the reduced Li-ion diffusion length, increased surface area and improved electrical contact contributed by the Si nanowires. As the GLAD-MACE Si nanowires were much denser and thinner than the IL-MACE nanowires, the GLAD-MACE sample was found to have slightly better rate performance at high current. As shown in Figure 7.6, the rate performance results of the Si nanowire samples in this study were also compared with those reported in the literature and our high aspect ratio Si nanowires outperformed many other Si structures, such as short nanopillar array and Si opal shells.[128],[129]

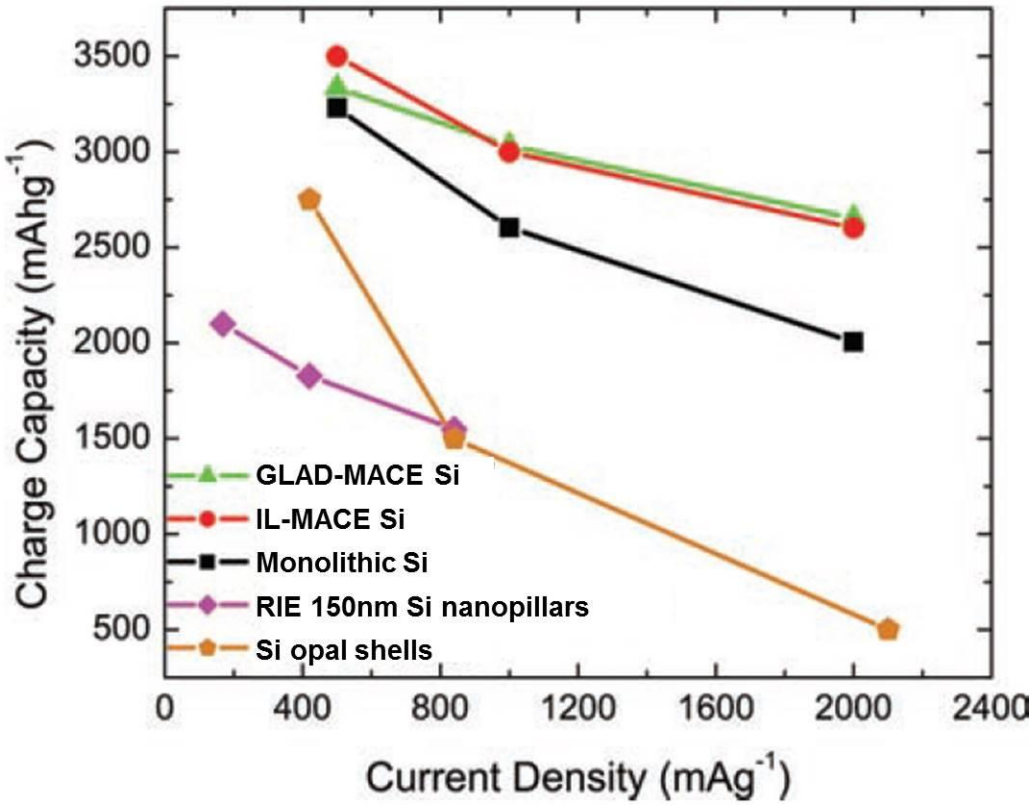

Figure 7.6: Plots of rate performance of monolithic, IL-MACE and GLAD-MACE Si samples with comparison to RIE 150nm Si nanopillars and Si opal shells.[128],[129]

7.7 Areal Specific Capacity of Si Battery Anode

The development of Li-ion micro-battery typically requires high areal specific capacity due to shrinking size of electronic and energy storage applications. In this section, the performance of monolithic Si and Si nanowires battery samples were compared using areal specific capacity as shown in Figure 7.7. The high surface to volume ratio of the Si nanowires could significantly increase the initial areal specific capacity of the Si anode batteries. As a result, the 750 nm GLAD-MACE Si nanowire battery sample had the highest initial areal specific capacity of ~0.24 $mAhcm^{-2}$ while the 200 nm monolithic Si thin film

sample showed the lowest initial areal specific capacity. However, as discussed in Section 7.4, pulverization and agglomeration of Si anode caused the cycling performance of GLAD-MACE battery sample to degrade significantly over the cycling process. As a result, IL-MACE battery sample with robust nanowires demonstrated good and stable areal specific capacity even after 50 cycles of lithiation and delithiation.

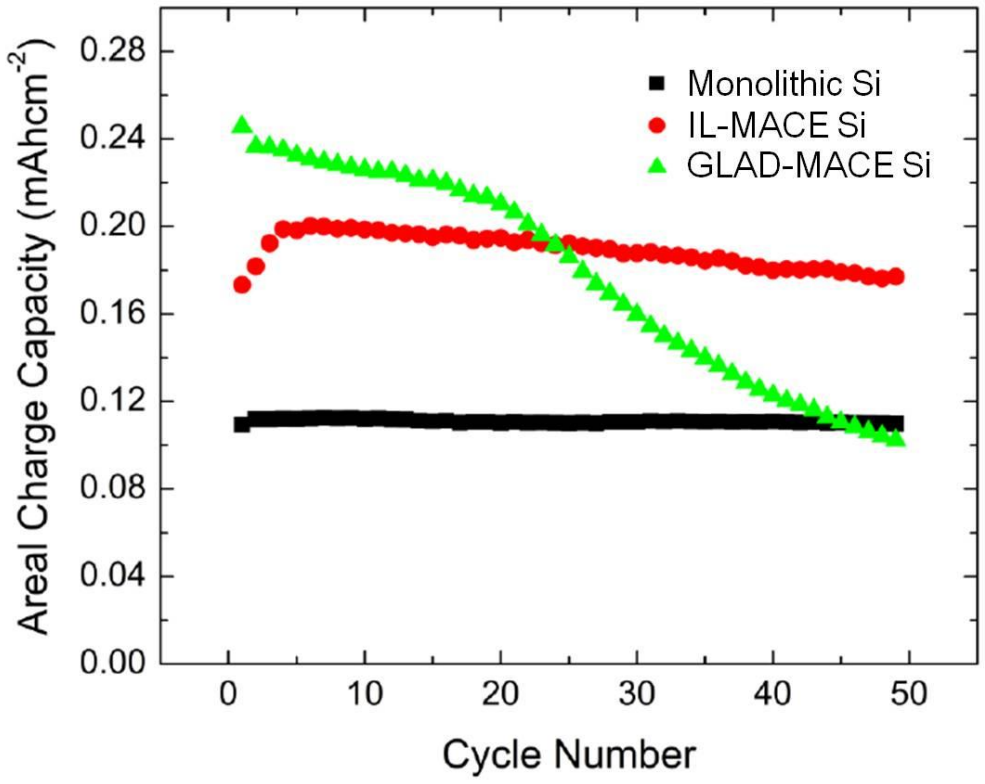

Figure 7.7: Plots of areal specific capacity of monolithic, IL-MACE and GLAD-MACE Si samples.

7.8 Summary

In this chapter, we have investigated the battery performance of monolithic Si thin film, GLAD-MACE Si nanowire and IL-MACE Si nanowire samples. The cycling performance of monolithic Si samples was limited by the Si thin film thickness due to pulverization and agglomeration issues associated with thicker films. To improve the cycling performance, GLAD-MACE and IL-MACE Si nanowires were integrated into the battery anode. Because of the morphology and volume change of the very thin Si nanowires, GLAD-MACE based battery degraded fast over many charging/discharging cycles. In comparison, IL-MACE nanowires with larger diameter and inter-wire space demonstrated the highest and most stable cycling performance. Moreover, the rate performance and areal specific performance of the 3 types of samples were compared in this study for more comprehensive evaluations. The Si nanowire samples showed better rate performance as compared to Si thin film sample due to reduced Li-ion diffusion length. Besides, very stable cycling performance with high areal charge capacitance was achieved on IL-MACE Si nanowire sample.

Chapter 8 Conclusions

8.1 Summary

In this study, two kinds of metal-assisted chemically etched Si nanowires, namely IL-MACE and GLAD-MACE nanowires, were synthesized, characterized and studied for the applications in bioanalytics, biomimetics and energy storage systems.

Metal-assisted chemical etching of Si is a unique wet etching method that has good control of anisotropic etching direction for the fabrication of high aspect ratio Si nanostructures. The diameter, period and cross-sectional shape of the metal-assisted chemically etched Si nanostructures are defined by the morphology of the noble metal coated on the Si surface. In this work, IL-MACE and GLAD-MACE methods were used to fabricate regular and random Si nanowires, respectively. The surface morphology of the nanowires was examined by SEM. Due to the excess holes injection during the etching process, Si nanowires fabricated by metal-assisted chemical etching had porous surface, which was investigated by TEM, BET and thermoporometry. It was found that GLAD-MACE nanowires had larger total surface area, total pore volume but smaller pore diameters as compared to IL-MACE Si nanowires.

With high surface-to-volume ratio, metal-assisted chemically etched Si nanowire substrates were used to create high loading capacity platform for detections of DNA and protein using an analyte-specific homogeneous mixing strategy. The surface loading capacities of the IL-MACE, GLAD-MACE (Au)

and GLAD-MACE (Ag) Si nanowire substrates were first evaluated by functionalizing the surface with amine group and directly coupling dye molecules (Cy5-NHS) on the sample surfaces. The reason for high surface loading capacity on GLAD-MACE (Au) sample was studied by comparing the results on the substrates with different surface morphologies and porosity. It was concluded that surface porosity was the primary factor and clumping of nanowires was the secondary factor for determining the loading capacity of metal-assisted chemically etched Si nanowire surfaces. As GLAD-MACE (Au) samples showed the highest loading capacity, they were further functionalized by carboxylation and coupled of sense ssDNA. The subsequent DNA and protein detections were performed by hybridization of dye-modified anti-sense ssDNA and conjugated analyte-antibody-anti-sense-DNA (analyte-ASR) complex onto the complementary sense-DNA immobilized on the nanowire substrate. The capturing efficiencies of sense-DNA, anti-sense-DNA and analyte-ASR complex on the GLAD-MACE (Au) samples showed enhance performance with up to 250 fold increase of signal intensities as compared to those on flat Si control samples. The potential of the protein microarray application of the nanowire substrates was further demonstrated by detecting IL-8 protein, an important sepsis biomarker, spiked in human serum. Preliminary results showed that a lower detection limit of ~1nM can be achieved for IL-8 protein on GLAD-MACE Si nanowire substrates.

Biomimetics of lotus and petal effects was also demonstrated using GLAD-MACE nanowires coated with organosilane with low surface energy. The GLAD duration was tuned to deposit Au nanoparticles of different surface

morphology. Due to the shadowing effect in the GLAD process, densely packed large Au nanoparticles with embedded smaller particles were formed on the longer-duration GLAD samples. As the samples with different GLAD durations had different porosity as shown in TEM images, relatively straight and clumped Si nanowires were obtained for shorter and longer duration GLAD samples, respectively. The different surface morphologies resulted in different surface adhesions of the silanized superhydrophobic surfaces of the GLAD-MACE samples. The contact angle of these lotus-like and petal-like surfaces was explained by the Cassie-Baxter model and the contact angle hysteresis was modeled by attractive van der Waals force and capillary adhesion. Making use of the high porosity of longer-duration GLAD samples, different drying methods were also used as an alternative route to modulate the surface morphology and wetting behavior of the GLAD-MACE samples. GLAD-MACE nanowires were dried by DI water, 2-propanol and methanol to create clumped nanowires with different cluster sizes. It was found that lotus-like and petal-like superhydrophobic surfaces were obtained on the silanized DI water dried and 2-propanol dried GLAD-MACE samples. The surface contact angles and surface adhesion were explained by Cassie-Baxter model and contact line pinning on samples with different percolation paths, respectively. The versatility of these two methods was presented by integrating the artificially fabricated lotus-like and petal-like superhydrophobic surfaces on a single substrate.

The performance of lithium ion battery with amorphous IL-MACE and GLAD-MACE Si nanowires as anode material was investigated in this study.

Monolithic Si thin films with different thickness were first examined to build a baseline for the Si anode battery performance. As the performance of Si thin film samples suffered from pulverization, cracking and large volume change issues during cycling, metal-assisted chemically etched Si nanowires were designed to be integrated to the battery anode for performance improvement. The battery performance of GLAD-MACE Si nanowires with a height of 450 nm and 750 nm showed degradation within 50 cycles. SEM results showed that the surface morphology changed severely during the charging and discharging process and the GLAD-MACE Si nanowires disappeared after cycling. The results indicated that GLAD-MACE Si nanowires were not robust enough to be used as Li-ion battery anode. On the other hand, IL-MACE nanowire based anode showed good cycling performance after 50 cycles, which was possibly contributed by the larger space between nanowires and enhanced mechanical strength of the thicker and less porous nanowires. The rate performance and areal specific capacity were also investigated for the monolithic Si thin film, IL-MACE and GLAD-MACE Si nanowire battery anodes.

8.2 Recommendations

In this study, GLAD-MACE Si nanowire substrates were used to fabricate protein microarray with high sensitivity and specificity. Preliminary results of sepsis diagnosis were obtained by detecting IL-8 protein on the GLAD-MACE bioanalytic platform. The lower detection limit of ~1nM was reached in the experiments described in this report. However, septic response is a complicated process and it is very difficult to differentiate sepsis from other inflammatory

reactions.[130] In order to accurately diagnose sepsis, many other biomarkers such as PCT, CRP and IL-6 need to be tested on the GLAD-MACE microarray.[130] In addition, the severity of diseases like sepsis increases very fast within a short period of time, which makes early stage detection an important requirement for protein microarray. To shorten the diagnostic procedures, the stationary incubation process for DNA immobilization and ASR hybridization can be improved by introducing microfluidic channels to overcome the diffusion barrier. Furthermore, the detection limit can be improved to pM or even fM range by optimizing the capturing chemistry and enhance the signal amplification response. The sensitivity of the biomedical detections is critical for early stage diagnosis.

The biomimetics of lotus effect and petal effect on Si nanowires have great potential for wide range of applications, such as self-cleaning, energy conservation, drag reduction and manipulation of liquid flow. Functional superhydrophobic and superhydrophilic surfaces can be integrated onto the side wall and bottom surface of microfluidic channels to improve and regulate the microfluidic flow for applications like drug delivery. Note that superhydrophilic surface can be simply created by Si nanowire surface without any additional coating. The microfluidic device with functional surfaces can also be utilized for the bioanalytic DNA and protein microarrays as discussed in the last paragraph.

The performance of Si nanowire based lithium ion battery anode can be further enhanced by using longer and denser IL-MACE nanowire. The increased nanowire height and density will lead to higher areal specific capacity. But it

should be noted that higher Si nanowires may result in weaker mechanical strength of the nanowires. The density of the nanowires needs to be optimized to be able to mitigate the volume change during charging and discharging cycles.

Bibliography

[1] S. K. Prasad, *Advanced Nanotechnology*, Discovery Publishing House PVT. LTD., New Delhi (2008).

[2] Y. Wang, T. Wang, P. Da, M. Xu, H. Wu and G. Zheng, *Adv. Mater.*, **25**, 5177 (2013).

[3] Z. Huang, N. Geyer, P. Werner, J. de Boor and U. Gosele, *Adv. Mater.*, **23**, 285 (2010).

[4] V. Schmidt ,J. V. Wittemann ,S. Senz and U. Gösele, *Adv. Mater.*, **21**, 2681 (2009).

[5] R. S. Wagner and W. C. Ellis, *Appl. Phys. Lett.*, **4**, 89 (1964).

[6] S. Chung, J. Yu and J. R. Heath, *Appl. Phys. Lett.*, **76**, 2068 (2000).

[7] Y. Wu, Y. Cui, L. Huynh, C. J. Barrelet, D. C. Bell and C. M. Lieber, *Nano Lett.*, **4**, 433 (2004).

[8] Y. Wu, J. Xiang, C. Yang, W. Lu and C. M. Lieber, *Nature*, **430**, 61 (2004).

[9] A. M. Morales and C. M. Lieber, *Science*, **279**, 208 (1998).

[10] Y. Wang, T. Wang, P. Da, M. Xu, H. Wu and G. Zheng, *Adv. Mater.*, **25**, 5177 (2013).

[11] Y. Cui, L. H. Lauhon, M. S. Gudiksen, J. Wang and C. M. Lieber, *Appl. Phys. Lett.*, **78**, 2214 (2001).

[12] S. Sharma, T. I. Kamins and R. Stanley Williams, *Appl. Phys. A.*, **80**, 1225 (2005).

[13] S. Kodambaka, J. Tersoff, M. C. Reuter and F. M. Ross, *Phys. Rev. Lett.*, **96**, 096105 (2006).

[14] A. Y. Cho and J. R. Arthur, *Prog. Solid State Chem.*, **10**, 157 (1975).

[15] Y. Cho, *Journal of Crystal Growth*, **201/202**, 1 (1999).

[16] P. Werner, N. D. Zakharov, G. Gerth, L. Schubert and U. Gosele, *Int. J. Mater. Res.*, **97**, 1008 (2006).

[17] P. Das Kanungo, N. Zakharov, J. Bauer, O. Breitenstein, P. Werner and U. Gosele, *Appl. Phys. Lett.*, **92**, 263107 (2008).

[18] L. Schubert, P. Werner, N. D. Zakharov, G. Gerth, F. M. Kolb, L. Long, U. Gosele and T. Y. Tan, *Appl. Phys. Lett.*, **84**, 4968 (2004).

[19] Y. F. Zhang, Y. F. Tang, N. Wang, C. S. Lee, I. Bello and S. T. Lee, *Appl. Phys. Lett.*, **72**, 1835 (1998).

[20] W. K. Choi, T. H. Liew, M. K. Dawood, H. I. Smith, C. V. Thompson and M. H. Hong, *Nano Lett.*, **8**, 3799 (2008).

[21] H. Liu, D. K. Biegelsen, N. M. Johnson, F. A. Ponce and R. F. W. Pease, *J. Vac. Sci. Technol. B*, **11**, 2532 (1993).

[22] C.-M. Hsu, S. T. Connor, M. X. Tang and Y. Cui, *Appl. Phys. Lett.*, **93**, 133109 (2008).

[23] J. T. L. Thong, Y. Bai, P. Luo and W. K. Choi, *Materials Science and Engineering B*, **72**, 177 (2000).

[24] B. Wu, A. Kumar and S. Pamarthy, *J. Appl. Phys.*, **108**, 051101 (2010).

[25] N. Singh, K. D. Buddharaju, S. K. Manhas, A. Agarwal, S. C. Rustagi, G. C. Lo, N. Balasubramanian and D.-L. Kwong, *IEEE Trans. Electron Devices*, **55**, 3107 (2008).

[26] V. M. Donnelly and A. Kornblit, *J. Vac. Sci. Technol. A*, **31**, 050825 (2013).

[27] P. Verdonck, *Plasma etching*, UNICAMP, Brazil (2006).

[28] R. J. Shul, S. J. Pearton. *Handbook of advanced plasma processing techniques*, Springer, 2000.

[29] J. I. A. Rashid, J. Abdullah, N. A. Yusof and R. Hajian, *Journal of Nanomaterials*, **2013**, 328093 (2013).

[30] C. K. Chan, H. Peng, G. Liu, K. Mcllwrath, X. F. Zhang, R. A. Huggins and Y. Cui, *Nat. Nanotechnol.*, **3** , 31 (2008).

[31] H. Wu and Y. Cui, *Nano Today*, **7**, 414 (2012).

[32] X. Li and P. W. Bohn , *Appl. Phys. Lett.*, **77** , 2572 (2000).

[33] C. Chartier, S. Bastide and C. Levy-Clement, *Electrochimica Acta*, **53**, 5509 (2008).

[34] K. Peng, A. Lu, R. Zhang and S. T. Lee, *Adv. Funct. Mater.*, **18**, 3026 (2008).

[35] S. L. Cheng, C. H. Chung and H. C. Lee, *J. Electrochem. Soc.*, **155**, D711 (2008).

[36] K. Rykaczewski, O. J. Hildreth, C. P. Wong, A. G. Fedorov and J. H. J. Scott, *Nano Lett*., **11**, 2369 (2011).

[37] V. Lehmann , *J. Electrochem. Soc.*, **140**, 2836 (1993).

[38] K. Q. Peng , M. L. Zhang , A. J. Lu , N. B. Wong , R. Q. Zhang and S. T. Lee, *Appl. Phys. Lett.*, **90**, 163123 (2007).

[39] X. G. Zhang, *Electrochemistry of Silicon and Its Oxide*, Kluwer Academic/ Plenum Publisher, New York (2001).

[40] W. Chern, K. Hsu, I. Chun, B. P. de Azeredo, N. Ahmed and K.-H. Kim, *Nano Lett.*, **10**, 1582 (2010).

[41] Z. Huang, T. Shimizu, S. Senz, Z. Zhang, N. Geyer and U. Gosele, *J Phys Chem C*, **114**, 10683 (2010).

[42] P. M. M. C. Bressers , J. J. Kelly , J. G. E. Gardeniers and M. Elwenspoek, *J. Electrochem. Soc.*, **143**, 1744 (1996).

[43] A. I. Hochbaum, D. Gargas, Y. J. Hwang and P. Yang, *Nano Lett.*, **9**, 3550 (2009).

[44] M. Khorasaninejad, N. Abedzadeh, J. Walia, S. Patchett and S. Saini,

Nano Lett., **12**, 4228 (2012).

[45] F. Patolsky, G. Zheng and C. M. Lieber, *Nat. Protocol.*, **1**, 1711 (2006).

[46] F. Patolsky, G. Zheng and C. M. Lieber, *Nanomedicine*, **1**, 51 (2006).

[47] B. R. Murthy, J. K. Ng, E. S. Selamat, N. Balasubramanian and W. T. Liu, *Biosens. Bioelectron.*, **24**, 723 (2008).

[48] P. Serre, C. Ternon, V. Stambouli, P. Periwal and T. Baron, *Sensors and Actuators B*, **182**, 390 (2013).

[49] S. W. Han, S. Lee, J. Hong, E. Jang, T. Lee and W. G. Koh, *Biosensors and Bioelectronics*, **45**, 129 (2013).

[50] L. Jiang, R. Wang, B. Yang, T. J. Li, D. A.Tryk, A. Fujishima, K. Hashimoto and D.B. Zhu, *Pure and Applied Chemistry*, **72**, 73 (2000).

[51] L. Feng, S. Li, Y. Li, H. Li, L. Zhang, J. Zhai, Y. Song, B. Liu, L. Jiang and D. Zhu, *Adv. Mater.*, **14**, 1857 (2002).

[52] D. Xia, L. M. Johnson, G. P. Lõpez, *Adv. Mater.*, **24**, 1287 (2012).

[53] Z. Guo, W. Liu, B.-L. Su, *J. Colloid Interface Sci.*, **353**, 335 (2011).

[54] B. Bhushan, Y. C. Jung, *Progress in Materials Science*, **56**, 1 (2011).

[55] J. W. M. Bush, D. L. Hu, M. Prakash, *Insect Mechanics and Control*, **34**, 117 (2007).

[56] M. Nosonovskiĭ, B. Bhushan, *Multiscale dissipative mechanisms and hierarchical surfaces: friction, superhydrophobicity, and biomimetics*, Springer, Heidelberg (2008).

[57] Y. Zheng, X. Gao, L. Jiang, *Soft Matter*, **3**, 178 (2007).

[58] W. Barthlott, C. Neinhuis, *Planta*, **202**, 1 (1997).

[59] L. Feng, Y. Zhang, J. Xi, Y. Zhu, N. Wang, F. Xia, L. Jiang, *Langmuir*, **24**, 4114 (2008).

[60] B. Bhushan, E. K. Her, *Langmuir*, **26**, 8207 (2010).

[61] X. Zhang, F. Shi, J. Niu, Y. Jiang, Z. Wang, *J. Mater. Chem.*, **18**, 621 (2008).

[62] S. Zhu, Y. Li, J. Zhang, C. Lü, X. Dai, F. Jia, H. Gao, B. Yang, *J. Colloid Interface Sci.*, **344**, 541 (2010).

[63] M. Liu, L. Jiang, *Adv. Func. Mater.*, **20**, 3753 (2010).

[64] Y. Nishi, *Journal of Power Sources*, **100**, 101 (2001).

[65] J. M. Tarascon and M. Armand, *Nature*, **414**, 359 (2001).

[66] H. Wu and Y. Cui, *Nano Today*, **7**, 414, (2012).

[67] N. S. Choi, Y. Yao, Y. Cui and J. Cho, *Journal of Materials Chemistry*, **21**, 9825 (2011).

[68] K. Q. Peng, J. S. Jie, W. J. Zhang and S. T. Lee, *Applied Physics Letters*, **93**, 033105 (2008).

[69] R. Huang, X. Fan, W. C. Shen and J. Zhu, *Applied Physics Letters*, **95**, 133119 (2009).

[70] W. Kern and D. A. Puotinen, *RCA Rev*., **31**, 187 (1970).

[71] W. K. Choi, T. H. Liew, M. K. Dawood, H. I. Smith, C. V. Thompson and M. H. Hong, *Nano Letters*, **8**, 3799 (2008).

[72] Q. Xie , M. H. Hong , H. L. Tan , G.X. Chen , L. P. Shi and T. C. Chong T.C. *Journal of Alloys and Compounds*, **449**, 261(2008).

[73] L. T. Haw, *Fabrication of Large area and precisely located nanostructures on silicon by interference lithography*, Ph. D Thesis, National University of Singapore, Singapore (2009).

[74] J. J. Steele and M. J. Brett, *Journal of Materials Science: Materials in Electronics*, **18**, 367 (2007).

[75] Y.-P. Zhao, D.-X. Ye, G.-C. Wang, T.-M. Lu, *Proceedings of SPIE*, **5219**, 59 (2003).

[76] https://www.purdue.edu/ehps/rem/rs/sem.htm

[77] http://www.microscopy.ethz.ch/TEMED.htm

[78] M. Thommes, *Chemie Ingenieur Technik*, **82**, 1059 (2010).

[79] W. Kuhn, E. Peterli, H. Majer and J. Polym. *Science*, **16**, 539 (1955).

[80] M. Brun, A. Lallemand, J.-F. Quinson and C. Eyraud, *Thermochim. Acta.*, **21**, 59 (1977).

[81] S. H. Kang, B. Pokroy, L. Mahadevan and J. Aizenberg, *ACS Nano*, **4**, 6323 (2010).

[82] J. J. Hill, K. Haller, B. Gelfand and K. J. Ziegler, *ACS Appl. Mater. Interfaces*, **2**, 1992 (2010).

[83] H. Duan and K. K. Berggren, *Nano Lett.*, **10**, 3710 (2010).

[84] H. Magoariec and A. Danescu, *Phys. Status Solidi C*, **7**, 1680 (2009).

[85] K. Tsujino and M. Matsumura, *Electrochem. Solid St. Lett.*, **8**, C193 (2005).

[86] C. L. Lee, K. Tsujino, Y. Kanda, S. Ikeda and M. Matsumura, *J. Mater.Chem.*, **18**, 1015 (2008).

[87] S. Chattopadhyay, X. L. Li and P. W. Bohn, *J. App. Phys.*, **91**, 6134 (2002).

[88] K. Q. Peng, Y. J. Yan, S. P. Gao and J. Zhu, *Adv. Funct. Mater.*, **13**,127 (2003).

[89] T. Hadjersi, N. Gabouze, E. S. Kooij, A. Zinine, A. Ababou, W. Chergui, H. Cheraga, S. Belhousse and A. Djeghri, *Thin Solid Films,* **459**, 271 (2004).

[90] M. K. Dawood, T. H. Liew, P. Lianto, M. H. Hong, S. Tripathy, J. T. L. Thong and W. K. Choi, *Nanotechnology*, **21**, 205305 (2010).

[91] J. K. Ng, P. K. Ajikumar, Y. C. Tang and J. Y. Lee, G. Stephanopoulos and H. P. Too, *Electrophoresis*, **28**, 4638 (2007).

[92] P. K. Ajikumar, J. Kiat, Y. C. Tang, J. Y. Lee, G. Stephanopoulos and H. P. Too, *Langmuir*, **23**, 5670 (2007).

[93] Y. C. Tang, G. Wan, J. K. Ng, P. K. Ajikumar and H. P. Too, *Front. Biosci.*, **13**, 5755 (2008).

[94] C. E. Hack, M. Hart, R. J. Schijndel, A. J. Eerenberg, J. H. Nuijens, L. G. Thijs and L.A. Aarden, *Infection and Immunity*, **60**, 2835 (1992).

[95] Y. Hirao, T. Kanda, Y. Aso, M. Mitsuhashi and I. Kobayashi, *Microbiology*, **31**, 39 (2000).

[96] C. Neinhuis and W. Barthlott, *Ann. Bot.*, **79**, 667 (1997).

[97] W. Barthlott and C. Neinhuis, *Planta*, **202**, 1 (1997).

[98] B. Bhushan and E. K. Her, *Langmuir*, **26**, 8207 (2010).

[99] M. Liu, Y. Zheng, J. Zhai and L. Jiang, *Accounts of Chemical Research*, **43**, 368 (2010).

[100] R. N. Wenzel. Indust. *Eng. Chem.*, **28**, 988 (1936).

[101] A. Cassie and S. Baxter, *Trans. Faraday. Soc.*, **40**, 546 (1944).

[102] Y. X. Zhuang, O. Hansen, T. Knieling, C. Wang, P. Rombach, W. Lang, W. Benecke, M. Kehlenbeck and J. J. Koblitz, *Micromech. Microeng.*, **16**, 2259 (2006).

[103] K. Robbie, J. C. Sit and M. J. Brett, J. Vac. *Sci. Technol. B*, **16**, 1115 (1998).

[104] A. Winkleman, G. Gotesman, A. Yoffe and R. Naaman, *Nano Lett.*, **8**, 1241 (2008).

[105] P.-G. de Gennes, F. Brochard-Wyart and D. Quéré, *Capillarity and Wetting Phenomena Drops, Bubbles, Pearls, Waves*, Springer Science Business Media Inc., New York, (2004).

[106] K. Autumn, Y. A. Liang, S. T. Hsieh, W. Zesch, W. P. Chan, T. W. Kenny, R. Fearing and R. J. Full, *Nature*, **405**, 681 (2000).

[107] K. Autumn, M. Sitti, Y. A. Liang, A. M. Peattie, W. R. Hansen, S. Sponberg, T. W. Kenny, R. Fearing, J. N. Isrealachivili and R. J. Full, *Proc. Natl. Acad. Sci. U.S.A*., **99**, 12252 (2002).

[108] X. Israelachvili, *Intermolecular and Surface Forces*, Academic Press: London (1985).

[109] Y. Lai, X. Gao, H. Zhuang, J. Huang, C. Lin and L. Jiang, *Adv. Mater.*, **21**, 3799 (2009).

[110] W. K. Cho and I. S. Choi, *Adv. Funct. Mater.*, **18**, 1089 (2008).

[111] Y. Xiu, S. Zhang, V. Yelundur, A. Rohatgi, D. W. Hess and C. P. Wong, *Langmuir*, **24**, 10421 (2008).

[112] V. Zorba, E. Stratakis, M. Barberoglou, E. Spanakis, P. Tzanetakis, S. H. Anastasiadis and C. Fotakis, *Adv. Mater.*, **20**, 4049 (2008).

[113] D. Chandra, S. Yang, A. Soshinsky and R. Gambogi, *ACS Appl. Mater. Interfaces*, **1**, 1698 (2009).

[114] P. A. Kralchevsky, V. N. Paunov, I. B. Ivanov and K. J. Nagayama, *J. Colloid Interface Sci.*, **151**, 79 (1992).

[115] H. Kesten, *Not. AMS*, **53**, 572 (2006).

[116] T.-K. Wong and C.-M. Ho, *Langmuir*, **25**, 12851 (2009).

[117] C. W. Extrand, *Langmuir*, **18**, 7991 (2002).

[118] D. Quéré, *Annu. Rev. Mater. Res.*, **38**, 71 (2008).

[119] C. Dorrer and J. Ruhe, *Langmuir*, **23**, 3179 (2007).

[120] P. Roy and S. K. Srivastava, *J. Mater. Chem. A*, Advance Article (2015).

[121] C. M. Park, J. H. Kim, H. Kim and H. J. Sohn, *Chem. Soc. Rev.*, **39**, 3115 (2010).

[122] H. Guo, H. Zhao, C. Yin and W. Qiu, *Mat. Sci. Eng. B*, **131**, 173 (2006).

[123] T. Takamura, S. Ohara, M. Uehara, J. Suzuki and K. Sekine, *J. Power Sources*, **129**, 96 (2004).

[124] M. Uehara, J. Suzuki, K. Tamura, K. Sekine and T. Takamura, *J. Power Sources*, **146**, 441 (2005).

[125] E. Pell, *Phys. Rev.*, **119**, 1222 (1960).

[126] T. L. Kulova, Y. V. Pleskov, A. M. Skundin, E. I. Terukov and O. I. Kon'kov, *Russ. J. Electrochem.*, **42**, 708 (2006).

[127] M. D. Levi and D. Aurbach, *J. Phys. Chem. B*, **101**, 4641 (1997).

[128] S. H. Nam, K. S. Kim, H. S. Shim, S. H. Lee, G. Y. Jung and W. B. Kim, *Nano. Lett.*, **11**, 3656 (2011).

[129] A. Esmanski and G. A. Ozin, *Adv. Funct. Mater.,* **19**, 1999 (2009).

[130] C. Pierrakos and J.-L. Vincent, *Critical Care*, **14**, R15 (2010).

Appendix – List of patents, presentations and publications

Patents:

- Khan, S. A., Dawood, M. K. B., Rajagopalan, R., Choi, W. K., Zheng, H., Process for altering the wetting properties of a substrate surface, US 20130171413 A1, 2013.

- Choi, W. K., Too, H. P., Rajagopalan, R., Zhou, L., Dawood, M. K. B., Zheng, H., Cheng, H., A microarray and method for forming the same, PCT/SG2012/000480, 2012.

Publications / Presentations:

- Zheng. H., Cheng. H., Wu. J., Zhou L., Dawood M. K., Rajagopalan R., Too H. P., Choi W. K., Porous Si nanowires based analyte-specific spatially addressable DNA and protein microarrays, MRS Spring, 2014.

- Cheng, H., Zheng, H., Wu, J., Xu, W., Zhou, L., Leong, K. C., Fitzgerald, E. A., Rajagopalan, R., Too, H. P., Choi, W. K., Photo-activation of biomolecules on silicon nanowires, Lab on a Chip, 2014, pending for publication.

- Wu, J., Zheng, H., Cheng, H., Zhou, L., Leong, K. C., Rajagopalan, R., Too, H. P., Choi, W. K., Thermoporometry characterization of silica microparticles and nanowires, Langmuir, 2014, 30, 2206.

- Lai, CQ, Mai TT, H Zheng, W Zheng, PS Lee, KC Leong, Chengkuo Lee and WK Choi, "Effects of structural and chemical anisotropy of nanostructures on droplet spreading on a two-dimensional wicking surface", Journal of Applied Physics, 2014, 116, 034907.

- Lai, Changquan, Mai TT, H Zheng, PS Lee, KC Leong, Chengkuo Lee and WK Choi, "Influence of nanoscale geometry on the dynamics of wicking into a rough surface", Applied Physics Letters, 2013, 102, 053104.

- Lai, Changquan, Mai, Trong Thi, H Zheng, PS Lee, KC Leong, Chengkuo Lee and WK Choi, "Droplet spreading on a two-dimensional wicking surface", Physical Review E, 2013, 88, 062406.

- Dawood, M. K., Zhou, L., Zheng, H., Cheng, H., Wan, G., Rajagopalan, R., Too, H. P., Choi, W. K., Nanostructured Si-nanowire microarrays for enhanced-performance bio-analytics, Lab on a Chip, 2012, 12 , 5016-5024.

- Dawood, M. K., Zheng, H., Kurniawan, N. A., Leong, K. C., Foo, Y. L., Rajagopalan, R., Khan, S. A.,Choi, W. K., Modulation of surface wettability of superhydrophobic substrates using Si nanowire arrays and

capillary-force-induced nanocohesion, Soft Matter, 2012, 8, 3549-3557.

- Dawood, M. K., Zheng, H., Liew, T. H., Leong, K. C., Foo, Y. L., Rajagopalan, R., Khan, S. A., Choi, W. K., Mimicking both petal and lotus effects on a single silicon substrate by tuning the wettability of nanostructured surfaces, Langmuir , 2011, 27, 4126-4133.